Clinical-task based reconstruction in Digital Breast Tomosynthesis

Maissa Sghaier

▶ **To cite this version:**

Maissa Sghaier. Clinical-task based reconstruction in Digital Breast Tomosynthesis. Signal and Image processing. Université Paris-Saclay, 2020. English. NNT : 2020UPASG040 . tel-03163854v2

HAL Id: tel-03163854
https://theses.hal.science/tel-03163854v2

Submitted on 9 Mar 2021

HAL is a multi-disciplinary open access archive for the deposit and dissemination of scientific research documents, whether they are published or not. The documents may come from teaching and research institutions in France or abroad, or from public or private research centers.

L'archive ouverte pluridisciplinaire **HAL**, est destinée au dépôt et à la diffusion de documents scientifiques de niveau recherche, publiés ou non, émanant des établissements d'enseignement et de recherche français ou étrangers, des laboratoires publics ou privés.

université
PARIS-SACLAY

Clinical-task based reconstruction in Digital Breast Tomosynthesis

Thèse de doctorat de l'Université Paris-Saclay

École doctorale n° 580, Sciences et Technologies de l'Information et de la Communication (STIC)
Spécialité de doctorat: Traitement du signal et des images
Unité de recherche: Université Paris-Saclay, CentraleSupélec, Centre de Vision Numérique, 91190, Gif-sur-Yvette, France
Référent: CentraleSupélec

Thèse présentée et soutenue par visioconférence totale, le 18 décembre 2020, par

Maissa SGHAIER

Composition du jury:

Denis Kouamé Professeur, Université Paul Sabatier, IRIT Lab (Toulouse, France)	Président & Examinateur
Amel Benazza-Benyahia Professeure à SUP'COM, Université de Carthage (Tunis, Tunisie)	Rapporteur & Examinatrice
Ioannis Sechopoulos Associate Professor of Radiology and Center Nuclear Medicine, Radboud University Medical Center (Nijmegen, Netherlands)	Rapporteur & Examinateur
Aurelia Fraysse Maître de conférence, Université Paris-Sud, L2S (Gif-sur-Yvettes, France)	Examinatrice
Laurent Najman Professeur à l'ESIEE, Université Paris-Est, Gaspard-Monge, A3SI (Noisy-le-Grand, France)	Examinateur
Jean-Christophe Pesquet Professeur, Université Paris-Saclay, CentraleSupélec, Inria, CVN (Gif-sur-Yvette, France)	Directeur de thèse
Emilie Chouzenoux Chargée de recherche INRIA, Université Paris-Saclay, CentraleSupélec, Inria, CVN (Gif-sur-Yvette, France)	Co-directrice de thèse
Serge Muller Chief Scientist, Women's Health and X-Ray, GE Healthcare, (Buc, France)	Co-directeur de thèse
Laurent Levy Radiologue, Institut de Radiologie de Paris (Paris, France)	Invité

Thèse de doctorat

NNT: 2020UPASG040

université PARIS-SACLAY

ÉCOLE DOCTORALE
Sciences et technologies de l'information et de la communication (STIC)

Titre: Modélisation de la tâche clinique en reconstruction pour la tomosynthèse numérique du sein

Mots clés: Détectabilité, Optimisation, Reconstruction d'images 3D, Problème inverse, Tomosynthèse numérique du sein, Variation Totale

Résumé: La reconstruction en tomosynthèse numérique du sein est considérée comme un problème inverse, pour lequel les méthodes itératives régularisées permettent de fournir une bonne qualité d'image. Bien que la tâche clinique joue un rôle crucial lors de l'examen des images par le radiologue, elle n'a pas été jusqu'à présent directement prise en compte dans le processus de reconstruction des images de tomosynthèse. Dans cette thèse, nous introduisons une nouvelle formulation variationelle de la reconstruction des images en tomosynthèse numérique du sein qui intègre la tâche clinique du radiologue, notamment la détection des microcalcifications. Le but de cette approche est de permettre à la fois le rehaussement de la détectabilité des microcalcifications et une restauration de bonne qualité des tissus mammaires.

Tout d'abord, nous proposons une nouvelle approche qui vise à rehausser la détectabilité des microcalcifications. Nous formulons une nouvelle fonction de détectabilité inspirée d'observateurs mathématiques. Nous l'intégrons, par la suite, dans une fonction objectif minimisée par un algorithme de reconstruction dédié. Nous montrons finalement l'intérêt de notre approche à l'égard des méthodes standards de reconstruction.

Dans une deuxième partie, nous introduisons une nouvelle régularisation, Spatially Adaptive Total Variation (SATV), en complément de la fonction de détectabilité dans le problème de reconstruction en tomosynthèse. Nous proposons une formulation originale où l'opérateur de gradient est remplacé par un opérateur adaptatif appliqué à l'image qui incorpore efficacement la connaissance *a priori* relative à la localisation de petits objets. Ensuite, nous dérivons notre régularisation SATV et l'intégrons dans une nouvelle approche de reconstruction. Les résultats expérimentaux montrent que SATV est une piste prometteuse pour améliorer les méthodes de régularisation de l'état de l'art.

Dans une troisième partie, nous étudions l'application de l'algorithme de Majoration-Minimisation à Mémoire de Gradient (3MG) à notre problème de reconstruction. Dans le but d'accroître sa vitesse de convergence, nous proposons deux améliorations numériques. Dès lors, les performances numériques sont évaluées en comparant la vitesse de convergence de la méthode proposée avec celles d'algorithmes d'optimisation convexe concurrents.

La dernière partie de la thèse porte sur l'évaluation quantitative des contributions de l'approche de reconstruction proposée en tomosynthèse numérique du sein. Nous menons une étude de lecture d'images impliquant quatorze lecteurs dont neuf radiologues avec différents niveaux d'expertise et cinq experts en mammographie de GE Healthcare. Les résultats démontrent l'intérêt de notre approche de reconstruction par rapport à l'approche standard non-régularisée selon des critères visuels spécifiques.

Title: Clinical-Task based reconstruction in Digital Breast Tomosynthesis

Keywords: 3D image reconstruction, Detectability, Digital Breast Tomosynthesis, Inverse problem, Optimization, Total Variation

Abstract: The reconstruction of a volumetric image from Digital Breast Tomosynthesis (DBT) measurements is an ill-posed inverse problem, for which existing iterative regularized approaches can provide a good solution. However, the clinical task is somehow omitted in the derivation of those techniques, although it plays a primary role in the radiologist diagnosis. In this work, we address this issue by introducing a novel variational formulation for DBT reconstruction. Our approach is tailored for a specific clinical task, namely the detection of microcalcifications. Our method aims at simultaneously enhancing the detection performance and enabling a high-quality restoration of the background breast tissues.

First, we propose an original approach aiming at enhancing the detectability of microcalcifications in DBT reconstruction. Thus, we formulate a detectability function inspired from mathematical model observers. Then, we integrate it in a cost function which is minimized for 3D reconstruction of DBT volumes. Experimental results demonstrate the interest of our approach in terms of microcalcification detectability.

In a second part, we introduce the Spatially Adaptive Total Variation (SATV) as a new regularization strategy applied to DBT reconstruction, in addition to the detectability function. Hence, an original formulation for the weighted gradient field is introduced, that efficiently incorporates prior knowledge on the location of small objects. Then, we derive our SATV regularization, and incorporate it in our proposed 3D reconstruction approach for DBT. We carry out several experiments, in which SATV regularizer shows a promising improvement with respect to state-of-the-art regularization methods.

Third, we investigate the application of Majorize Minimize Memory Gradient (3MG) algorithm to our proposed reconstruction approach. Thus, we suggest two numerical improvements to boost the speed of the reconstruction scheme. Then, we assess the numerical performance of 3MG by comparing the convergence speed of the proposed method with state-of-the-art convex optimization algorithms.

The last part of this thesis is focused on the quantitative assessment of the contribution of our proposed DBT reconstruction. Thus, we conduct a visual experiment trial involving fourteen readers including nine radiologists with different levels of expertise and five GE Healthcare experts in mammography. According to specific visual criteria, the results show the superiority of our proposed reconstruction approach over the standard non-regularized least squares solution.

Université Paris-Saclay
Espace Technologique / Immeuble Discovery
Route de l'Orme aux Merisiers RD 128 / 91190 Saint-Aubin, France

I dedicate this thesis to the loving memory of my grand-fathers, my dearest grand-mothers, my beloved parents and my precious three flowers.

"The knowledge that has not come down to us is larger than the knowledge that has," Ibn Khaldun, The Muqaddimah: An Introduction to History.

"We see with our brains, not with our eyes," Norman Doidge, The Brain That Changes Itself: Stories of Personal Triumph from the Frontiers of Brain Science

"If you hear a voice within you say 'you cannot paint,' then by all means paint, and that voice will be silenced," Vincent Van Gogh

"Happy is the man who can with vigorous wing
Mount to those luminous serene fields,

The man whose thoughts, like larks,
Take liberated flight toward the morning skies
–Who hovers over life and understands without effort
The language of flowers and voiceless things!"
Charles Beaudelaire, Élévation (les fleurs du mal, 1857)

Acknowledgment

This PhD thesis research is a collaboration between GE Healthcare France and laboratory Center for Visual Computing - OPIS Inria group, Centrale-Supelec, University Paris-Saclay. This work was partially founded by the Association Nationale de la Recherche Technique (ANRT) under CIFRE grant n°2017/0106.

Undertaking this PhD has been a truly life-changing experience for me and it would not have been possible to do without the encouragement, the help and the support that I have received from many people.

First, I would like to express my sincere gratitude to my thesis advisors Prof. Jean-Christophe Pesquet, Dr. Emilie Chouzenoux and Dr. Serge Muller. Jean-Christophe and Emilie, your guidance and your insights on optimization and algorithms pushed me to sharpen my thinking and brought my work to a higher level. Serge, your commitment, continuous support and our uncountable inspiring scientific discussions have provided me with the tools that I needed to make my work a potential clinical reality. Besides, I have particularly enjoyed our philosophical discussions about life and arts that were stimulating and happy moments during my PhD. I would also like to thank Dr. Giovanni Palma for his supervision during my first year PhD and for sharing his knowledge on practical apsects of tomosynthesis reconstruction and C++ coding. I would like to convey my deepest gratitude to Dr. Ann-Katherine Carton for her expert support in the implementation and statistical analysis that provided the perfect "Finale" to my symphony.

I would like to thank all the members of my jury, who accepted to spend their precious time evaluating my thesis work. I would like to thank the president of the jury Prof. Denis Kouamé, Prof. Amel Benazza and Dr. Ioannis Sechopoulos who reviewed this manuscript and Prof. Laruent Najman and Dr. Aurelia Fraysse for their valuable questions. I would like to extend my gratitude to Dr. Laurent Levy for the wonderful collaboration in the preference trial and for his expert feedback.

I am also grateful for the time spent reading our images in the preference trial and their valuable comments to Dr. Hegar Bouchoucha, Dr. Stéphanie Cohen-Zarade, Dr. Sophie Grivaud, Dr. Gabrielle Journo, Dr. Hélène

Kokotek, Dr. Michael Suissa (Institut de radiologie de Paris, Paris France), Dr. Philippe Benilouche and Dr. Patrick Toubiana (CSE imagerie médicale numérique, Paris, France).

To all my WHARe-mates: Laurnece, Viviane, Clément, Pablo, Zhijin, Andrei, Ruben and Dr. to be Karine, thank you for your encouragements, stimulating conversations, food...and especially your machines to run my endless DBT reconstructions. I also wish to thank a number of GE colleagues including Jorge Corsinoespino, Vincent Bismuth, Charlotte Delams, Cyril Riddell and Giang-Chau NGO for many inspiring discussions about DBT reconstruction challenges. A special mention to office fellows and freinds: Anna, Aymeric, Ketan, Emmanuelle, Ludovic, Thuy, Bianca, Marion, Gwladys and the list never ends.

I would like to thank my fellow CVN-mates, old and new: Sagar, Kadir, Kavya, Yunshi, Yingping, Mathieu, Arthur, Marie-Caroline, Mihir, Maria V. and Maria P. It was wonderful to have the opportunity to do reseacrh by your sides. I will always cherish the memories and the fun we have had inside and outside the lab.

Finally, I could not have completed this dissertation without the unconditional love and support of my family and my freinds. Words are just worthless to express my deepest gratitude and love especially to my *parents* who raised me with a love of Science and Arts and supported me in all my pursuits. To my dearest *neko-punchy*, *riri* and *rourou* who are always there for me, thank you my priceless gift of life.

Résumé

Le cancer du sein est le cancer le plus fréquemment diagnostiqué et la deuxième cause de décès, chez les femmes. Selon l'organisation mondiale de la santé, cette maladie touche environ $2,1$ millions de femmes chaque année. Les campagnes de dépistage à partir d'un certain âge jouent un rôle fondamental pour réduire la mortalité causée par le cancer du sein. Dans ce contexte, la mammographie est la modalité d'imagerie actuellement utilisée en première intention pour le dépistage et le diagnostic du cancer du sein. Cette technique d'imagerie permet l'observation du sein radiographié par rayons X sur un plan 2D. Bien que cette modalité ait prouvé son efficacité, elle présente des limitations inhérentes à la superposition des tissus lors de la projection du sein sur le plan image, ce qui a pour conséquence de réduire la visibilité des lésions, voire de les occulter complétement. Afin de pallier ces défauts, une alternative est de considérer l'information tridimensionnelle du sein. L'introduction de la tomosynthèse numérique du sein semble une voie prometteuse d'imagerie tridimensionnelle utilisée dans le dépistage et le diagnostic du cancer du sein. Elle s'appuie sur l'acquisition d'un ensemble de projections 2D sur une ouverture angulaire limitée. Par la suite, un algorithme de reconstruction permet de retrouver un volume 3D composé de coupes parallèles au détecteur permettant la réduction de la superposition des structures. Cette modalité favorise l'exploration volumique des seins denses. En outre, elle permet une meilleure visibilité et identification des lésions potentiellement présentes dans le sein et donc de réduire le taux de femmes rappelées pour des examens complémentaires.

La précision du diagnostic lors du dépistage du cancer du sein dépend considérablement de la capacité du radiologue à détecter facilement les lésions et plus particulièrement les microcalcifications dans les images analysées. Bien que la tomosynthèse ait le potentiel de réduire le problème de superpositions des tissus posé en mammographie standard, la détectabilité des microcalcifications n'a pas encore atteint un niveau de qualité faisant consensus au sein de la communauté médicale. Premièrement, la détection des microcalcifications est une tâche difficile à cause de leur petite taille et de leur contraste parfois faible dans les seins denses. Deuxièmement, l'apport

de la représentation tridimensionnelle du sein par la tomosynthèse se fait au prix d'une plus grande quantité d'images à analyser pour le radiologue. En effet, un volume 3D peut compter dix à cinquante fois plus d'images à examiner qu'un cliché 2D issu de la mammographie standard ce qui augmente la durée et la complexité de l'interprétation pour le radiologue. Ses performances de détection en sont ainsi affectées. Finalement, étant donnée l'ouverture angulaire limitée lors de l'acquisition des projections en tomosynthèse, les volumes reconstruits sont caractérisés par une résolution anisotrope, avec une haute résolution au niveau des plans parallèles au détecteur et une résolution très inférieure dans la direction perpendiculaire, ce qui peut avoir un impact néfaste sur la visibilité des microcalcifications.

Afin d'améliorer la performance des radiologues en termes de détectabilité des microcalcifications en tomosynthèse numérique du sein, une solution est d'investiguer l'algorithme de reconstruction qui joue un rôle crucial sur l'apparence des données reconstruites. D'un point de vue mathématique, la reconstruction en tomosynthèse numérique du sein est un problème inverse mal posé, pour lequel les méthodes itératives régularisées ont démontré leur supériorité sur les méthodes analytiques. En effet, l'avantage primordial des méthodes itératives consiste à incorporer de la connaissance *a priori* pour pallier au problème de données manquantes. D'un point de vue pratique, ces termes *a priori* sont généralement réglés de manière à optimiser des métriques de qualité d'image. Ces dernières, bien que garantissant une certaine intégrité de la restauration des données, ne modélisent pas la tâche clinique du radiologue, notamment la détection des microcalcifications. De plus, le sein est constitué de plusieurs composantes anatomiques avec des propriétés d'atténuation différentes, par rapport à celles des microcalcifications. Dans ce contexte, avoir recours à des termes de régularisation standard, comme par exemple la variation totale classique, s'avère insuffisant pour gérer l'hétérogénéité des images du sein.

Dans cette thèse, nous proposons de reformuler le problème de reconstruction en tomosynthèse de manière à maximiser la détection des microcalcifications par le radiologue, en prenant en compte les spécificités anatomiques du sein. Plus précisément, nous proposons la minimisation d'une fonction coût intégrant des termes de régularisation qui encodent efficacement des connaissances *a priori* cliniquement significatives. Dès lors, nous introduisons une nouvelle formulation variationelle de la reconstruction des images en tomosynthèse numérique du sein qui permet à la fois le rehaussement de la détectabilité des microcalcifications et une restauration de bonne qualité des tissus mammaires.

Les contributions de la thèse comportent quatre volets :

1. Nous proposons un nouveau terme *a priori*, qui vise à réhausser la détectabilité des microcalcifications. La stratégie de détection optée par les observateurs mathématiques CHO ajoutée à la reconstruction

itérative régularisée en tomosynthèse seront présentées dans le chapitre 3.

2. Nous introduisons, dans le chapitre 4, une nouvelle régularisation spatiale, *Spatially Adaptive Total Variation* (SATV), en complément de la fonction de détectabilité dans le problème de reconstruction en tomosynthèse.

3. Nous étudions l'application de l'algorithme de Majoration-Minimisation à Mémoire de Gradient (3MG) à notre problème de reconstruction et en proposons une version accélérée, dans le chapitre 5.

4. Nous menons dans le chapitre 6 une étude d'analyse d'images impliquant quatorze lecteurs dont neuf radiologues avec différents niveaux d'expertise et cinq experts en mammographie de GE Healthcare afin d'évaluer quantitativement les contributions de l'approche de reconstruction proposée en tomosynthèse numérique du sein.

Nous commençons par une introduction générale dans le chapitre 1, en détaillant les objectives de la thèse, les contributions ainsi que les publications relatives à nos travaux de recherche.
Le chapitre 2 est consacré à expliquer le contexte clinique relatif à nos travaux de recherche. Tout d'abord, nous décrivons l'épidémiologie du cancer du sein et nous présentons brièvement les différentes modalités d'imagerie actuellement utilisées pour le dépistage et le diagnostic du cancer du sein. Nous introduisons par la suite la tomosynthèse numérique du sein en mettant en relief les avantages par rapport à la mammographie standard. Dès lors, nous nous focalisons sur les principes généraux afin de mieux comprendre les enjeux et les points d'amélioration potentiels dans le cadre de détection des microcalcifications. Nous finissons ce chapitre par l'étude du processus de reconstruction en tomosynthèse. Cette dernière s'avère une voie prometteuse et cruciale pour améliorer la détectabilité des microcalcifications par le radiologue.

Dans le chapitre 3, nous introduisons la nouvelle approche proposée qui vise à rehausser la détectabilité des microcalcifications. Nous commençons par présenter les limites des approches standard de reconstruction en tomosynthèse qui ne prennent pas en compte la tâche clinique du radiologue, notamment la détection des microcalcifications. Dès lors, nous proposons notre approche en formulant tout d'abord une nouvelle fonction de détectabilité inspirée des observateurs mathématiques. Nous expliquons, par la suite, la construction et l'implémentation de ce nouveau terme *a priori* qui sera intégré dans une fonction objectif minimisée par un algorithme de reconstruction dédié. Nous montrons finalement l'intérêt de notre approche à l'égard des méthodes standard de reconstruction sur des données synthétiques et cliniques.

Le chapitre 4 est dédié à la nouvelle régularisation spatiale SATV. En premier lieu, nous présentons les régularisations spatiales de l'état de l'art basées sur la variation totale. Ensuite, nous expliquons le besoin d'introduire une régularisation spatiale plus sophistiquée et adaptée au contenu morphologique des images du sein. Nous suggérons alors une formulation originale où l'opérateur de gradient est remplacé par un opérateur adaptatif appliqué à l'image qui incorpore efficacement la connaissance *a priori* relative à la localisation de petits objets. Enfin, nous déduisons notre régularisation SATV et l'intégrons dans une nouvelle approche de reconstruction. Les résultats obtenus sur des données synthétiques et cliniques démontrent que SATV présente une piste prometteuse pour améliorer les méthodes de régularisation de l'état de l'art.

Dans le chapitre 5, nous étudions l'application de l'algorithme de Majoration Minimisation à Mémoire de Gradient (3MG) à notre problème de reconstruction. Dans le but d'accroître sa vitesse de convergence, nous proposons deux améliorations numériques : premièrement, nous considérons la formulation d'une majorante locale de la fonction objectif à minimiser dans le voisinage de l'itération actuelle. Cette amélioration revient à relaxer l'hypothèse de majoration dans le principe du Majoration-Minimisation (MM). Deuxièmement, nous formulons une nouvelle approche qui vise à augmenter progressivement le poids de la fonction de distance. Nous évaluons finalement les performances numériques de l'algorithme 3MG amélioré en comparant sa vitesse de convergence avec celles d'algorithmes d'optimisation convexe concurrents.

Le chapitre 6 porte sur l'évaluation quantitative des contributions de l'approche de reconstruction proposée en tomosynthèse numérique du sein. Nous décrivons tout d'abord la méthodologie adoptée dans notre étude de lecture d'images en expliquant la construction de la base de données utilisée, les lecteurs impliqués et le protocole de lecture des images. Nous présentons finalement les résultats qui démontrent l'intérêt de notre méthode de reconstruction par rapport à l'approche standard non-régularisée selon des critères visuels spécifiques.

Dans le chapitre 7, nous résumons nos principales contributions et nous proposons plusieurs pistes pour de futurs travaux.

Notation

$\mathbb{R}$	:	set of real numbers
$\mathbb{R}^m$	:	set of vectors with m entries
$\mathbb{R}^{m\times n}$	:	set of matrices with m rows and n columns
$\mathbb{N}$	:	set of positive integers
v	:	scalars and vectors will be denoted by lowercase letters
M	:	matrices will be denoted by uppercase letters
$M^\top, M^{-1}$	:	transpose and inverse of M, respectively
I_m	:	square identity matrix $\mathbb{R}^m$
v_i	:	ith coefficient of v
$\|v\|_1$	:	ℓ_1 norm of v
$\|v\|$	:	ℓ_2 norm of v
$\|v\|_{1,2}$	:	$\ell_{1,2}$ norm of v
$\|M\|_S$	:	spectral norm of M
$\mathrm{Diag}\{v\}$	:	diagonal matrix whose elements are given by v
$\nabla f(v)$	:	gradient function f evaluated at v
Δ	:	3D discretized gradient operator in $\mathbb{R}^{3m\times m}$
ι_C	:	indicator function of set C
P_C	:	porjection onto set C
$\mathsf{p}(x)$	:	prior probability density function of x
$\mathsf{p}(x \mid z)$	:	probability density function of x given z

Acronyms

2D	:	Two-Dimensional
3D	:	Three-Dimensional
3MG	:	Majorize-Minimize Memory Gradient
ACR	:	American College of Radiology
ADMM	:	Alternating Direction Method of Multipliers
AIP	:	Average Intensity Projection
BI-RADS	:	Breast Imaging Reporting and Database System
CAD	:	Computer-Aided Detection
CC	:	Cranio-Caudal
CESM	:	Contrast Enhanced Spectral Mammography
CE-MRI	:	Contrast Enhanced Magnetic Resonance Imaging
CHO	:	Channelized Hotelling Observer
CTBR	:	Clinical Task-Based Reconstruction
DBT	:	Digital Breast Tomosynthesis
DL	:	Deep Learning
dNRLS	:	Non-Regularized Least Squares solution using a detectability function
dSATV	:	DBT reconstruction with detectability function and Spatially Adaptive Total Variation regularization
dTV	:	DBT reconstruction with detectability function and Total Variation
FBP	:	Filtered Back-Projection
FDA	:	Food and Drug Administration
FFDM	:	Full Field Digital Mammography
FISTA	:	Fast Iterative Shrinkage-Thresholding Algorithm
FN	:	False Negative
FP	:	False Positive
HE	:	High Energy
HO	:	Hotelling Observer
IO	:	Ideal Observer
LE	:	Low Energy
log-TV	:	smoothed log-Total Variation

MAP	:	Maximum A Posteriori
MIP	:	Maximum Intensity Projection
ML	:	Maximum Likelihood
MLO	:	Mediolateral Oblique
MM	:	Majoration-Minimization
MRI	:	Magnetic Resonance Imaging
NLTV	:	Non-local Total Variation
NRLS	:	Non-Regularized Least Squares
PGD	:	Projected Gradient Descent
ROI	:	Region Of Interest
SAA	:	Shift-And-Add
SART	:	Simultaneous Algebraic Reconstruction Technique
SATV	:	Spatially Adaptive Total Variation
SDNR	:	Signal Difference to Noise Ratio
SIRT	:	Simultaneous Iterative Reconstruction Technique
SNR	:	Signal to Noise Ratio
SOOT-TV	:	Smoothed One Over Two-Total Variation
TGV	:	Total Generalized Variation
TV	:	Total Variation
TVSG	:	Total Variation on a Staggered Grid
U/S	:	Breast Ultrasound
Welsch-TV	:	Welsch-Total Variation
WHO	:	World Health Organization

Contents

- Chapter 1 -

General introduction

§ 1.1 Context

In a will to reduce the mortality linked to breast cancer, heavy demands on improving medical imaging modalities for breast cancer detection led to many developments conducted in the last few years. Full Field Digital Mammograph (FFDM) has for a long time been considered as the gold standard for screening and early detection of breast cancer. Recently, Digital Breast Tomosynthesis (DBT) has nonetheless demonstrated its clinical superiority over FFDM for detecting lesions with comparable X-ray dose.

One of the main features of DBT is to foster a quasi-3D image of the breast. Indeed, it relies on the acquisition of a set of low-dose 2D projections on a limited angular aperture. The reconstruction of a 3D volume of the imaged object from these projections is conducted thanks to a reconstruction algorithm. This 3D nature of the reconstructed image is of a crucial importance, in particular for women with dense and heterogeneous breasts. Indeed, in dense breasts cancer detection can lead to lower clinical performance when using FFDM due to the superimposition of tissues inherent to the projection process. In analogy to looking for a needle in a haystack, detecting a cancer lesion by visual inspection of a standard 2D mammography is very challenging. Therefore, three-dimensional DBT offers a piercing view through the haystack, i.e., the breast, by decreasing masking effect of tissue superimposition. Thus, it helps to reduce recall rates, to improve the accuracy of breast cancer detection, and consequently to improve the clinical performance especially for dense breasts.

The diagnosis accuracy in breast cancer screening highly depends on the facility of the radiologist to detect lesions and more particularly microcalcifications within the analyzed images. Nevertheless, microcalcification detectability in the context of DBT has not yet reached consensus in the

medical community. First, microcalcification detection is a very challenging task due to their small size and their potential low contrast in dense areas of the breast. Second, the high number of images to be reviewed in DBT, due to its three dimensional nature, increases the time and complexity of the interpretation for the radiologist, that may negatively affect her/his performance in terms of visual detection accuracy. Third, due to inherent geometric limitations of DBT, the reconstructed DBT volumes are characterized by anisotropic spatial resolution, with high resolution in the planes parallel to the detector and much lower resolution in the perpendicular direction.

One leading research direction to improve microcalcification detectability performance in DBT is to investigate on the reconstruction process of DBT volumes. DBT image reconstruction is considered as an ill-posed problem where iterative algorithms demonstrated their superiority over the analytical ones. The main advantage of such methods is their ability to incorporate prior knowledge aiming at mitigating the missing information issue. Although these regularized approaches seem to provide a certain trade-off in terms of image quality in DBT, they do not account for the aforementioned clinical task, i.e. microcalcification detection. In addition, breasts are composed of several anatomical components with different attenuation properties compared with the ones of microcalcifications. Employing classical regularization approaches, such as total-variation (TV), may not be adapted to handle such heterogeneity within the DBT images.

In this work, we propose to reformulate the reconstruction method so that it maximizes the clinical task (detection of microcalcification) taking into consideration the anatomical specificities within the breast. More precisely, we investigate the minimization of a penalized least squares cost function encoding some clinically meaningful prior knowledge. Then, we introduce a novel variational reconstruction framework in DBT which is tailored to enhance the microcalcification detectability and to enable a high quality restoration of the breast tissue background. The outcomes of our work have both mathematical and applicative components.

§ 1.2 Main contributions

Chapter 3 focuses on introducing a new a priori term in the DBT reconstruction process by adding to classical regularized iterative DBT reconstruction a task-based assessement strategy implemented in CHO observer. Our contributions are:

(i) A new approach is proposed aiming at enhancing the detectability of microcalcifications in DBT reconstruction as the targeted clinical task.

(ii) A detectability penalty function is defined which is computed following

an approach similar to the mathematical model observer CHO and integrated as an a priori term in the proposed optimization approach.

(iii) Experimental results obtained on both synthetic and clinical datasets demonstrate the potential interest of our method with respect to standard DBT reconstruction in terms of microcalcification visibility.

Chapter 4 introduces a new Spatially Adaptive Total Variation (SATV) regularization in DBT reconstruction, in addition to the detectability function. Our contributions are:

(i) We provide a new definition for the weighted gradient field by integrating a priori knowledge on microcalcification spatial location.

(ii) SATV is incorporated as a spatial regularization term with the detectability function in DBT reconstruction, leading to the dSATV reconstruction approach.

(iii) Experimental results conducted on several datasets highlight the potential interest of our proposed dSATV approach which constitutes a promising way of improving state-of-the-art regularization methods.

In Chapter 5, we investigated the application of the Majorize-Minimize Memory Gradient (3MG) algorithm to our proposed dSATV approach. Our contributions are:

(i) Two numerical improvements are proposed for 3MG algorithm when applied to our reconstruction approach. These improvements comprise a definition of a local majoration of the objective function in the neighbourhood of the current iterate and a new scheme of the weight of the distance penalization function of each voxel of the volume to the plausible hypercube values.

(ii) We conduct a numerical comparison of the convergence speed of the proposed method with those of standard convex optimization algorithms and we showed the interest of the proposed numerical improvements of 3MG in terms of convergence speed.

In Chapter 6, a visual experiment trial is conducted with fourteen readers including nine radiologists with different levels of expertise and five GE Healthcare experts in mammography to quantitatively evaluate the contribution of our proposed dSATV approach. Our contributions in this chapter are:

(i) We present a clinical protocol to carry out a visual study assessing the potential benefits of our proposed 3D reconstruction algorithm.

(ii) We provide a comparison of dSATV and the standard non-regularized least squares solution NRLS according to four criteria: microcalcification conspicuity, rendering of breast structures, presence of potential artifacts and overall visual preference.

(iii) An inter-reader agreement analysis was conducted to highlight the image preference triggers from the different reader populations.

§ 1.3 Related publications

Journal papers

- M. Sghaier, E. Chouzenoux, J.C. Pesquet and S. Muller, "A Novel Task-Based Reconstruction Approach for Digital Breast Tomosynthesis", *Submitted to Medical image analysis.*

Conference papers

- M. Sghaier, E. Chouzenoux, J.C. Pesquet and S. Muller, "A New Spatially Adaptive TV Regularization for Digital Breast Tomosynthesis," *2020 IEEE 17th International Symposium on Biomedical Imaging (ISBI 2020)*, Iowa City, IA, USA, 2020, pp. 629-633.

- M. Sghaier, E. Chouzenoux, G. Palma, J.C. Pesquet and S. Muller, "A New Approach For Microcalcification Enhancement In Digital Breast Tomosynthesis Reconstruction," *2019 IEEE 16th International Symposium on Biomedical Imaging (ISBI 2019)*, Venice, Italy, 2019, pp. 1450-1454.

§ 1.4 Outline

The manuscript is organized as follows.
In Chapter 2, we introduce the context of our research work. First, we provide the clinical context in Section 2.2 by giving an overview of breast cancer epidemiology and the main diagnosis imaging modalities currently used for breast cancer screening. Then, we focus on DBT by spotlighting its main benefits over standard x-ray mammography, which is the current standard for screening and early detection of breast cancer. In Section 2.3, we foster an exhaustive presentation of DBT to understand the challenges and identify some potential improvements in microcalcification detectability task. Then, in Section 2.4 we investigate the reconstruction process of DBT volumes as a promising research direction to enhance microcalcification detectability performance in DBT.

Chapter 3 is dedicated to introducing a novel approach for microcalcification enhancement in DBT reconstruction. First, in Section 3.2 we explain the motivation and the mathematical formalism of our approach. Then, in Section 3.3, we present the construction of the clinical task based a priori term introduced in our approach. Finally, by integrating the developed clinical term in an optimization framework, we illustrate on both synthetic and clinical datasets the potential interest of our method with respect to standard DBT reconstruction in terms of microcalcification visibility, in Section 3.4.

In Chapter 4, we introduce a new Spatially Adaptive TV (SATV) regularization function and its application in DBT. In Section 4.2, we present state-of-the-art TV-based regularization strategies. Then, in Section 4.3 we provide a novel definition of the weighted gradient field by integrating a priori knowledge on microcalcification spatial location. Subsequently, we deduce the SATV regularization and integrate it in the clinical task-based reconstruction approach for DBT. Finally, we discuss in Section 4.4 the qualitative results conducted on both physical phantom and clinical datasets.

In Chapter 5, we investigate the application of Majorize-Minimize Memory Gradient (3MG) algorithm to our proposed DBT reconstruction. Therefore, we formulate 3MG algorithm when applied to the clinical-task based reconstruction in Section 5.2. We then suggest two numerical improvements of the algorithm aiming at improving the speed of the reconstruction process in Section 5.3. Finally, in Section 5.4 we evaluate the numerical performance of 3MG by comparing the convergence speed of the proposed method with those of standard convex optimization algorithms.

Chapter 6 presents the quantitative assessment of the proposed DBT reconstruction approach through a visual evaluation study. First, we present in Section 6.2, the methodology of the visual experiment study by describing the construction of the image data set, the image readers and the image review protocol. We then show and discuss the results of our experiment in Section 6.3.

Finally, we draw some conclusions and perspectives in Chapter 7.

- Chapter 2 -

Tomographic reconstruction and its application in DBT

§ 2.1 Introduction

The mortality rate of breast cancer is one of the primary clinical motivation behind developing new and improved breast imaging techniques. As technology evolves, breast cancer imaging and screening, which enables to detect the tumor at the early stage, provides guidance to more effective treatments. Therefore, the need for breast images that maximise the lesion detectability performance becomes increasingly important. In this thesis, we are interested in Digital Breast Tomosynthesis (DBT) as an emerging imaging technique that plays an important role in breast cancer detection.

The objective of this introductory chapter is to present the clinical context of our research. First, we introduce in Section 2.2 breast cancer basics starting from the scope of epidemiology and we describe the main diagnosis imaging modalities currently used to detect suspicious lesions. Then, we focus on DBT by highlighting its main advantages over standard x-ray mammography, which is the current standard for breast cancer screening and diagnosis. A thorough description of DBT will be provided in Section 2.3 to better seize the challenges and identify some potential prospects for its improvement. Thus, in Section 2.4 we delve into one of its main features, which is the reconstruction algorithm, in order to bring insight to the contribution of our research work.

§ 2.2 Clinical context

2.2.1 Breast cancer epidemiology

Cancer is one of the main causes of mortality worldwide. In 2008, 8 million deaths were recorded as a result of malignant cancer diseases. This rate is estimated to reach 11 million by 2030 [99]. Today, breast cancer is the most common cancer among women and the second-leading cause of death among them. According to the World Health Organization (WHO), it impacts 2.1 million women each year. Even though it is often thought of as something which only affects women, breast cancer can harm men as well but accounting for less than 1% of all cases of breast cancers [142].

Several factors contribute to the occurrence of this disease [92]. They mainly include the gender, the age, the genetic mutations (BRCA1 and BRCA2), the family history of breast cancer, the high breast tissue density, the late age at first full-term pregnancy (> 30 years), the early menarche and/or late menopause, the smoking and the alcohol consumption, the lifestyle and the environment. Although breast cancer exists anywhere throughout the world, its incidence, mortality and survival rates vary considerably among different regions. For instance, the incidence rate of breast varies from 27 per $100,000$ people in Middle Africa and East Asia to 96 per $100,000$ people in Western Europe [59]. The incidence rate of breast cancer is estimated to reach 3.2 million by 2050 [70]. While the prevalence of new cases of breast cancer seems to be higher in developed countries, the less developed ones have the higher mortality rates in breast cancer [64]. In fact, the mortality rate of breast cancer in the world is estimated to be 12.9 per $100,000$ people. It varies from 6 cases per $100,000$ people in East Asia while presenting 20 cases per $100,000$ people in Western Africa [76].

Despite those daunting numbers of the mortality rate by breast cancer, early screening and diagnosis can make a life-changing shift in these statistics. While screening consists of identifying the disease before any symptoms appear, diagnosis focuses on providing access to treating the disease. Thus, the goal is to increase the proportions of breast cancers identified at an early stage to allow more effective treatment to be deployed and to reduce drastically the risks of death by breast cancer. In this context, imaging techniques have a crucial role to play, for both screening and diagnosis. Actually, about 90% of cases can be cured, as soon as the breast cancer is diagnosed at an early stage [125].

2.2.2 Imaging modalities for breast cancer screening

Today, x-ray mammography is recognized as the most effective technique for breast cancer detection at an early stage. It has demonstrated a decrease in mortality among screened women up to 40% [65]. This modality, also

known as Full Field Digital Mammography (FFDM), is a two-dimensional (2D) x-ray imaging technique. As depicted in Figure 2.1(a), during the image acquisition, the breast is compressed between the compression paddle and the detector. The compression is important for several reasons [80] :

- It evens out the breast thickness so all of the tissue can be visualized using a detector presenting a limited dynamic in exposure.
- It allows a lower x-ray dose delivered to the breast since a thinner amount of breast tissue is being imaged.
- It reduces motion-based blur as well as x-ray scatter which increases sharpness of the image.

Once the breast is well positioned, x-rays are emitted from the x-ray tube to be transmitted through or absorbed by the breast tissue. The detector then converts the reached x-rays to digital information.

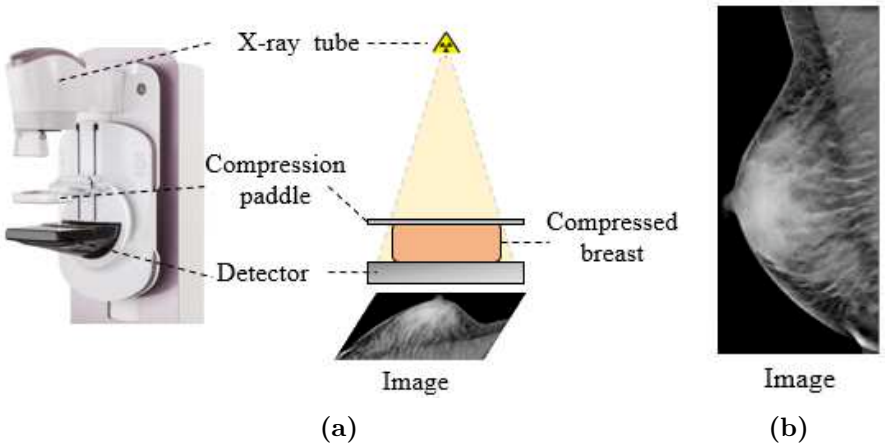

Figure 2.1: *(a) A schematic of a mammography image acquisition. (b) Example of an acquired image from the imaging system.*

The pixels values of the obtained projection image, as shown in Figure 2.1(b), follow the *Beer-Lambert* law which denotes the link between the attenuation of x-ray photons, the thickness and the linear attenuation coefficient of the breast tissue. Assuming a monochromatic x-ray spectrum, the mathematical formulation of *Beer-Lambert* law is

$$I(x,y) = I_0 e^{\left(-\int_{r\in L(x,y)} \mu(r)\,\mathrm{d}r\right)} \tag{2.1}$$

where $L(x,y)$ denotes the x-ray beam path between the x-ray source and the 2D position (x,y) on the detector, I_0 is the x-ray photon intensity incident

upon the breast, $I(x, y)$ is the x-ray photon intensity at the position (x, y). Finally, $\mu(r)$ represents the linear attenuation coefficient of the breast tissue material along the x-ray path. Typically, the breast is composed by fibroglandular tissue and adipose tissue with different attenuation properties each. Indeed, the fibroglandular one tends to absorb more x-ray photons and translate to white areas in the image. Meanwhile, the adipose tissue permits more of the transmission of x-ray photons which translate to darker areas in the mammographic image as illustrated in Figure 2.1(b).

Although FFDM has for long been accepted as the gold standard for screening and early detection of breast cancer, its sensitivity is far from perfect. It ranges from 47.8% to 98% with highly dense fibroglandular tissue presenting the main encumbrance to detection [77]. In this context, supplemental modalities are considered in the clinical routine in order to alleviate this limitation. Breast ultrasound (U/S) has proved its utility for women with dense breast tissue [128]. In fact, the accuracy of detecting breast cancers occulted on mammography using U/S is unaffected by breast tissue density [15, 11]. Furthermore, U/S has been proven to be effective in distinguishing cystic from solid masses. It allows also determining the suspicion of the solid masses and whether a biopsy is needed or not [121, 143, 7]. Unlike x-rays imaging, ultrasound is an imaging technique based on the application of sound waves, i.e. not radiation, for producing images of the internal breast structures. In particular, this technique uses waves which frequencies are above the upper limit of human hearing, called ultrasound, and are able to penetrate biological tissues (at least 1 MHz) [57]. To obtain the image, first a gel is interposed between the U/S probe and the part of the skin of the breast to be diagnosed. The probe is then moved in multiple directions, with an adequate pressure that makes the U/S usually painless. The waves are variably reflected as echoes by the breast tissues. These reflected echoes are received by the probe and forwarded as electronic signals to a computer system that finally generates the images. Even though U/S is more accessible and cost-effective compared to mammography, it is discouraged to perform screening with U/S alone. Indeed, it may not detect efficiently clusters of microcalcifications some of which being an early sign of breast cancer. Furthermore, it generates relatively higher number of false positives compared to FFDM [48, 14, 15] yielding to undesirable negative biopsies. Overall, it has not been shown to reduce mortality from breast cancer when used as stand-alone modality. Yet, it may be considered as an adjunct to mammography in asymptotic women for a specific category, i.e. women with dense breasts, despite the high false positive rate.

Other additional modalities to mammography for the screening of high-risk women are the functional-based techniques. They are based on highlighting the blood vessels developed around the tumor. These blood vessels supply the tumor with oxygen and nutrients to sustain its growth. Thus, defined as tumor angiogenesis, it begins at the earliest stages of tumor de-

velopment. Therefore, imaging this proliferation would enable the detection and the characterization of breast cancer early. In this context, contrast-enhanced magnetic resonance imaging (CE-MRI) is one of the functional imaging techniques. The injection of a gadolinium-based contrast product enables the tracking of the uptake of the contrast agent in the lesions. In particular, the morphology and the kinetic profile of the contrast uptake allows the distinction between malignant lesions from the benign ones [82]. Therefore, it has been shown in several studies that MRI allowed to identify earlier stage disease than mammography and that combining MRI and mammography is linked to decreased mortality rate [89]. Yet, MRI is affected by its high cost, reduced accessibility and a significant rate of false positives.

An additional functional-based modality worth mentioning is Contrast Enhanced Spectral Mammography (CESM). As is the case with FFDM, CESM is a 2D x-ray imaging technique. Yet, its routine is very different from FFDM [83]. First, the patient is injected with iodinated contrast agent. After letting the iodine diffuse for some time, the breast is compressed. Then, two images of the breast are acquired with different x-ray spectra. One of them is located below the discontinuity K of iodine denoted as low-energy (LE) spectrum and the other one is located above it, defined as high-energy (HE) spectrum. Finally, the iodine-enhanced image is obtained by recombining the acquired dual-energy images. The feasibility of CESM was shown in 2003 [83] and became commercially available in 2010 through the introduction of SenoBright application (GE Healthcare; Chicago, IL, USA). Several studies have shown the superiority of CESM over FFDM [133] especially for patients with dense breasts. [74].

In a nutshell, supplemental modalities may be recommended in addition to FFDM, depending on the patient case and the radiologist decision. We recall that the first task of the radiologist when reading mammograms in the context of a breast cancer screening exam is to detect signs that may indicate the presence of a breast cancer. Hence, when reading mammography images, the radiologist searches for specific radiological findings which will be detailed in the next section.

2.2.3 Radiological findings in mammography images

The mammographic images allow to spotlight anomalies which, depending on their morphology, their number, their distribution and their evolution in time, imply a diagnosis of benign pathology or cancer. Hence, their detection and characterization are of great importance to decide recalling or not the woman during the screening phase, or deciding for a biopsy and providing the right treatment during the diagnostic phase. Radiologists are commonly using the BI-RADS (Breast Imaging Reporting and Database System) terminology established by the ACR (American College of Radiology) to de-

scribe the main characteristics of the detected findings, as summarized in Table 2.1.

Table 2.1: *Mammography lexicon of the significant findings.*

Radiological findings	Description		
Mass	**Shape**	oval-round-irregular	
	Margin	circumscribed-obscured-microlobulated-indistinct-spiculated	
	Density	fat-low-equal-high	
Asymmetry	asymmetry-global-focal-developing		
Architectural distorsion	distorted parenchyma with no visible mass		
Calcification	**Morphology**	typically benign	
		suspicion	1. amorphous 2. coarse heterogeneous 3. fine pleiomorphic 4. fine linear or fine linear branching
	Distribution	diffuse-regional-grouped-linear-segmental	

In BI-RADS terminology, a mass is a lesion occupying a 3D space seen in two different projections. If a potential mass is seen in a single projection, it should be called an 'asymmetry' until its three-dimensionality is confirmed. The shape of a mass correlates with the level of malignancy of the lesion. The more irregular is the mass, the higher is the probability of a cancer. A mass with well-circumscribed edges has a low probability being related to a cancer, while spiculated edges are strongly indicative of a cancer. Furthermore, the density of the mass is also an indicator of the level of malignancy of the lesion.

Contrary to masses, asymmetries lack convex outward borders and conspicuity as found in masses, according to BI-RADS third edition [144]. When such potential abnormality is detected, it is important to determine first whether it is really three dimensionally or just a projection of superimposed normal structures. Then, additional incidence with comparison with the opposite side of the breast are typically required for a better evaluation.

Architectural distortions correspond to a deviation, disharmony or rupture in the distribution of the conjunctivo-glandular dense tissue. They are associated to fibrous lesions which are generally difficult to detect (not visible enough and of small size). They may be detected by comparing the content in left and right breast images, or between current and prior images.

On histological examination, 50 to 80% of breast cancers have calcifications [72]. The latter ones are due to central necrosis, defined as a form of cell injury which results in the premature death of cells in living tissue, or secretions of malignant cells. Therefore, the detection of calcifications in mammography is of crucial importance for the early detection of breast cancers. Despite the relative high contrast of calcifications compared to the breast tissue, due to their high x-ray attenuation properties, their detection is difficult when they are of small size. In order to improve detectability, the radiologist resorts to different practices such as zooming or adjusting brightness and contrast of the images, acquiring magnified views to increase contrast and spatial resolution in order to visualize more calcifications and to better characterize their shape. Three important features are considered

to determine the malignancy of calcifications:

- The size
- The morphology
- The distribution in the breast

Based on the size, calcifications are either denoted macrocalcifications if their diameter is larger than 0.5 cm or microcalcifications if their diameter is less than 0.5 cm. Typically, macrocalcifications are benign while microcalcifications can be either benign or malignant according to their morphology as well as their distribution. Concerning the morphology, it remains the most important factor in differentiation between benign and malignant calcifications as illustrated in Figure 2.2 and 2.3 respectively.

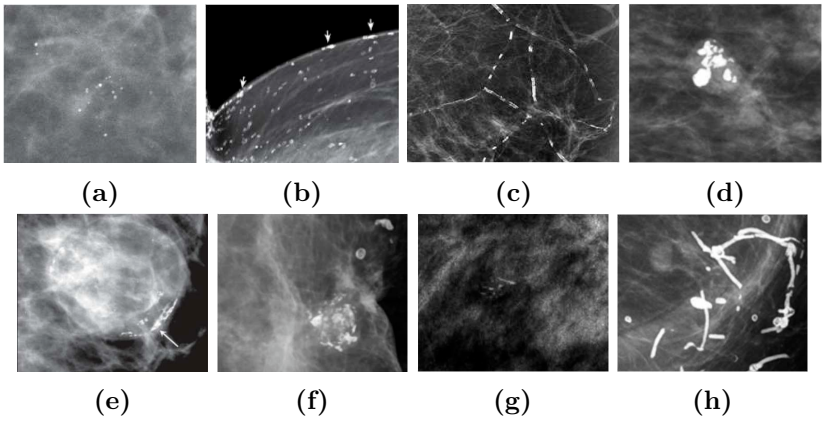

Figure 2.2: *Examples of typically benign calcifications [105].(a) Round. (b) Skin. (c) Vascular. (d) Coarse or popcorn-like. (e) Rim. (f) Dystrophic. (g) Milk of calcium. (h) Suture.*

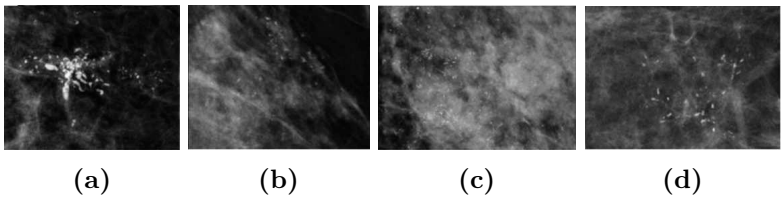

Figure 2.3: *Examples of calcifications with suspicious morphology [105].(a) Coarse heterogeneous. (b) Amorphous. (c) Fine pleomorphic. (d) Fine linear or fine linear-branching.*

Moreover, based on their distribution and number, the clustered arrangements are more or less suspicious. In the BI-RADS atlas, different

distributions are provided, as shown in Figure 2.4. Hereunder, the description of the arrangements are depicted, according to their increased risk of malignancy:

1. **Diffuse :** distributed randomly throughout the breast.
2. **Regional :** occupying a large portion of breast tissue > 2 cm.
3. **Grouped (historically cluster) :** few calcifications occupying a small portion of breast tissue; lower limit 5 calcifications within 1 cm and upper limit a larger number of calcifications within 2 cm.
4. **Linear :** arranged in a line, which suggests deposits in a duct.
5. **Segmental :** suggests deposits in a duct or in ducts and their branches.

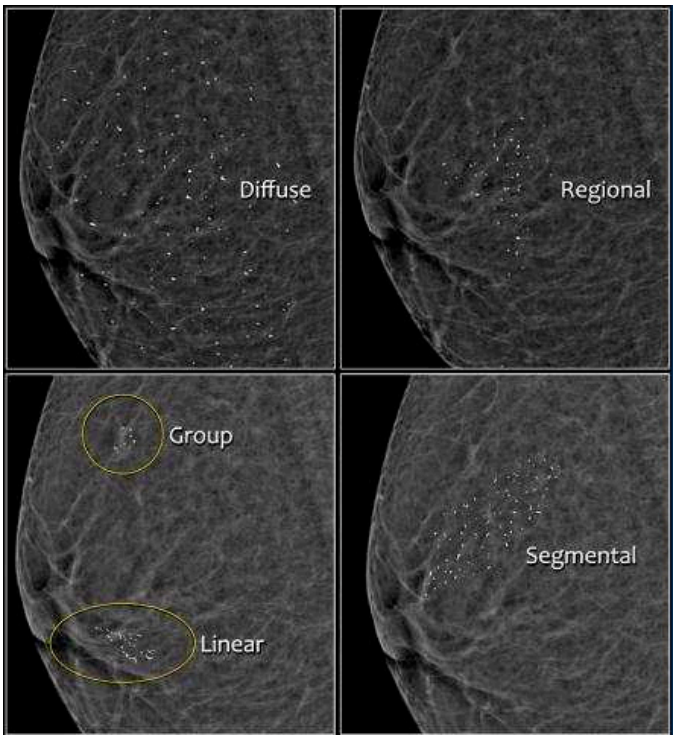

Figure 2.4: *Examples of different microcalcification distributions (BI-RADS for mammography and ultrasound 2013).*

One can thus understand that detection is a difficult task in mammography due to the large variability of radiological findings in size, shape and contrast. In particular, detection of microcalcifications is challenging due to their small size but also because they can be obscured by the breast tissues

especially in women with dense breasts. In this context, Section 2.2.4 is dedicated to discussing the impact of breast density on microcalcification detectability.

2.2.4 Impact of breast density on mammography performance

Besides the fact that detecting the radiological findings remains in itself a sensitive task for the radiologist, the breast density can impact the mammography performance, especially when it comes to microcalcification detectability. In the BI-RADS terminology, the breast density is classified into four categories as illustrated in Figure 2.5, according to their increased density [105].

- BI-RADS *a*: almost entirely fatty.
- BI-RADS *b*: there are scattered areas of fibroglandular density.
- BI-RADS *c*: the breasts are heterogeneously dense, which may obscure small masses.
- BI-RADS *d*: the breasts are extremely dense, which lowers the sensitivity of mammography.

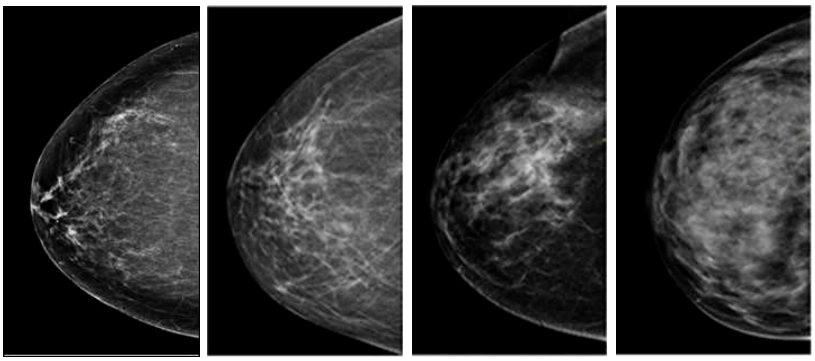

(a) **(b)** **(c)** **(d)**

Figure 2.5: *BI-RADS classification of breast density in mammography images : (a) almost entirely fatty. (b) scattered fibroglandular. (c) heterogeneously dense. (d) extremely dense.*

Breast density describes the amount of the fibroglandular tissue compared to the amount of the fatty tissue in the breast on a mammogram. Typically, the breast density is measured through a visual assessment by the radiologist when reviewing the mammogram [6]. The radiologist relies on the BI-RADS categorization, where she/he assigns mammograms to one of the four aforementioned classes.

So, the denser the breast, the greater the amount of fibroglandular breast tissue in the breast. This is illustrated in Figure 2.5 ranging from (a) to (d) with respect to the increased amount of fibroglandular breast tissue. Furthermore, the denser the breast, the poorer the sensitivity in FFDM. This is primarily explained by potentially occulting the lesions, especially microcalcifications, by the fibroglandular tissue [63]. One can infer that it is harder to detect microcalcifications in dense and textured breasts (i.e., BI-RADS *c* and *d*, illustrated in Figure 2.5(c) and (d) respectively).

Henceforth, microcalcification detection task is simultaneously important and very challenging when breast cancer screening is performed. This task is crucial since microcalcifications might be a sign of breast cancer when grouped and presenting some specific morphological and densiometric characteristic. Yet, it is very challenging due to the small size of microcalcifications and their low contrast when superimposed to dense areas of the breast. Our research work will be particularly focused in the enhancement of the detectability of microcalcifications. More precisely, we aim to improve this task in the recent modality called Digital Breast Tomosynthesis (DBT) which was introduced to curb the limitations of FFDM. Section 2.3 will be dedicated to thoroughly present DBT, explain its main features and advantages over FFDM thereby discussing its impact on microcalcification detectability. Finally, a presentation of the main contributions of this research work will be provided.

§ 2.3 Digital Breast Tomosynthesis (DBT)

2.3.1 Limitations of x-ray mammography

Even though x-ray mammography remains the current modality of choice for breast cancer screening and diagnosis, the detection may not be accurate enough, particularly for women with highly dense breasts. As explained in section 2.2.2, in a conventional FFDM exam of the breast, two x-ray images, from top-to-bottom (which corresponds to Cranio-Caudal (CC) view as in Figure 2.6(a)) and from angled side-to-side (which corresponds to Mediolateral oblique (MLO) as in Figure 2.6(b)), are acquired while the breast is compressed between the compression paddle and the detector. The acquisition of a projected view of the breast, as in FFDM, implies the superimposition of breast tissues which is the primary limitation of FFDM senstivity. The superimposition of tissues can reduce the visibility of lesions present in the breast or even completely occult them. This effect leads to a false negative (FN) error, that is the mammogram looks normal even though breast cancer is present [23]. This results in a lower detection rate in DBT than in FFDM [77]. The superimpostion of breast tissues may also generate structures that can mislead the radiological interpretations. For

instance, the overlapping of normal fibrosis tissue may mimic radiological findings and may lead to a false positive (FP) diagnosis [26]. This can result in undesirable recalls of women for further diagnostic tests, impelling to an increased patient anxiety [96].

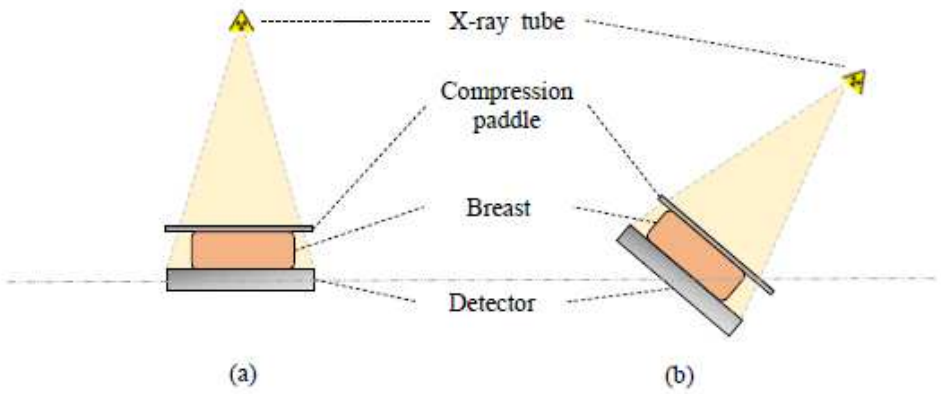

Figure 2.6: *(a) Cranio-caudal (CC) view (from top-to-bottom). (b) Medi-olateral oblique (MLO) view (from angled side-to-side).*

2.3.2 Advantages of DBT over x-ray mammography

Digital Breast tomosynthesis (DBT) was designed to partially alleviate the aforementioned major limitation of FFDM, induced by the tissue overlap. The acquisition geometry is very similar to that used in mammography, but with DBT, several projections of the breast are acquired enabling the reconstruction of a stack of images parallel to the detector plane corresponding to breast slices. During the acquisition process, the x-ray tube moves along an arc around the breast with a limited angular aperture, typically from 11° to 50°, whilst the detector remains stationary. A limited number of low-dose projection images are acquired so that the total dose to the patient is still comparable to the one in FFDM. In DBT, the number of projection images varies from 9 to 25 depending on the imaging system [120]. These two-dimensional projection images are then reconstructed, using a reconstruction algorithm, into a three-dimensional volume. Herein, the reconstruction algorithm is tailored so that it estimates the 3D distribution of the breast tissues using the projection images as the input data. Thus, the resulting volume consists of slices that present less superimposition of tissues compared to a standard x-ray mammography. A schematic of a DBT acquisition and an example of a reconstructed tomosynthesis volume is provided in Figure 2.7.

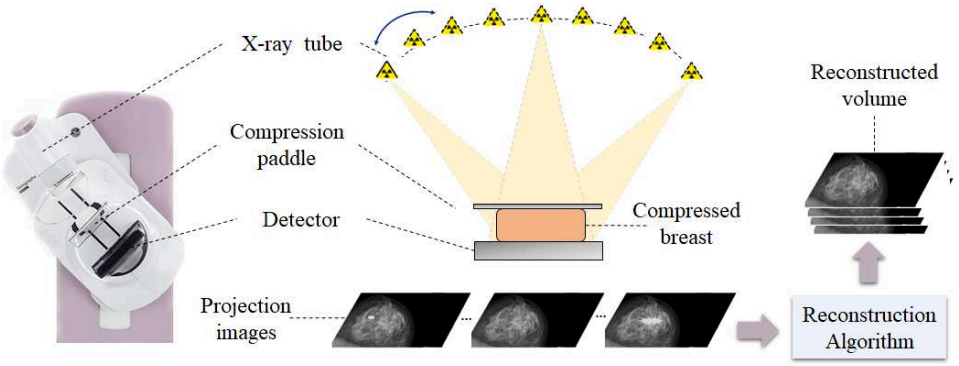

Figure 2.7: *A schematic of DBT acquisition process and reconstruction.*

Since DBT projections are acquired over a limited angular aperture, the DBT volume has a high isotropic resolution in the planes parallel to the detector and a much lower resolution in the perpendicular direction, i.e. the depth direction. It is worth mentioning that the in-plane resolution of the DBT slices is limited by the detector resolution. Due to the 3D nature of the DBT reconstructed volume, DBT has the potential to help reducing recall rates, improve the accuracy of breast cancer detection, and therefore improve the clinical performance particularly in dense breasts.

During the last decade, the current DBT systems have achieved significantly improved results towards greater acceptance of DBT as a viable alternative to conventional mammography. Several clinical studies have demonstrated that using DBT in stand-alone or DBT combined with FFDM for breast cancer screening results in an improvement of cancer detection rate and a decrease in false positive recall rate compared to FFDM alone. Thanks to the reduction of breast tissue overlapping, a better visibility and depiction of radiological findings are enabled. In this context, some studies have shown that DBT should enable a better differentiation between benign and malignant lesions [107]. Other comparative studies have demonstrated that lesions are better depicted in DBT which should enable more affirmative interpretations. This holds in particular for masses and architectural distortions in dense breasts [90, 24]. Furthermore, DBT provides a more accurate lesion localization [9].

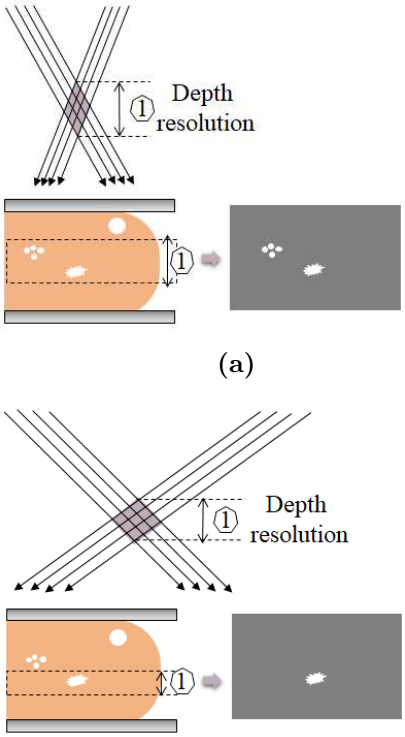

Figure 2.8: *(a) A schematic of a limited angular aperture resulting in a low depth resolution. (b) A schematic of a larger angular aperture resulting in a high depth resolution.*

Compared to standard mammography, DBT acquisition involves several additional parameters. The most important ones are those who defines the acquisition geometry of DBT, notably:

- The angular aperture covered by x-ray tube,
- The number of projections,
- The angular distribution of projections.

These parameters highly impact the resulting image quality and thus the performance of the clinical task. Current tomosynthesis systems use different geometrical parameters which shows the great complexity involved in optimizing these parameters.

It is expected that maximizing the angular aperture improves the depth resolution as illustrated in Figure 2.8(b). Not only lesions will be brought into a clear focus plane but also they will be better defined in the depth direction. However, it is worth mentioning that larger angular range may require

a longer acquisition time. This may result into more blur due to patient motion which can impact the overall image quality. Besides, decreasing the angular aperture would result in a lower depth resolution which may then reduce the visibility of lesions, as in slices shown in Figure 2.8(a). Yet, it has the advantage to enable a more acceptable acquisition time in DBT.

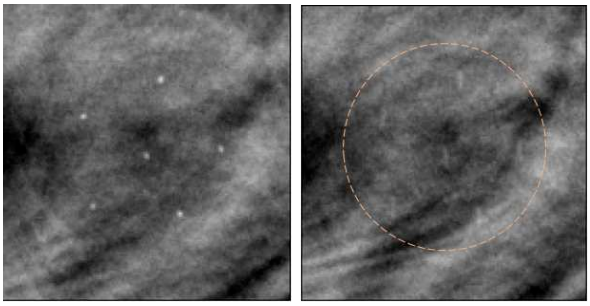

(a) **(b)**

Figure 2.9: *Examples of replication artifacts in DBT reconstruction.(a) Reconstructed DBT slice containing in-plane structure. (b) An adjacent reconstructed DBT slice containing an out-of-plane (cross-section of replication artifact) artifact.*

Increasing the number of projections and the angular range would result in a higher image quality. Nevertheless, increasing the number of projections is limited by the total exposure available for all the projections. This means that a higher number of projections will require the reduction of the exposure per projection. Hence, it will lead to lower signal-to-noise ratio in each projection and will result to a higher relative contribution of the detector electronic noise per projection. Furthermore, the distribution of the projections under a given angular aperture can result in out-of-plane artifacts or so-called replication artifacts. These latter are the most common artifacts in DBT. They present a replication of high-attenuation objects in every DBT reconstructed slice except for the slice in which the object is located [118, 119]. So, the fewer the number of projections, the more out-of-plane artifacts. An illustration of these artifacts is provided in Figure 2.9(b) presenting replications of structures originally located in a focal slice (as respectively depicted in Figure 2.9(a)). In DBT, several postprocessing algorithms have been developed for the purpose of removing these artifacts [138, 71].

2.3.3 Image review in DBT and its impact on microcalcification detectability performance

In contrast to the superiority of DBT over FFDM in terms of mass and architectural distortion detectability, microcalcification detectability remains

undoubtfully one of the limitations to be improved in DBT. Microcalcifications are harder to detect due to their characteristics and the impact of breast density on microcalcification detectability as detailed in Section 2.2.3 and 2.2.4 respectively. Therefore, a more comprehensive study of DBT is needed to better seize opportunities for improvement.

Several research studies have compared DBT with FFDM regarding microcalcification detection. Some of them have demonstrated that DBT was worse than FFDM, for accomplishing the aformentioned clinical task [129]. Others have shown that the results were comparable between DBT and FFDM [97, 113], or even DBT was better than FFDM [81, 53]. These different conclusions, may be explained by four major factors:

- The different inherent parameters of DBT acquisition systems,
- The different reconstruction algorithm,
- The different rendering of the reconstructed DBT volume,
- The different interpretative skills of the readers.

First, DBT image acquisition can be performed with a step-and-shoot or continuous motion of the x-ray tube. This can impact the level of blur in the acquired projections. Second, the acquisition time can differ depending on the angular aperture and the number of projections which can result in patient motion-based blur in the acquired projections. The reconstruction algorithms were also different in these studies which shows that it is one of the most important features impacting the microcalcification detectability in DBT. The inter-reader differences in such a clinical task may influence the error rates. Interpreting a DBT exam requires scrolling through and analyzing the DBT slices. Their number depends on the breast thickness. Since DBT is not yet approved as stand-alone, DBT exam typically combines reviewing DBT images and 2D mammography. Thereby compared to FFDM exam, it is not surprising that the interpretation time for each case is increased since there are more images to be reviewed. Thence, the needed extra time should be taken into consideration while processing DBT volumes. This is at the aim of easing the microcalcifications detectability task for the radiologist. So, it will significantly mitigate error rates in practice.

To reduce the review time, thicker slabs may be a potential alternative to slices in DBT volumes. To compute one slab, a number of reconstructed slices are combined, or “slabbed”, along the depth-direction. Therefore, the reader can scroll through a lower number of images during the DBT exam. The combining process can be performed, for example, by average intensity projection (AIP) approach or maximum intensity projection (MIP) method [55]. AIP approach tends to smooth images in the depth-direction, which lowers the noise level but also the contrast of small structures as

microcalcifications. On the other hand, both noise and visibility of microcalcifications increase with MIP technique. Groups of microcalcifications are better depicted in slabs as individual microcalcifications present in separated slices are regrouped in slabs. Each slice can be used in more than one slab, enabling a smoother transition when sifting through the DBT volume.

Although DBT acquisitions are low in dose, a combination of 2D mammography and DBT in a single exam increases patient radiation exposure. A potential method that has been recently developed to reduce the overall dose delivered to the patients and to reduce the reading time of DBT images is the creation of a 2D synthetic view of DBT volumes. Synthetized 2D mammography are constructed from the DBT images by applying a MIP-like algorithm that aims at condensing the DBT slices into a single 2D image.

The developed algorithms used to create synthetized 2D mammography are tailored to preserve small structures such as microcalcifications or spicules, which may sometimes be better visible compared with standard 2D mammography [69]. The 2D nature of synthetized mammography has the advantage of giving an overview of the breast, enabling to compare with previous exams, and particularly detecting cluster of microcalcifications which are generally not entirely located in a single DBT slice. Even though Food and Drug Administration (FDA) has approved synthetized 2D mammography since 2013 [69], it is not yet considered as a stand-alone substitution of 2D standard mammography. While several clinical studies have shown that no significant differences were noted in terms of recall rates, cancer detection, and diagnostic accuracy when combining synthetized 2D mammography and DBT compared with combining conventional FFDM with DBT [126, 34], further developing of more efficient algorithms is needed for synthetized 2D mammography.

To sum up, the shortcomings of FFDM have led to a stronger interest to DBT. As discussed before, DBT provides a 3D volume with less breast tissues overlapping that enables a better detectability of radiological findings compared to FFDM. Due to the several aforementioned reasons, no consensus is inferred on microcalcification detectability performance with DBT when used as a stand-alone modality compared with FFDM. The introduction of slabs and synthetized 2D mammography in the clinical use may have a great potential towards an increased acceptance of DBT combined with synthetized 2D mammography as a viable alternative to FFDM. Today, several issues are remaining, thereby providing opportunities for further research. If DBT performance is at least as effective as FFDM in microcalcification detection, one of the primary aims of the research should be to address the rendering of DBT volume such that it would efficiently impact reviewing DBT images hence improves the radiologist performance. It seems that the screening interpretive process requires visual pattern recognition when scanning a high volume of images. Therefore, enhancing microcalcification

detectability in DBT requires the integration of the radiologist performance associated to microcalcification detectability in the reconstruction procedure of DBT volumes. One can infer that the reconstruction algorithm plays a key role in this context. A new formulation of a reconstruction algorithm based on the microcalcification detectability task, considered as the clinical task to be improved in DBT, should be further investigated. Section 2.4 will discuss state of the art reconstruction approach in DBT and present the motivation of the contribution of this work.

§ 2.4 Inverse problem approaches in image reconstruction

The objective of DBT reconstruction is to recover the volumetric distribution of linear attenuation coefficients $\mu(r)$ from the measured log-projections at various angles. These measurements are modeled, by developing the Beer-Lambert's law setting (equation (2.1)), by integrals along lines that reads

$$p_\theta(x,y) = -\ln \frac{I_\theta(x,y)}{I_0} = \int_{r \in L_\theta(x,y)} \mu(r)\, \mathrm{d}r \tag{2.2}$$

where $L_\theta(x,y)$ denotes the x-ray beam path between the x-ray source and the position (x,y) on the detector under the angle of view θ. $I_\theta(x,y)$ is the x-ray photon intensity at the position (x,y) on the detector under the angle of view θ and $p_\theta(x,y)$ is the measurement of the log-projection at the position (x,y) under the angle θ. Various approaches were developed to analytically or iteratively resolve the inversion of equation (2.2). In this section, several reconstruction methods will be briefly reviewed.

2.4.1 Analytical methods : Filtered Back-Projection (FBP)

Analytical methods are based on the mathematical inversion of equation (2.2), which is equivalent to the *Radon Transform*. Filtered backprojection is the most commonly known analytical algorithm for DBT [119]. Its name comes from the fact that this method involves two steps : a filtering step and a backprojection step. The backprojection step is based on the traditional Shift-and-Add (SAA) algorithm [103]. Mathematically, the backprojection is the transpose operator of a forward projection which is based on a discretization of the continuous operator of *Radon Transform*, while incorporating the DBT imaging geometry. More precisely, it consists in smearing back the line integrals to the 3D voxelized volume, by analyzing the breast structures displacement in the projections.

With the setup of DBT acquiring very limited projections, the Fourier domain of the imaged breast is sampled such that the low frequencies are

sampled much more densely than the high ones. This explains why a simple backprojection results in a blurry reconstruction. The filtering phase consists in applying well-designed filters to the projection data with the aim of sharpening details while reducing the noise [54, 119]. In practice, the filtering phase is performed before the backprojection since it is computationally more efficient and it can drastically impact the quality of the reconstruction [119]. A schematic of the difference between simple backprojection and filtered backprojection is depicted in Figure 2.10(a) and (b) respectively.

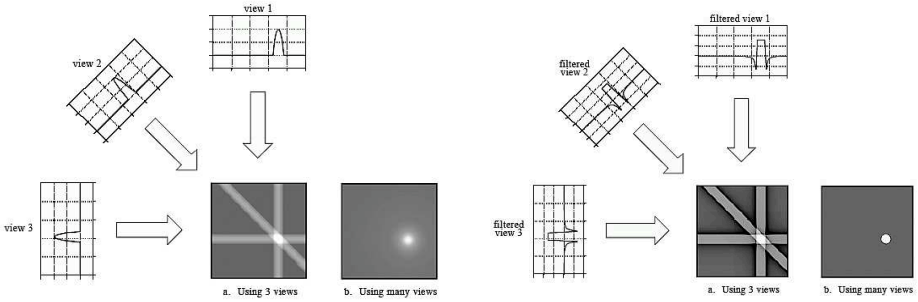

(a) **(b)**

Figure 2.10: *A schematic of the difference between simple backprojection and filtered backprojection reconstruction. (a) Simple backprojection resulting in a blurry version of the original image. (b) Filtered backprojection resulting in reduced blurs seen in the simple backprojection method.[127]*

Limits of the analytical methods :

Reconstruction with FBP method requires that the discrete projection operator accurately represents the continuous operator of *Radon Transform*. Some authors have shown that the number of projections should be roughly equal to the number of rays in each projection [75, 102], with

$$M_{proj} \geq \frac{\pi}{2} N_{rays} \tag{2.3}$$

where M_{proj} denotes the number of projections and N_{rays} is the number of rays per projection. Equation (2.3) can be seen as a consequence of the Shannon-Nyquist sampling criterion. In practice, $M_{proj} \approx N_{rays}$ may be roughly sufficient in most cases without causing subsampling artifacts. However, in DBT, the reconstruction volume involves a highly limited number of projections, i.e. $M_{proj} \ll N_{rays}$, due to several experimental constraints (radiation dose concern, design of the imaging system, etc.). This violates the Shannon-Nyquist sampling criterion. Moreover, more advanced methods are required to improve the Signal to Noise Ratio (SNR) of the reconstructed volumes in case of projections with low SNR. This explains the interest of the research community for iterative reconstruction approaches.

2.4.2 Algebraic Reconstruction Technique (ART)-based iterative methods

Several algebraic methods have been developed for the DBT reconstruction problem. In contrast to analytical approach, these methods rely on the iterative resolution of a system of simultaneous linear equations. To infer the latter set of linear equations, equation (2.2) is approximated by the following linear form,

$$p = Ad \tag{2.4}$$

where $p \in \mathbb{R}^n$ is a vector that denotes the projections data, $d \in \mathbb{R}^m$ is a vector that represents the DBT volume to be reconstructed and $A \in \mathbb{R}^{n \times m}$ is the forward projection matrix that depicts the DBT geometry system. So, equation (2.4) is equivalent to a set of n linear equations of m unknowns.

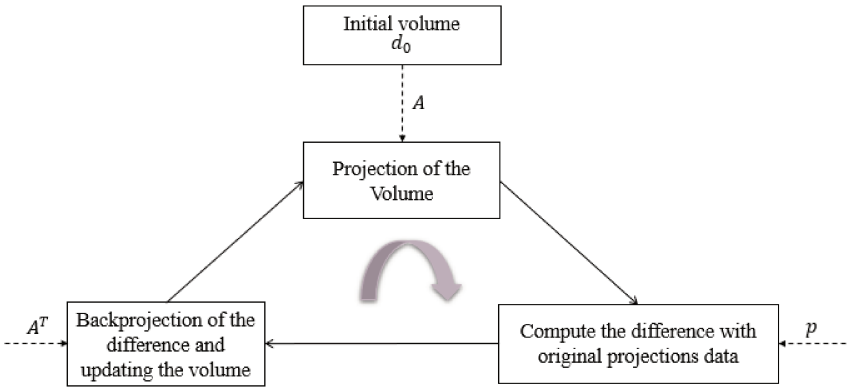

Figure 2.11: *A schematic of the general steps of ART-based methods.*

ART-based methods basically share the same backbone which involves three steps: forward projection of the volume, computing the error between the projected volume and the original acquired projections data, backprojecting the error and updating the volume. A schematic of the general steps of ART-based methods is illustrated in Figure 2.11. The update rule differs leading to the different ART-based methods [5]. For instance, the update rule in ART involves updating the volume ray per ray of each projection. A more refined version of the ART is the Simultaneous Algebraic Reconstruction Technique (SART) which involves all the rays in a projection at each volume update. Therefore, it provides a better convergence rate, though with a higher cost per iteration. Another ART-based method is Simultaneous Iterative reconstruction technique (SIRT). Unlike SART, all the projections are taken into account to update one voxel of the reconstructed volume. It is performed by backprojecting the mean of all the error

projections. At the expense of slower convergence, SIRT leads usually to a better reconstruction than the one obtained by the ART method.

Though ART-based iterative methods may present many advantages, they may not be ideally suitable for DBT reconstruction. In fact, these iterative algorithms are designed for reconstruction problems from complete acquired projections data. Conversely, the acquired projections are highly incomplete in DBT which yields to one among many solutions of equation (2.4), due to the under-determination of the reconstruction problem. Therefore, more advanced methods should be considered to alleviate the missing information issue in which ART-based methods make little effort. In this context, algorithms based on the minimization of an objective function including constraints and regularization, usually offers a good alternative.

2.4.3 Least square estimation

From a mathematical point of view, the reconstruction of the volume image from DBT measurements is a special instance of linear inverse problem. Beer-Lambert's law modelling the x-ray transmission process (equation (2.2)) leads to the following linear forward projector with a noise model

$$p = Ad + e \tag{2.5}$$

where $p \in \mathbb{R}^n$ is a vector derived from the acquired projections, $d \in \mathbb{R}^m$ is a vector representing the DBT volume to be reconstructed, $A \in \mathbb{R}^{n\times m}$ is the forward projection matrix describing the geometry of the DBT system, and $e \in \mathbb{R}^n$ is assumed to be a realization of a zero-mean white Gaussian noise. Then the probability of observing the acquired projections p given the unknown d is depicted as

$$\mu_{P|D=d}(p) = \frac{1}{(2\pi\sigma^2)^{\frac{n}{2}}} \exp\left(\frac{-\|Ad-p\|^2}{2\sigma^2}\right) \tag{2.6}$$

where $\mu_{P|D=d}(p)$ denotes the likelihood for observing p given d, and σ assumed to be the noise standard deviation. Thence, the Maximum Likelihood (ML) algorithm aims at maximizing the quantity (2.6) with respect to the unknown volume d, so that the acquired projections p correspond to the most probable observed signal. By applying the negative logarithm on (2.6), we obtain a quadratic term related to the data fidelity term as following:

$$-\log \mu_{P|D=d}(p) \propto \frac{1}{2\sigma^2}\|Ad-p\|^2 \tag{2.7}$$

ML algorithm becomes then equivalent to minimizing the negative log-likelihood as following,

$$\underset{d\in\mathbb{R}^m}{\text{minimize}} \quad \frac{1}{2}\|Ad-p\|_2^2. \tag{2.8}$$

Note that in equation (2.8) the multiplicative factors involving σ are simplified, since they do not depend on d. So by developing the minimization problem 2.8, we obtain the least square solution under the following closed-form formula,

$$d = (A^\top A)^{-1} A^\top p \tag{2.9}$$

The solution obtained in equation (2.9) to recover d is nothing but a least-square solution. Nevertheless, the latter one is never computed directly since the matrix $(A^\top A)$ is often ill-conditioned or even not invertible, thereby an efficient regularization strategy is needed.

Even though several efficient algorithms are provided to solve the latter minimization problem, the least square solution likely yields to a noisy DBT reconstruction. This is due to the ill-conditioning of the projection matrix A where the noise tends to be amplified even if it is present in tiny amounts in the input projections data. The key is to modify equation (2.8) such that the solution to the new problem is less sensitive to the perturbations. To this end, several research studies have investigated regularized reconstruction approaches which will be further detailed in Section 2.4.4.

2.4.4 Regularized reconstruction approach

As already stated, the least square estimation is related to the maximum likelihood (ML) estimate given a noise model. It does not take into consideration any prior knowledge on the latent space, which is the volume space in DBT context. Although problem (2.8) is well-posed in Hadamard sense [67] (i.e. the solution exists, is unique, and depends continuously on the input data), the ill-conditioning of the operator A makes the computation of the solution d sensitive to perturbations in the input data p. Henceforth, a regularization should be considered, incorporating prior knowledge on the solution whereby computing a Maximum A Posteriori (MAP) solution rather than the ML one. In DBT, MAP methods aim at maximizing the posterior probability density of the unknown volume d given the projections p under the Bayesian setting,

$$\mathsf{p}(d \mid p) = \frac{\mathsf{p}(p \mid d)\mathsf{p}(d)}{\mathsf{p}(p)} \propto \mathsf{p}(p \mid d)\mathsf{p}(d) \tag{2.10}$$

where $\mathsf{p}(d \mid p)$ denotes the posterior probability density, $\mathsf{p}(p \mid d)$ is the likelihood of observing the projections p knowing the volume d and $\mathsf{p}(d)$ is the prior probability corresponding to the prior knowledge on d. In the same manner than for ML solution, maximizing equation (2.10) is equivalent to minimizing the negative log-likelihood which entails to solving the following problem, again assuming Gaussian noise model :

$$\underset{d \in \mathbb{R}^m}{\text{minimize}} \quad \frac{1}{2}\|Ad - p\| + g(d). \tag{2.11}$$

where the first term denotes the data fidelity term that measures the distance between the projections issued from the solution Ad and the acquired projections p. Herein, g represents a function that encodes prior knowledge on the solution. In other terms, the first term in problem (2.11) is based on the noise model and g is based on the prior knowledge in the latent space. So, the MAP solution is a trade-off between the likelihood to the observed projections p and the prior knowledge on the unknown volume d. Thence, a potential strategy to improve DBT reconstruction is to solve the regularized problem (2.11) satisfying these requirements:

- Well-posed in Hadamard sense [67],
- Consistent with the original problem which means that the solution should belong to the solution space of the original problem,
- Reaching a reasonable trade-off between computational complexity and solution quality.

Several research studies have investigated different regularization functions to improve the overall image quality in DBT or likewise in limited view reconstruction [132, 49]. Among the proposed regularization functions, total variation regularization [122, 124, 111], total p variation regularization [123, 124], joint entropy regularization [134], adaptive diffusion regularization [87]. Note that these regularizations will be further discussed in Section 4.9.

Even though these regularization functions may provide a certain trade-off in terms of image quality in DBT, they do not account for a specific clinical task such as the microcalcification detectability as explained in Section 2.3.3. More precisely, the radiologist performance associated to microcalcification detection while reviewing DBT volumes has not been directly formalized in the reconstruction procedure of DBT images, so far. In this context, the advantage of regularized approaches as detailed in problem (2.11) is to integrate regularization functions encoding some relevant prior knowledge in the latent space, tailored for a specific task. Henceforth, modeling novel prior terms based on the aforementioned clinical task and integrate them in a regularized iterative reconstruction approach will be the core contribution of our research work.

§ 2.5 Summary

While DBT demonstrated its clinical superiority over FFDM, its performance in terms of microcalcification detectability did not yet reached consensus in the medical community. Microcalcification detection is a very

challenging task due to their small size and their potential relative low contrast in dense areas of the breast. In addition, DBT presents geometric limitations partially addressed in iterative reconstruction algorithms.

In classic regularization approaches used in DBT reconstruction, such as total-variation (TV), penalization cost functions are applied the same way on each voxel of the reconstructed volume. In order to preserve contrast and shape of microcalcifications while reducing the noise in other tissues, we propose to reformulate the reconstruction method such as it maximizes the clinical task (detection of microcalcifications) taking into consideration the anatomical specificities within the breast. Instead of minimizing a discrepancy function, we seek to minimize a penalized least squares cost function encoding some clinically meaningful prior knowledge.

We will then establish a novel variational reconstruction framework in DBT which aims at simultaneously enhancing the microcalcification detectability performance and enabling a high quality restoration of the breast tissues.

- Chapter 3 -

A new approach for microcalcification enhancement in DBT reconstruction

§ 3.1 Introduction

As mentioned in Section 2.3.3, the detection performance in breast cancer screening highly depends on the ease for the radiologist to detect microcalcifications within the analyzed DBT images. We aim then at introducing a new reconstruction procedure in order to help the radiologist for this task. Hence, our DBT reconstruction method will be formulated to maximize the microcalcification visibility. The detectability task can be efficiently assessed by using anthropomorphic model observers [135, 112]. Anthropomorphic model observers refer to mathematical observer models that were developed to assess image quality for a specific clinical task [12]. These observers mimic the human observer for such a task, in contrast with ideal observers (IOs) which assume a full knowledge of the statistics of the image [109]. In essence, by applying an anthropomorphic model observer to a given image, one would obtain as an output a scalar decision variable that determines how detectable is the lesion for the radiologist. We will construct our clinical-task based function by following this principle.

In this chapter, we first explain our proposed reconstruction approach in DBT in Section 3.2. Then, we detail the construction of the clinical task based a priori term used in this approach in Section 3.3. Finally, by incorporating the clinical term in an optimization framework, we will show the potential interest of our method compared with standard DBT reconstructions on both clinical and physical phantom data in Section 3.4.

§ 3.2 Reconstruction problem in DBT

3.2.1 Problem statement

A typical workflow that involves the lesion detection task in a context of breast cancer screening using DBT is illustrated in Figure 3.1. This workflow includes all the steps from data acquisition to detection task. Once the DBT volume is reconstructed and post-processed, if needed, the radiologist searches over the regions of interest within the DBT volume with multiple eye movements fixating at points of interest. Then, (s)he decides whether a group of microcalcifications is present or absent binary decision. There are several downsides when performing these different steps independently from each other. Within this configuration, each single step is prone to introduce approximations that are not necessarily taken into consideration by subsequent steps. In particular, the reconstruction step may not consider the end clinical task performed by the radiologist. Most reconstruction algorithms are focused on producing good image quality, but not images enabling clinical performance improvement of the radiologist in a specific task such as radiological finding detection.

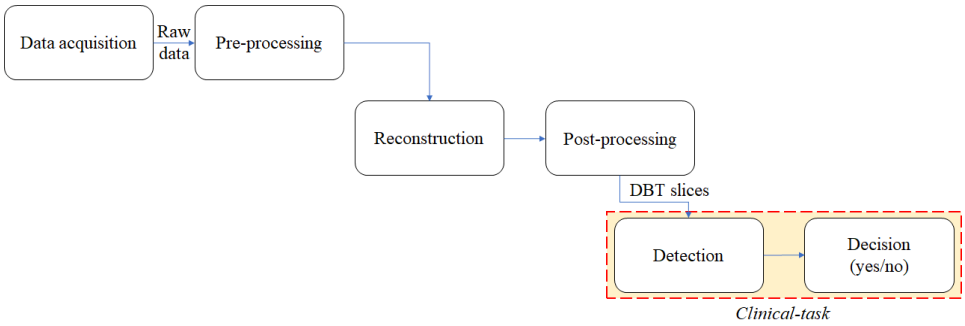

Figure 3.1: *Schematic of a typical workflow involving lesion detection task in DBT. First row: raw data is acquired and pre-processed, resulting in log-projections as detailed in equation (2.2). Second row: the pre-processed data is used as input to a reconstruction algorithm then potentially followed by a post-processing step, if needed, in the aim of delivering a DBT volume with a sufficient image quality. Third row: The reconstructed DBT slices are used by the radiologist to perform the clinical task.*

It is therefore natural to be confronted with the question of how to integrate the end clinical task in the reconstruction process to improve this clinical performance. More precisely, the right question that should be asked would merely be:

How to reformulate the reconstruction step when the screening involves a human observer and a given clinical task ?

3.2.2 Proposed clinical-task based reconstruction in DBT

A potential answer to the above question is to consider a new approach for the reconstruction step of the workflow sketched in Figure 3.1. In this context, task adapted reconstruction was proposed in tomographic imaging where the reconstruction step is associated with feature extraction task [3]. Hence, we propose to introduce a new DBT reconstruction approach, the *clinical-task based reconstruction* (CTBR) as illustrated in Figure 3.2. This novel method integrates the reconstruction procedure with the radiological performance associated with a given clinical task. The objective is then to maximize the radiological performance for the predefined clinical task at hand. The key is to mathematically model an a priori term that takes into consideration the pre-processed data and the clinical task performed by the radiologist. Once formulated, this term will be incorporated into the reconstruction algorithm through an optimization framework which will be further detailed within this section.

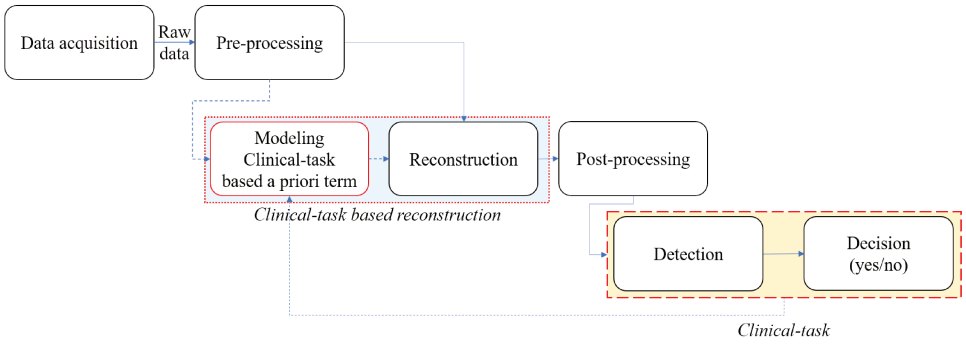

Figure 3.2: *A schematic of our proposed DBT workflow involving a clinical-task (detection of microcalcifications) in DBT. The first and the third rows remain the same as illustrated in Figure 3.1. In the second row, the proposed clinical-task based reconstruction comprises two steps: 1) modeling of the clinical task based a priori term, 2) integration of this clinical-task term in a cost function which is minimized for 3D reconstruction of DBT volumes. The final outcome of this step is a DBT reconstructed volume that maximizes the radiological performance for the predefined clinical task at hand.*

More precisely, as depicted in the blue dotted rectangle in Figure 3.2, the pre-processed data and the clinical task to be performed by the radiologist are considered as inputs to model the clinical-task based term. Thereby, the resulting a priori term will be fed to the reconstruction algorithm within the pre-processed data whereby outputting a DBT volume that maximizes the clinical task which would enhance the performance of the radiologist. To delve into the proposed clinical-task based reconstruction illustrated in the blue dotted rectangle in Figure 3.2, we propose to consider the following

four major steps :

1. Detecting the lesion, which is defined as the signal of interest, in the considered DBT volume.
2. Defining the regions of interest (ROIs) that are occupied by the potential detected lesion in the DBT volume.
3. Defining the detection task on the ROIs as a binary hypothesis test, by mimicking the human observer.
4. Formulating the detectability function which will be incorporated as an a priori term in an optimization framework of DBT reconstruction.

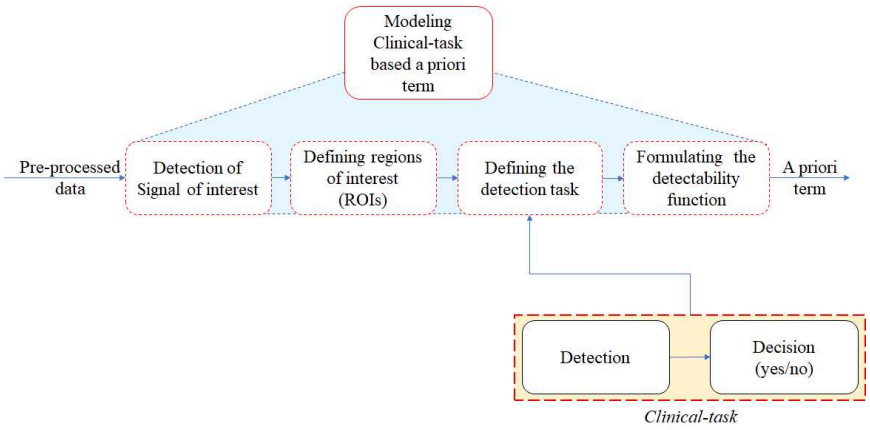

Figure 3.3: *Detailed steps of modeling the clinical-task based a priori term.*

In our context, the signal of interest is the microcalcifications and the clinical task is their detection in the DBT volume. Following the steps in Figure 3.3, we now provide a comprehensive explanation of the mathematical formalism of the clinical task-based a priori term. For conciseness, we will refer to clinical-task based a priori term as detectability function in the following.

§ 3.3 Construction of the detectability function

3.3.1 Anthropomorphic mathematical observer as a model of the clinical task

Let us consider a set of q vectors $(r^i)_{1\leq i\leq q}$ of intensity values in regions of interest from a volume $d \in \mathbb{R}^m$ where, for every $i \in \{1, ..., q\}$, $r^i \in \mathbb{R}^k$ with

$k \leq m$, is the vector defining a zone where a microcalcification is potentially present. For every $i \in \{1, \ldots, q\}$, let us introduce the decimation operator S_i that extracts a region of interest r^i from the volume d as follows:

$$\begin{aligned} S_i &: \mathbb{R}^m \to \mathbb{R}^k \\ d &\mapsto r^i = (d_j)_{j \in \mathbb{I}^i}, \end{aligned} \tag{3.1}$$

where each $\mathbb{I}^i$ denotes the set of indices of k voxels related to each region of interest r^i. For simplicity, we will assume that these regions do not overlap, i.e., $\forall (i,j) \in \{1, ..., q\}^2, \mathbb{I}^i \cap \mathbb{I}^j = \varnothing \, \text{if} \, i \neq j$. By imposing this condition, we will be able to avoid signal from background and signal with signal overlapping. Concerning the first case, we enable a better recovery of the detectability measure for the signal of interest (microcalcifications) in our proposed detectability function. With the second one, we enable a more robust separation between microcalcifications located in different regions of interest.

Following the approach used in channelized Hotelling observer (CHO) [112], itself an extension of Hotelling observer (HO) [12], each r^i is channelized into c discriminative features through a decomposition matrix $U \in \mathbb{R}^{k \times c}$ where each column denotes a single channel with size equal to the one of the original region of interest. Thereby, we obtain a feature vector $v^i = U^\top r^i$ (Figure 3.4). The channelization process is crucial for two reasons. First, it allows to simplify the computation complexity in HO by greatly reducing the dimension of the input images when $c \ll k$, [100]. Second, it was demonstrated that the channelization mechanism enables to model characteristics of the human visual system in certain conditions by choosing adequate channel filters [108, 135, 68].

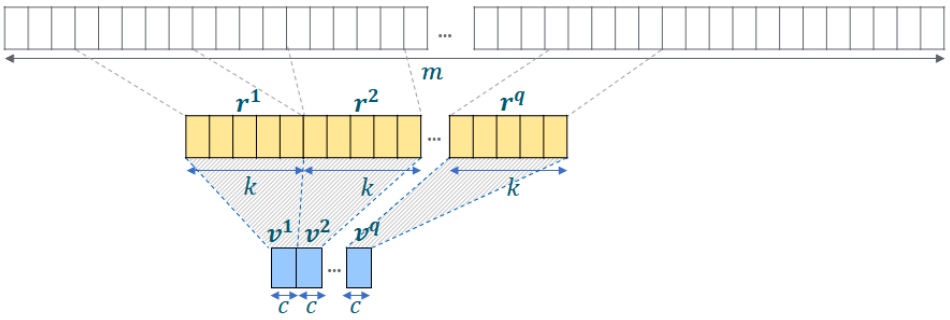

Figure 3.4: *Detailed steps of the channelizing process. The first row presents the vectorized volume $d \in \mathbb{R}^m$. The second row denotes the ROIs $(r^i)_{1 \leq i \leq q}$ with size k each, extracted using the decimation operator in (3.1). The third row depicts the resulting feature vectors $(v^i)_{1 \leq i \leq q}$ when applying the channelization process on the initial ROIs $((r^i)_{1 \leq i \leq q})$.*

We are now ready to formulate our detectability criterion. Consider

an index $i \in \{1, \dots, q\}$, and the associated vectors r^i and v^i. The detection task can be expressed as a binary hypothesis test, defining $\mathcal{H}_0$ for microcalcification-free signal and $\mathcal{H}_1$ the presence of a microcalcification. More precisely, the following two statistical cases have to be distinguished for r^i:

$$\begin{cases} \mathcal{H}_0 : & r^i = b^i + \gamma^i \\ \mathcal{H}_1 : & r^i = \mu^i + b^i + \gamma^i \end{cases} \tag{3.2}$$

where b^i, μ^i, and γ^i are real-valued variables that model the background, the signal of interest (i.e., microcalcification) and the noise, respectively. Under the assumption of a zero-mean multivariate Gaussian noise, the detectability is defined by maximizing the log-likelihood ratio under the hypotheses (3.2),

$$R = \sum_{i=1}^{q} \log\Big(\frac{\mathsf{p}(v^i \mid \mathcal{H}_1)}{\mathsf{p}(v^i \mid \mathcal{H}_0)}\Big), \tag{3.3}$$

Hereabove, $\mathsf{p}(v^i \mid \mathcal{H}_1)$ (resp. $\mathsf{p}(v^i \mid \mathcal{H}_0)$) designate for the probability density function of v^i in the presence (resp. absence) of microcalcification, that read

$$\begin{aligned} \mathsf{p}(v^i \mid \mathcal{H}_1) &= \frac{1}{\sqrt{(2\pi)^c |\Sigma|}} \exp -\frac{1}{2}\Big((v^i - U^\top(b^i + \mu^i))^\top \Sigma^{-1}(v^i - U^\top(b^i + \mu^i))\Big) \\ \mathsf{p}(v^i \mid \mathcal{H}_0) &= \frac{1}{\sqrt{(2\pi)^c |\Sigma|}} \exp -\frac{1}{2}\Big((v^i - U^\top b^i)^\top \Sigma^{-1}(v^i - U^\top b^i)\Big) \end{aligned} \tag{3.4}$$

where Σ denotes the covariance matrix of the channelized noise. In order to compute this matrix, we need to estimate the sample means of the feature vectors v^i conditioned to both hypotheses. This enables the computation of R in equation (3.3). It is worth noticing that computing the maximum likelihood ratio for a single image is similar to computing the template of a channelized model observer which is obtained by *linear discriminant analysis* [60]. Let us consider two training datasets F_0 and F_1 with cardinalities t_0 and t_1 respectively:

$$\begin{aligned} F_0 = &\ \{\tilde{r}^j_{|\mathcal{H}_0} \in \mathbb{R}^k \mid j \in \{1, \dots, t_0\}\} \\ F_1 = &\ \{\tilde{r}^j_{|\mathcal{H}_1} \in \mathbb{R}^k \mid j \in \{1, \dots, t_1\}\}, \end{aligned} \tag{3.5}$$

We can then infer, for every $\ell \in \{0, 1\}$ and $j \in \{1, \dots, t_\ell\}$, the channelized image as follows:

$$\tilde{v}^j_{|\mathcal{H}_\ell} = U^\top \tilde{r}^j_{|\mathcal{H}_\ell}. \tag{3.6}$$

The estimation of the covariance matrix Σ of the channelized noise is deduced by

$$\Sigma = \frac{1}{t_0 + t_1} \sum_{\ell=0}^{1} \sum_{j=1}^{t_\ell} \Big(\tilde{v}^j_{|\mathcal{H}_\ell} - \bar{\tilde{v}}_{|\mathcal{H}_\ell}\Big)\Big(\tilde{v}^j_{|\mathcal{H}_\ell} - \bar{\tilde{v}}_{|\mathcal{H}_\ell}\Big)^\top, \tag{3.7}$$

where

$$\bar{\tilde{v}}_{|\mathcal{H}_\ell} = \frac{1}{t_\ell} \sum_{j=1}^{t_\ell} \tilde{v}^j_{|\mathcal{H}_\ell}, \quad \ell \in \{0,1\}. \tag{3.8}$$

For practical simplicity, we can consider $t_1 = t_0$. As mentioned before the channel mechanism enables the simplification of the computation of the inverse of covariance matrix compared to HO by greatly reducing the dimension of the training regions of interest [100] and requires fewer training images than HO [139]. Now, based on expressions (3.2), we are able to calculate the log-likelihood ratio in (3.3) as follows :

$$\begin{aligned} R &= \sum_{i=1}^{q} -\frac{1}{2} \left(v^i - U^\top (b^i + \mu^i)\right)^\top \Sigma^{-1} \left(v^i - U^\top (b^i + \mu^i)\right) \\ &+ \frac{1}{2} \left(v^i - U^\top b^i\right)^\top \Sigma^{-1} \left(v^i - U^\top b^i\right) \\ &= \sum_{i=1}^{q} \frac{1}{2} \left((b^i + \mu^i)^\top U \Sigma^{-1} v^i + (v^i)^\top \Sigma^{-1} U^\top (b^i + \mu^i)\right) \\ &- \frac{1}{2} \left((b^i)^\top U \Sigma^{-1} v^i - (v^i)^\top \Sigma^{-1} U^\top b^i + (\mu^i)^\top U \Sigma^{-1} U^\top \mu^i\right). \end{aligned} \tag{3.9}$$

The fact that Σ^{-1} is a symmetric matrix leads to the following simplification:

$$R = \sum_{i=1}^{q} (\mu^i)^\top U \Sigma^{-1} U^\top r^i - \frac{1}{2} (\mu^i)^\top U \Sigma^{-1} U^\top \mu^i. \tag{3.10}$$

Since the μ^i's are fixed, the quantity to be maximized using (3.1) is

$$\begin{aligned} (\forall d \in \mathbb{R}^m) \quad D(d) &= \sum_{i=1}^{q} (\mu^i)^\top U \Sigma^{-1} U^\top S_i d \\ &= \mu^\top \sum_{i=1}^{q} S_i^\top U \Sigma^{-1} U^\top S_i d, \end{aligned} \tag{3.11}$$

where $\mu = \sum_{i=1}^{q} S_i^\top \mu^i$. The last equality has been derived from the properties of the operators S_i and the assumption that the ROIs do not overlap. This yields our clinical-task based penalization term for the detectability of the microcalcifications in any reconstructed volume $d \in \mathbb{R}^m$. In practice, the ROIs location as well as the signal of interest vector μ will be derived from an intermediate reconstructed volume d^* as detailed next.

3.3.2 Detection map based on a Computer-Aided Detection approach

The evaluation of the proposed detectability function (3.11) requires the construction of detection maps composed of :

- The ROIs determining the location of potential microcalcifications,
- The signal of interest μ and the associated covariance matrix Σ. We highlight that the signal of interest μ corresponds to the volume d in which only the voxels of the ROIs μ^i are not equal to zero.

To this aim, a possibility is to resort to Computer-Aided Detection tools [41] that have the ability to locate suspicious structures in a medical image. Following classical approaches which were developed to identify findings based on their size [136], we implement our detectability function to be specifically suited to the detection of lesions with a size in a specific range. We thus propose a strategy for the construction of signal μ, and the associated regions of interest $(\mathbb{I}^i)_{1\leq i\leq q}$ from a total-variation (TV) based reconstructed volume. Note that TV amounts to a piecewise constant image [104], thus yielding to a segmented volume in our context. Furthermore, the covariance matrix Σ will be learnt using training datasets as described in Section 3.3.2.

Let detail the proposed approach for estimating the signal. In order to build the signal μ, we rely on the resolution of a constrained optimization problem where positivity and total-variation constraints are introduced. More precisely, we consider the following formulation of our problem:

$$\underset{\substack{d\in[0,+\infty[^m\\ \Delta d\in B_{1,2}(0,\zeta)}}{\text{minimize}} \quad \frac{1}{2}\|p-Ad\|^2, \tag{3.12}$$

where $\Delta \in \mathbb{R}^{3m\times m}$ is the discretized gradient operator along the 3 spatial dimensions,

$$B_{1,2}(0,\zeta) = \{\delta \in \mathbb{R}^{3m} \mid \|\delta\|_{1,2} \leq \zeta\}, \tag{3.13}$$

$\|\cdot\|_{1,2}$ denotes the $\ell_{1,2}$ norm, and $\zeta > 0$ is a preset constraint bound on the total-variation of the volume.

The objective function in Problem (3.12) is convex, but it has to be minimized under constraints. To solve this minimization problem, we resort to a parallel forward-backward based Primal-Dual approach [78]. This approach presents the advantage of a reduced complexity per iteration since, in particular, linear operator inversion is not required, while ensuring convergence guarantees. Another lead advantage is that it can successfully be applied in convex optimization problems involving both smooth and nonsmooth functions. In the context of the resolution of Problem (3.12), we end up with Algorithm 1, where the differentiable cost function is dealt with a gradient step while a projection step is used to handle the constraint terms ($J_{\max} > 0$ denotes the maximum iteration number). To benefit from the splitting ability of this primal-dual approach, we have defined the following functions:

$$\begin{cases} f = & \iota_{[0,+\infty[^m}, \\ g = & \iota_{B_{1,2}(0,\eta)}, \\ h = & \frac{1}{2}\|p - A\cdot\|^2, \end{cases} \tag{3.14}$$

where f is the positivity constraint function, g represents the TV constraint function, and h is the data fidelity function. Hereabove, we have introduced the indicator function of a subset C of a Hilbert space $\mathcal{H}$ which is defined as follows:

$$\forall d \in \mathcal{H}, \;\; \iota_C(d) = \begin{cases} 0 & \text{if } d \in C, \\ +\infty & \text{otherwise.} \end{cases} \tag{3.15}$$

Algorithm 1: General formulation of Parallel Forward-Backward based Primal-Dual Algorithm for Problem (3.12)

Set $\lambda \in]0,1]$, $\tau \in]0,+\infty[$.
Compute σ using (3.19).
Set primal and dual variables: $d^{(0)} \in \mathbb{R}^m$, $y^{(0)} \in \mathbb{R}^{3m}$
for $j = 1, \ldots, J_{\max}$ **do**
  $\tilde{d}^{(j)} = \text{prox}_{\tau f}(d^{(j)} - \tau(\nabla h(d^{(j)}) + \Delta^\top y^{(j)}))$
  $d^{(j+1)} = d^{(j)} + \lambda(\tilde{d}^{(j)} - d^{(j)})$
  $\tilde{y}^{(j)} = \text{prox}_{\sigma g^*}(y^{(j)} + \sigma\Delta(2\tilde{d}^{(j)} - d^{(j)}))$
  $y^{(j+1)} = y^{(j)} + \lambda(\tilde{y}^{(j)} - y^{(j)})$
end

In order to implement our algorithm, we need to apply the proximity operators of f and g functions (here equivalent to projecting over the constraint sets), while we perform a gradient step for h function.
We recall that the proximity operator [78] of a proper, convex, lower semi-continuous function $f\colon \mathbb{R}^m \to]-\infty, +\infty]$ is defined as follows

$$\forall x \in \mathbb{R}^m, \quad \text{prox}_f(x) = \underset{u \in \mathbb{R}^m}{\text{argmin}} \quad f(u) + \frac{1}{2}\|u - x\|^2. \tag{3.16}$$

Hereunder, we deduce the projection onto the closed convex domain $[0, +\infty[^m$ as the proximity operator of function f. We note also that, in practice, we can use Moreau's decomposition formula to express $\text{prox}_{\sigma g^*}$ from $\text{prox}_{\sigma g}$:

$$\begin{aligned} \forall u \in \mathbb{R}^{3m}, \quad \text{prox}_{\sigma g^*}(u) &= u - \text{prox}_{\sigma^{-1} g}(\sigma^{-1} u) \\ &= u - \text{P}_{B_{1,2}(0,\eta)}(\sigma^{-1} u), \end{aligned} \tag{3.17}$$

where P_C denotes the projection onto a nonempty closed convex set C. The algorithm parameter (σ, τ) are chosen so as to satisfy the theoretical requirements in [78] in order to guarantee the convergence of Algorithm 1:

$$\tau^{-1} - \sigma\|\Delta\|_S^2 \geq \frac{1}{2\|A\|_S^2} \tag{3.18}$$

where $\|A\|_S$ (resp. $\|\Delta\|_S$) denotes the spectral norm of A (resp. Δ). To set the algorithm parameters in practice, we simply fix $\tau \in]0, 2\|A\|_S^2[$ and compute σ as follows:

$$\sigma = \frac{1}{\|\Delta\|_S^2} \left(\tau^{-1} - \frac{1}{2\|A\|_S^2} \right). \tag{3.19}$$

Based on (3.17), we re-write Algorithm 1 in the following way:

Algorithm 2: General formulation of Parallel Forward-Backward based Primal-Dual Algorithm for Problem (3.12)

Set $\lambda \in]0, 1]$, $\tau \in]0, +\infty[$.
Compute σ using (3.19).
Set primal and dual variables: $d^{(0)} \in \mathbb{R}^m$, $y^{(0)} \in \mathbb{R}^{3m}$
for $j = 1, \ldots, J_{\max}$ **do**
  $\tilde{d}^{(j)} = \mathrm{P}_{[0,+\infty[^m}(d^{(j)} - \tau(A^\top(Ad^{(j)} - p) + \Delta^\top y^{(j)}))$
  $d^{(j+1)} = d^{(j)} + \lambda(\tilde{d}^{(j)} - d^{(j)})$
  $\tilde{y}^{(j)} = y^{(j)} + \sigma\Delta(2\tilde{d}^{(j)} - d^{(j)})$
    $-\sigma\, \mathrm{P}_{B_{1,2}(0,\zeta)}(\sigma^{-1} y^{(j)} + \Delta(2\tilde{d}^{(j)} - d^{(j)}))$
  $y^{(j+1)} = y^{(j)} + \lambda(\tilde{y}^{(j)} - y^{(j)})$
end

Let consider d^* the resulting regularized TV-based solution obtained by Algorithm 2.

We apply on the latter one morphological operations [101] in order to detect the voxels containing structures suspected to be microcalcifications whose size lies in a specific range, in the line of the method from [136]. As we are interested in preserving small particles with no specific spatial orientation, we use an opening operator using a disk with a small radius as the structuring element that we apply slice per slice. In order to keep structures with radius size in the range $[\rho_{\min}, \rho_{\max}]$ where $0 < \rho_{\min} < \rho_{\max}$, we apply the following steps:

1. Apply opening with radius $\rho_{\min}$ on d^* to generate $d^*_{|\rho_{\min}}$.

2. Apply an opening with radius $\rho_{\max}$ on $d^*_{|\rho_{\min}}$ to generate $d^*_{|\rho_{\max}}$.

3. $\mu = d^*_{|\rho_{\min}} - d^*_{|\rho_{\max}}$.

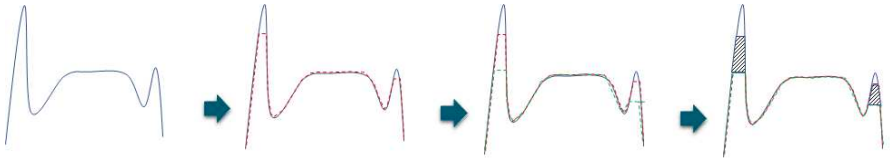

(a) **(b)** **(c)** **(d)**

Figure 3.5: *Different steps performed to detect the signal of interest: (a) Original signal. (b) Applying opening with radius $\rho_{\min}$ on original signal results in red signal. (c) Applying opening with radius $\rho_{\max}$ on output signal of step (b) results in green signal. (d) The signal of interest is the hatched part obtained by the subtracting green signal to red one.*

The output of the above method leads to our estimated μ which is expected to contain high intensity voxels in zones where structures are present in the predefined radius range, and very low intensity ones otherwise.

The estimated signal μ will also be useful for the construction of the ROIs themselves, as the local maxima of μ correspond to sought areas for micro-calcifications. We propose to extract local maxima from a MaxTree [16] representation computed using 26-connectivity. This approach allows to represent the volume as a tree where each node corresponds to a connected component of similar gray level. The nodes are then connected hierarchically depending on their intensity. By construction, the leaves present the highest gray level intensities, that are the local maxima. Determining the set of pixels included in each leaf allows us to construct a list of q representative pixels that we define to be the centers of our ROIs. We then deduce the $(\mathbb{I}^i)_{1\leq i\leq q}$ sets by imposing a given ROI size enabling the inversion of the covariance matrix while minimizing the overlap of ROIs.

3.3.3 Proposed reconstruction algorithm

In this section we will explain the method allowing us to reconstruct the volume d. Henceforth, we reformulate Problem (2.11) as the minimization of a penalized least squares cost function

$$(\forall d \in \mathbb{R}^m) \quad f(d) = \frac{1}{2}\|p - Ad\|^2 + \Phi(d) - \alpha D(d) + \frac{\gamma}{2}\|d\|^2 + \kappa Q(d) \tag{3.20}$$

where

$$(\forall d \in \mathbb{R}^m) \quad \Phi(d) = \Psi(\Delta d), \tag{3.21}$$

with

$$\big(\forall u = (u_i)_{1\leq i\leq m} \in (\mathbb{R}^3)^m\big) \quad \Psi(u) = \sum_{i=1}^{m} \psi\big(u_i\big), \tag{3.22}$$

In this work, we will set

$$(\forall u \in \mathbb{R}^3) \quad \psi(u) = \beta\sqrt{\|u\|^2 + \epsilon^2}, \tag{3.23}$$

where $\beta > 0$ is the regularization weight, and $\epsilon > 0$ controls the smoothness of the penalty function. Moreover, $D\colon \mathbb{R}^m \to \mathbb{R}$ denotes the developed detectability function with weight $\alpha > 0$ that controls the sensitivity of detection for the microcalcifications in the reconstructed DBT volume. The elastic net regularization $\|.\|^2$ with weight $\gamma \geq 0$ is included to ensure the uniqueness of the solution. Finally, the values of the reconstructed volume are encouraged to lie in a specific range of values $[0, d_{\max}]$, with $d_{\max} > 0$, through the introduction of the penalty function Q scaled with $\kappa > 0$, that reads

$$(\forall d = (d_i)_{1\leq i\leq m} \in \mathbb{R}^m) \quad Q(d) = \sum_{i=1}^{m} \inf_{a\in[0,d_{\max}]} (d_i - a)^2. \tag{3.24}$$

It is worth mentioning that, when κ goes to infinity, κQ tends to the indicator function for the convex domain $[0, d_{\max}]^m$. To compute the function D, we shall follow these steps:

- We compute d^* by solving a total variation based constrained problem, then we estimate the corresponding μ following the method detailed in Section 3.3.2
- We extract the related ROIs using the method presented in Section 3.3.2
- We compute the inverse of the covariance matrix Σ and we choose the channelization matrix U as will be explained in the next section.

The minimization of f is performed by using a new formulation of Majorize-Minimize Memory Gradient (3MG) algorithm [35] that will be further detailed in Section 5.2.

§ 3.4 Assessment of microcalcification enhancement in different datasets

3.4.1 Experimental settings

We now present experimental results assessing the performance of our method on both physical phantom and several clinical datasets, that will be further detailed in sections 3.4.2 and 3.4.3. For each considered volume, we simulated the 9 projections as acquired with a DBT commercial system (Senographe Essential, GE Healthcare) with a 25° opening angle. The detector is composed of 3062 × 2394 detector elements of 100 µm×100 µm in

size. The volumes are reconstructed with a 100 µm×100 µm×1 mm sampling grid. We aim at enhancing the detectability of microcalcifications with size ranging from 0.2 mm to 0.4 mm. This range was chosen to enhance the visibility of a specific group of microcalcifications included in Model 015 phantom (CIRS, Norfolk, VA, USA) and clinical data used in our experiments. A detection map is generated as explained in Section 3.3.2, with the same sampling grid as the reconstructed volume. The size of the ROIs was set to $51 \times 51 \times 5$ voxels so that it ensures the inversion of the covariance matrix Σ defined in (3.7) while reducing the overlapping between ROIs. The total number q of ROIs depends on the considered data. In our experiments, q varies from 10^5 to 10^6 for the volumes considered in the evaluation of our approach that will be further described in Sections 3.4.2 and 3.4.3. The covariance matrix Σ is learnt from a database of 400 ROIs. Half of the ROIs contain lesions of 0.2 mm in size, while the others do not contain any. The images we used were generated by using a simulation software developed by GE Healthcare [84]. Finally, Laguerre-Gauss channels [108] are employed for defining the matrix $U \in \mathbb{R}^{k\times c}$ defined below :

$$U = \begin{bmatrix} u_1 & u_2 & \dots & u_c \end{bmatrix} \tag{3.25}$$

where, for every $p \in \{1, \dots, c\}$, $u_p = (u_{\ell,p})_{1\leq \ell \leq k}$ represents a $k-$dimensional Laguerre-Gauss channel which is defined as

$$\forall\ \ell \in \{1, \dots, k\}, \quad u_{\ell,p} = \frac{\sqrt{2}}{a_u} \exp\left(\frac{-\pi \|z_\ell\|^2}{a_u^2}\right) L_{p-1}\left(\frac{2\pi \|z_\ell\|^2}{a_u^2}\right), \tag{3.26}$$

where, for every $\ell \in \{1, \dots, k\}$, z_ℓ denotes the 3D spatial coordinates of the ℓ-th voxel of the ROI (with spatial origin defined at the center of it), $a_u \in \mathbb{R}_+$ represents the spread of the Gaussian kernel and L_{p-1} denotes the Laguerre polynomial of degree $p-1$, defined as

$$\forall x \in \mathbb{R}, \quad L_{p-1}(x) = \sum_{j=0}^{p-1} (-1)^j \binom{p-1}{j} \frac{x^j}{j!}. \tag{3.27}$$

A range of values for a_u and c were considered depending on the background type. We select then the optimal combination that maximizes the area under ROC curve following the CHO framework [112]. Based on a previous research work [84], the values of a_u and c are presented in Table 3.1 for 0.2 mm spherical microcalcifications.

Table 3.1: *Laguerre-Gauss channels parameters used for different background types.*

Background type	Laguerre-Gauss parameters
Uniform	$a_u = 0.8, \quad c = 30$
Textured	$a_u = 0.6, \quad c = 30$

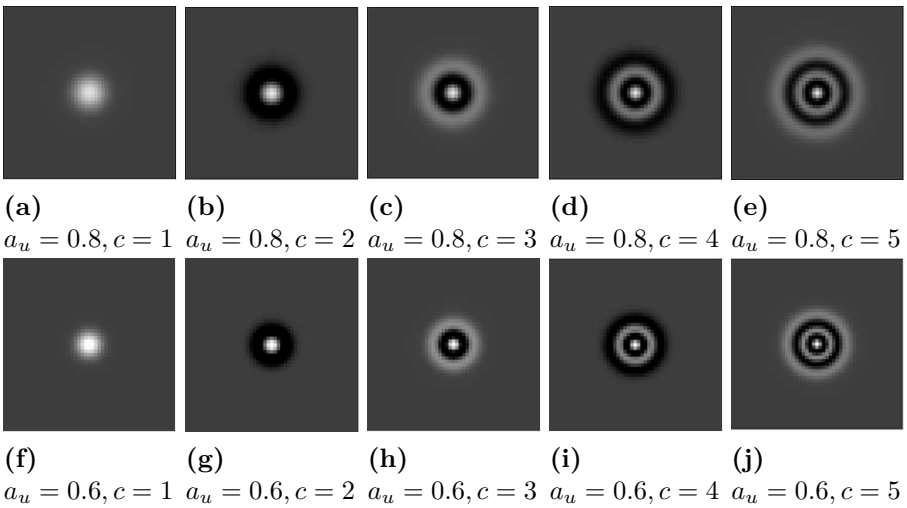

Figure 3.6: *Example of the central slice of three-dimensional Laguerre-Gauss channels with size* $51 \times 51 \times 5$ *used for uniform background (first row) and textured background (second row).*

Table 3.2: *The parameters value of the smooth TV regularization used in* (3.21) *and TV constraint function used in* (3.12)*, respectively.*

TV version	Regularization parameters
Smoothed TV version	$\beta = 600, \quad \epsilon = 10$
Constrained TV version	$\eta = \frac{3}{2}\|\Delta d_0\|_{1,2}$

Our minimization algorithm (See Chapter 5) used to solve the optimization problem (3.20) is initialized with the Filtered Back Projection (FBP) solution, and run until a maximum number of iterations (here equal to 200), which was shown to be sufficient to reach practical convergence in our experiments. The upper bound in the range of plausible values of the reconstructed volume is chosen equal to $d_{max} = 4095$. The smooth TV regularization parameters β and ϵ in equation (3.21) and bound η associated with the TV constraint in (3.12) are adjusted based on visual inspection, so as to optimize the global reconstruction quality. In Table 3.2, the latter

parameters value are provided where d_0 is taken as the FBP solution.

3.4.2 Physical phantom data

We have first used data acquired from the Model 015 phantom (Figure 3.7). Its dimension is of 45mm × 102mm × 108mm, with uniform background. Fibers, specks and masses are embedded in a wax insert to simulate respectively microcalcifications, fibrous structures and tumors. The phantom simulates a 4.2cm compressed breast of average glandular/adipose composition. In our experiments, we were focused on the group of 6 Al_2O_3 specks simulating microcalcifications of 0.32mm in diameter.

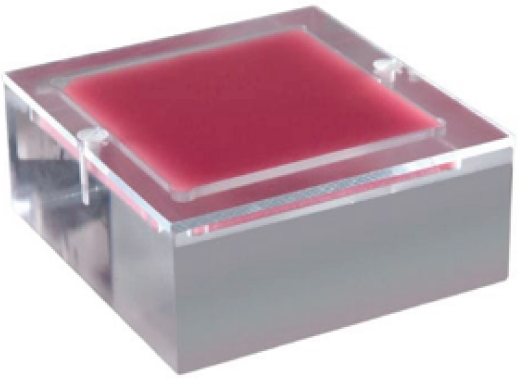

(a)

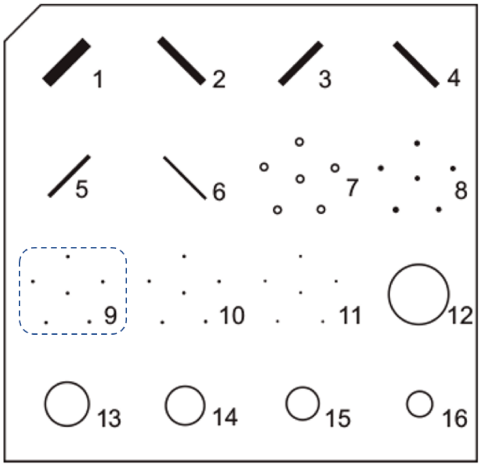

(b)

Figure 3.7: *Model* 015 *phantom (CIRS, Norfolk, VA, USA) : (a) Physical phantom. (b) The test objects are located in the red wax insert. The dotted region represents* 6 Al_2O_3 *specks that simulates microcalcifications of* 0.32 mm *in diameter.*

We first show in Figure 3.8 the central slice of the resulting signal estimation μ (detection map) of the zoomed region, following the method detailed in Section 3.3.2. We note that the background is merely equal to 0 and that the 6 microcalcifications are well detected. Yet, it is important to mention that different gray level values will lead to different enhancement levels for each detected microcalcification. This may be explained by ; the variability in size of the small specks in Model 015 phantom and the noise generated while acquiring the projections.

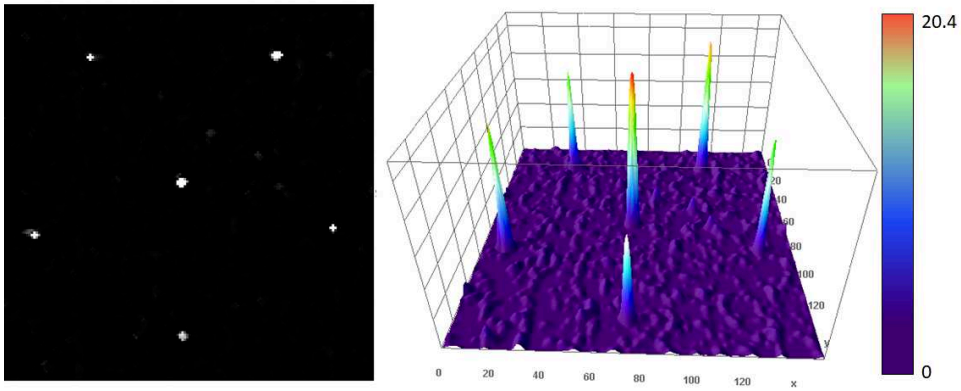

Figure 3.8: *Zoomed slice of μ, estimated from Model 015 phantom, containing 6 ROIs .*

Effect of varying α weight:
Now, we illustrate in Figure 3.9 the influence of a change in the parameter α weighting the detectability function in equation (3.20). We observe that the higher the value of α, the more visible the microcalcifications. Qualitatively, this is illustrated in Figure 3.9(a) to (d) according to the increased value of α. This latter parameter is expected to control the sensitivity of detection for the microcalcifications in the reconstructed DBT volume. Quantitatively, this is depicted through the increased SDNR value denoted in Table 3.3 when increasing the magnitude of the detectability function. Note that the signal difference to noise ratio (SDNR) is computed as following:

$$SDNR = \frac{\max_{signal} - m_{bg}}{\sigma}. \tag{3.28}$$

where $\max_{signal}$ is the maximum value of the signal of interest, m_{bg} denotes the mean value of the background and σ represents the standard deviation of the background. Consequently, this measure helps us to quantify the contrast of the enhanced microcalcifications. We highlight also that despite the high number of ROIs (around 10^5) within the whole volume, the enhancement is only effective in the microcalcifications area. No false positives appear to have been caused by our approach on this uniform background

image of Model 015 phantom. This is outlined numerically in Table 3.3 where we notice that for the different values of α, the reconstructed region of Model 015 phantom demonstrates the same mean brightness level. Furthermore, the pixel values deviate approximately with the same magnitude around the same grayscale mean.

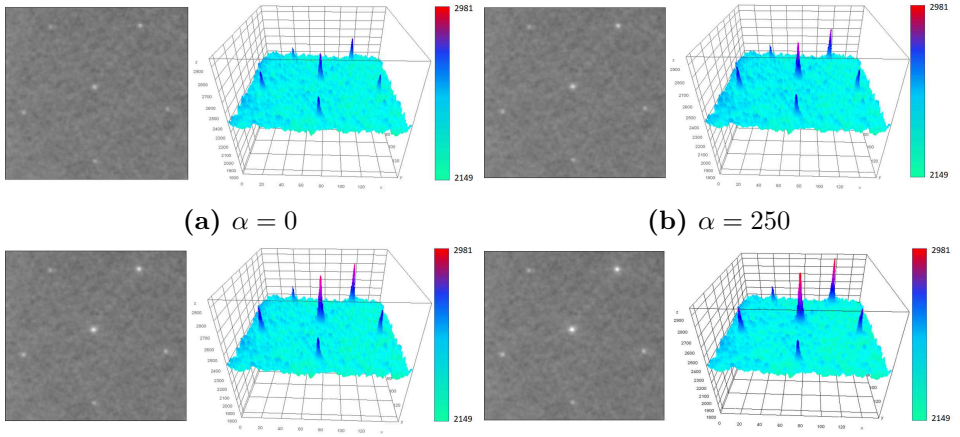

(a) $\alpha = 0$ **(b)** $\alpha = 250$

(c) $\alpha = 500$ **(d)** $\alpha = 750$

Figure 3.9: *Region of Model 015 phantom slice containing 6 ROIs: Enhancement level for different detectability function weights* α.

Table 3.3: *Statistics on the region of Model 015 phantom slice containing 6 ROIs for different* α *values*

α	Mean	StD	Max	SDNR
0	2340.93	22.90	2667	11
250	2343.55	22.91	2774	13
500	2337.70	22.94	2873	15
750	2336.85	22.99	2981	18

Increased SDNR values highlight that the enhancement is indeed effective on the 6 microcalcifications comprised in the zoomed region of the Model 015 phantom. This is further confirmed qualitatively and quantitatively in Figure 3.10 and Table 3.4 when analyzing SDNR of individual microcalcifications. It is worth mentioning that high values of α may however tend to increase the size of the enhanced microcalcifications. In this context, microcalcifications 2 and 3 in Figure 3.10 are the most affected by this spreading effect. To further understand this effect, we suggest studying the contribution of each regularization term used in the proposed cost function (3.20) that is minimized to reconstruct the DBT volume.

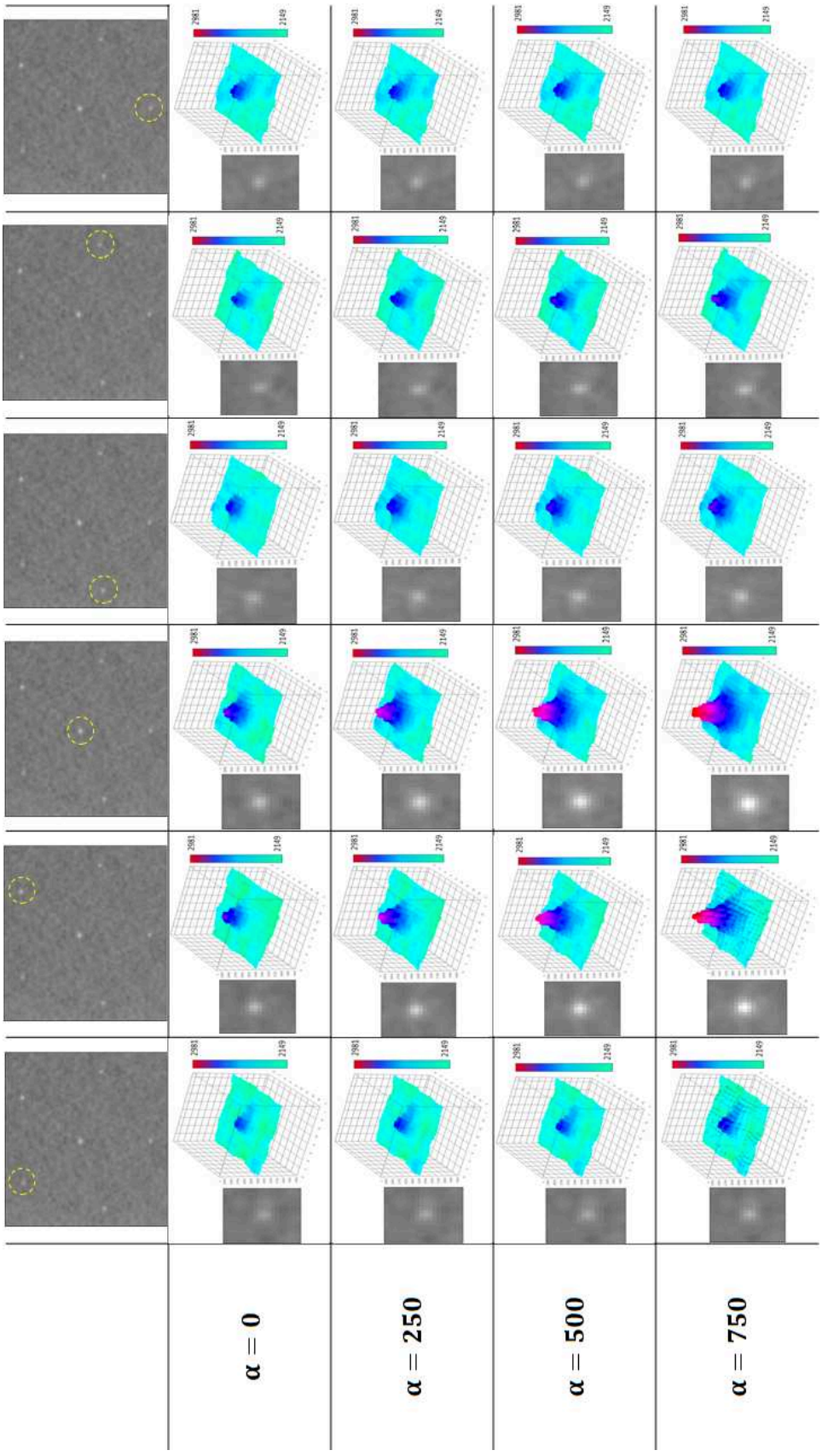

Figure 3.10: *Profiles of each microcalcification in the considered region of the Model 015 phantom slice for different α values*

Table 3.4: *SDNR (signal difference to noise ratio) of each microcalcification in the considered region of Model 015 phantom slice for different α values*

α	0	250	500	750
Microcal. 1	8	9	10	11
Microcal. 2	13	17	22	27
Microcal. 3	14	19	23	28
Microcal. 4	10	11	13	14
Microcal. 5	9	11	12	14
Microcal. 6	10	10	11	11

Effect of each term in the penalized least squares function :
In this section, we investigate the effect of each regularization term in the considered cost function (3.20). We are particularly interested to scrutinize the interaction between the smoothed TV regularization function Φ defined in (3.21) and the newly developed detectability function D in (3.11). For this reason, we consider four different reconstructions as illustrated in Figure 3.11:

- non-regularized least squares solution (NRLS)
- classical TV and no detectability function (TV)
- non-regularized least squares solution with detectability function (dNRLS)
- classical TV using detectability function (dTV)

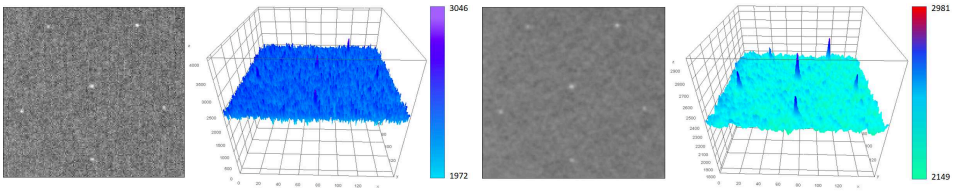

(a) $\alpha = 0, \beta = 0$ **(b)** $\alpha = 0, \beta = 600$

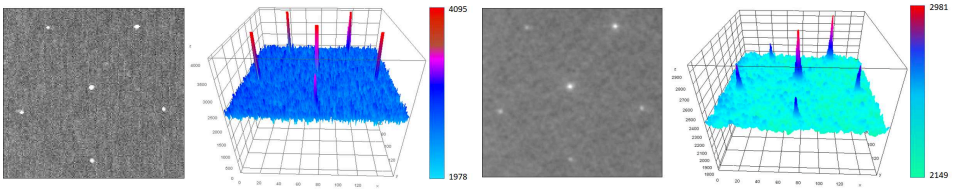

(c) $\alpha = 750, \beta = 0$ **(d)** $\alpha = 750, \beta = 600$

Figure 3.11: *Region of Model 015 phantom slice containing 6 ROIs : (a) NRLS. (b) TV. (c) dNRLS. (d) dTV.*

As expected, the non-regularized least squares solution (NRLS) leads to a highly noise level as shown in Figure 3.11(a). DBT reconstruction with classical TV and no detectability function (TV) leads to a satisfying background restoration however it reduces microcalcification intensity and sharpness, as depicted in Figure 3.11(b). In contrast, Figure 3.11(c) demonstrates that when the detectability function is used, without additional regularization (dNRLS), the microcalcifications are enhanced as well as sharpened. Yet, the background remains noisy. Finally, by combining the detectability function and the classic TV regularization (dTV), in Figure 3.11(d), we simultaneously denoise the background and enhance the contrast of microcalcifications. However, the latter appear less sharp and with a slight spreading effect increasing their perceived size.

Table 3.5: *Statistics on the region of Model 015 phantom slice containing 6 ROIs for different reconstructions*

Algorithm	$\boldsymbol{\alpha, \beta}$	**Mean**	**StD**	**Max**	**SDNR**
NRLS	$\alpha = 0, \beta = 0$	2348.76	96.20	3046	7
TV	$\alpha = 0, \beta = 600$	2339.97	34.36	2667	10
dNRLS	$\alpha = 750, \beta = 0$	2343.71	114.52	4095	15
dTV	$\alpha = 750, \beta = 600$	2339.60	37.92	2981	17

The aforementioned qualitative observations are numerically outlined through the statistical values provided in Table 3.5. In fact, noise level in the least squares solution (NRLS) as well as in the DBT reconstruction with detectability function and no regularization (dNRLS) is explained by the relatively high deviation magnitude of pixels around the grayscale mean. In contrast, the regularized solutions, i.e when $\beta = 600$, (TV) and (dTV), provide a lower deviation magnitude around the grayscale mean. Furthermore, DBT reconstruction when using detectability function and no TV regularization (dNRLS), i.e. $\alpha = 750$ and $\beta = 0$, provides the highest maximum grayscale value reflecting the highest enhancement level in the detected microcalcifications. This latter maximum value decreases when TV regularizer is incorporated in the DBT reconstruction, with a lower noise level leading to a better SDNR.

To better grasp the aforementioned observations, we focus on the central microcalcification where the spreading effect is the most obvious. Therein, we observe in Figure 3.12(a) that the least squares solution (NRLS) yields to a poorly defined microcalcification due to the high presence of the noise. DBT reconstruction when using TV regularization (TV), in Figure 3.12(b) provides a better restoration of the background where the microcalcification can be better distinguished. However, the microcalcification appears to be smoother and less enhanced. In contrast, DBT reconstruction with

detectability function and no TV regularization (dNRLS) leads to enhanced and sharper microcalcification that stands out in a highly noisy background, as depicted in Figure 3.12(c). Finally, a DBT reconstruction with detectability function and TV regularization (dTV), as shown in Figure 3.12(d), simultaneously leads to a high restoration of the background and a significant enhancement of the microcalcification contrast. Nonetheless, the microcalcification seems less sharp compared to DBT reconstruction with detectability function and no TV regularization (dNRLS). Herein, further investigation for a more sophisticated spatial regularizer is needed to preserve the sharpness of the enhanced microcalcifications.

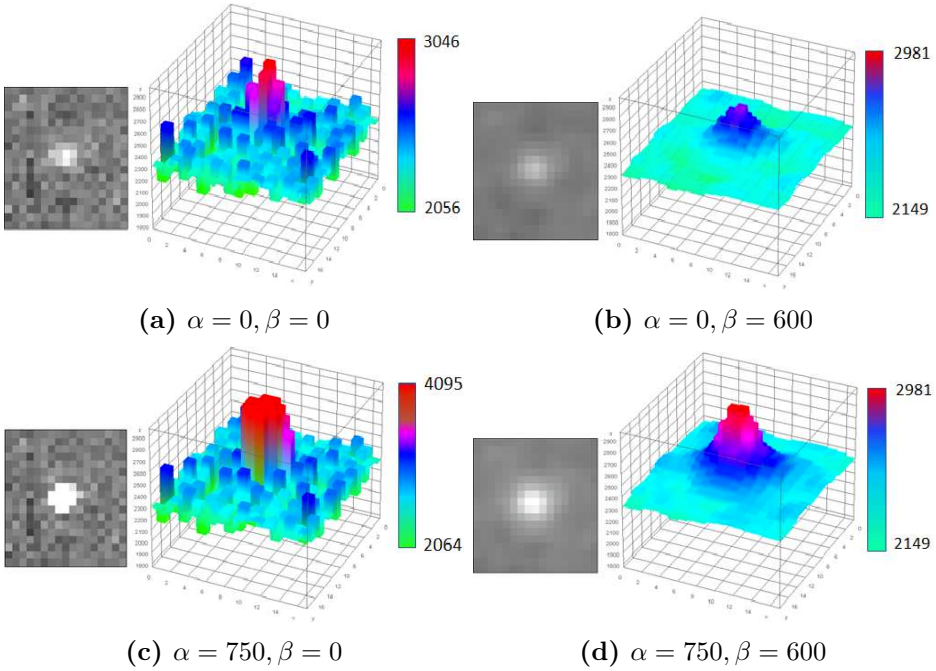

(a) $\alpha = 0, \beta = 0$ **(b)** $\alpha = 0, \beta = 600$

(c) $\alpha = 750, \beta = 0$ **(d)** $\alpha = 750, \beta = 600$

Figure 3.12: *Zoom on the central microcalcification contained in the considered region of Model 015 phantom central slice : (a) NRLS. (b) TV. (c) dNRLS. (d) dTV.*

3.4.3 Clinical data

We also assessed our approach on clinical data. We propose to show representative cases that include inconspicuous microcalcifications. First, we evaluate our approach on cases containing benign microcalcifications. Then, we extend our evaluation on a case comprising a potentially malignant group of microcalcifications.

Clinical cases with benign microcalcifications: We present in Figure 3.13 results for a BI-RADS d breast composition image containing an isolated microcalcification and in Figure 3.14 and 3.15, for a BI-RADS c breast composition image comprising group of microcalcifications. The corresponding detection maps are shown in Figure 3.13(a), Figure 3.14(a) and Figure 3.15(a) respectively. Similar conclusions as for the physical phantom case can be drawn from visual inspection of those images. We notice again two drawbacks of DBT reconstruction with detectability function and no TV regularization. First, it may yield saturated microcalcifications since no penalization is applied in their gray level values (Figure 3.13(c)). Second, some false positives in the detection map may also lead to enhanced microcalcification-like structures when no regularization is applied (Figure 3.13(c), Figure 3.14(c) and Figure 3.15(c)). By combining the detectability function and TV regularization (Figure 3.13(e), Figure 3.14(e) and Figure 3.15(e)), we observe similar results as for the physical phantom case, enhanced but unsharp microcalcifications and a denoised background.

Clinical case with potentially malignant cluster of microcalcifications: We show in Figure 3.16 results for a BI-RADS c breast composition image with a potentially malignant group of microcalcifications. The corresponding detection map is illustrated in Figure 3.16(a). Here again, we observe the behaviour already unveiled in the physical phantom data as well as the aforementioned clinical cases. In one hand, the advantage of applying the detectability function in the DBT reconstruction is the significant enhancement in the detected microcalcifications, as illustrated when comparing Figure 3.16(b) with Figure 3.16(c). In the other hand, the TV regularizer improves the robustness to the noise and the overall image quality, as illustrated when comparing Figure 3.16(b) with Figure 3.16(d). Henceforth, applying these two terms enables simultaneously the enhancement of microcalcifications and the high restoration of the background, as illustrated in Figure 3.16(e). However, the observed unsharpness of microcalcifications incites us to investigate the efficiency of TV regularizer in our reconstruction problem.

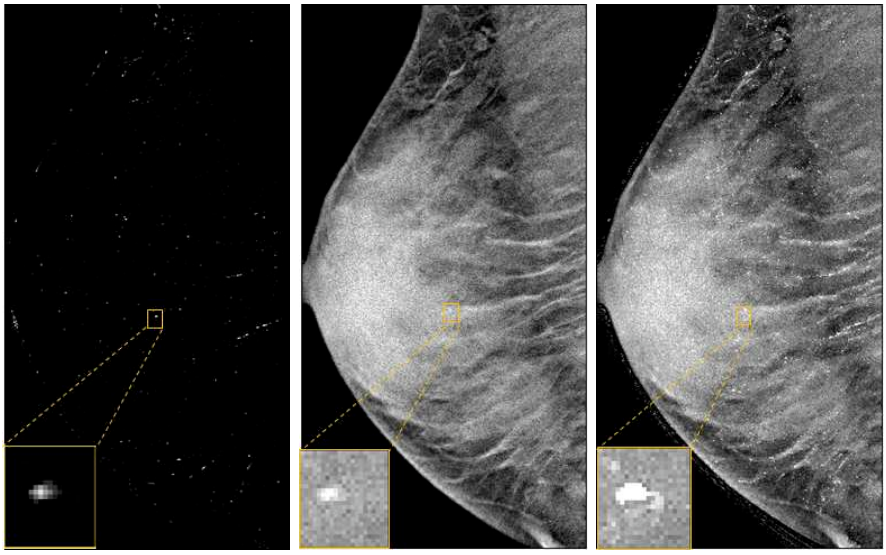

(a) **(b)** $\alpha = 0, \beta = 0$ **(c)** $\alpha = 0, \beta = 600$

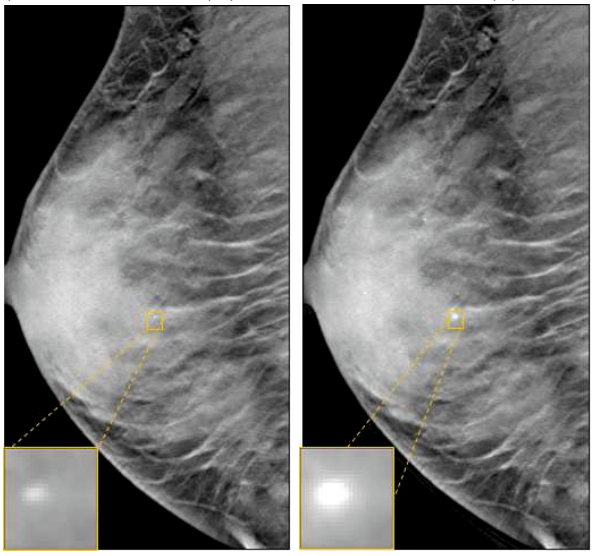

(d) $\alpha = 1500, \beta = 0$ **(e)** $\alpha = 1500, \beta = 600$

Figure 3.13: *Selected slice of a DBT reconstruction with size* $2344 \times 868 \times 44$ *(voxels) : (a) Detection map* μ*. (b) NRLS. (c) dNRLS. (d) TV. (e) dTV.*

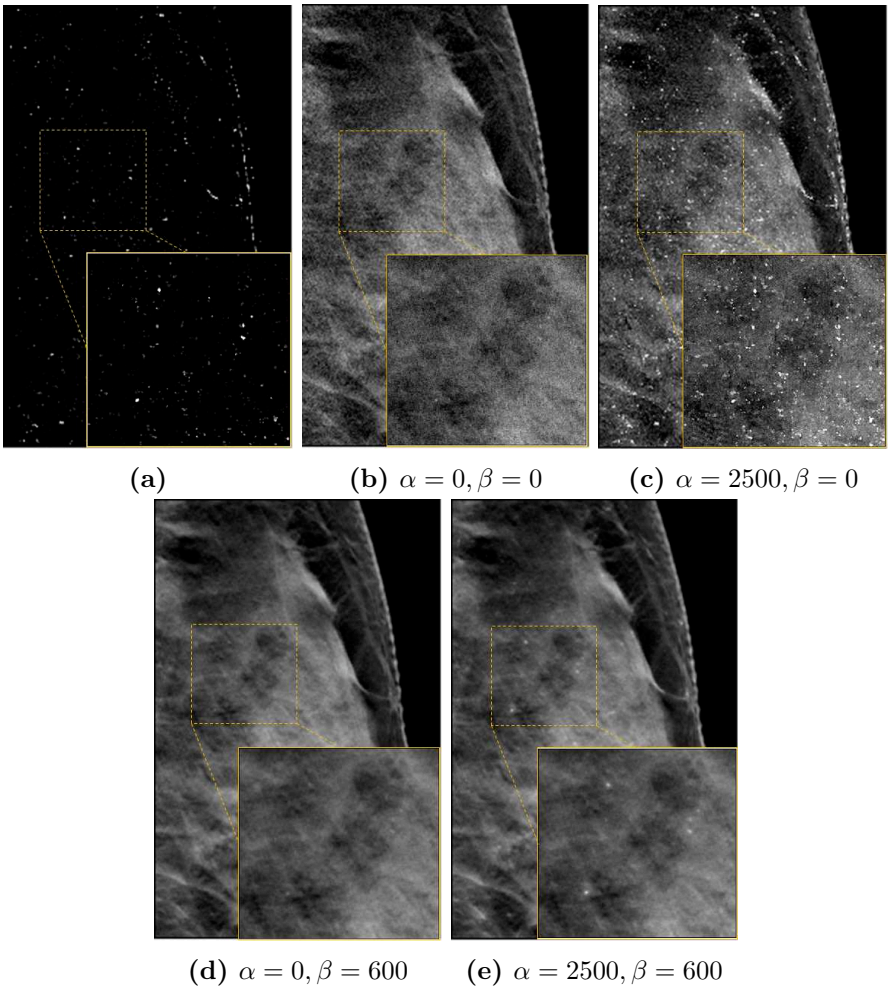

(a) **(b)** $\alpha = 0, \beta = 0$ **(c)** $\alpha = 2500, \beta = 0$

(d) $\alpha = 0, \beta = 600$ **(e)** $\alpha = 2500, \beta = 600$

Figure 3.14: *Selected slice of a DBT reconstruction with size* $2227 \times 594 \times 44$ *(voxels) : (a) Detection map* μ*. (b) NRLS. (c) dNRLS. (d) TV. (e) dTV.*

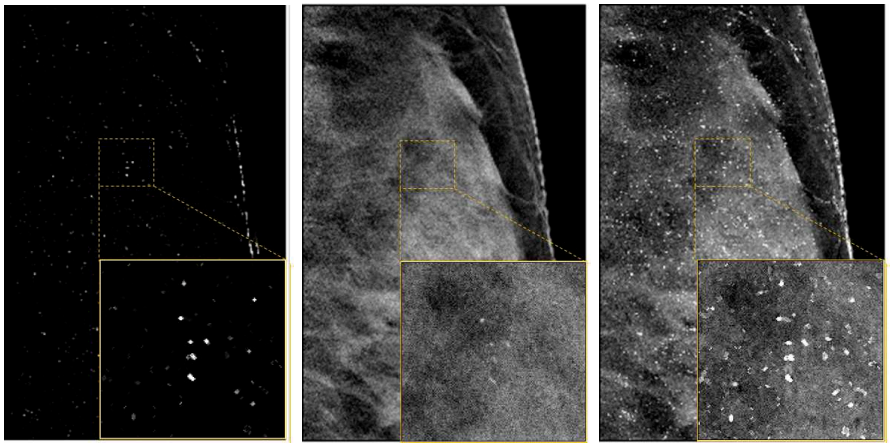

(a) **(b)** $\alpha = 0, \beta = 0$ **(c)** $\alpha = 2500, \beta = 0$

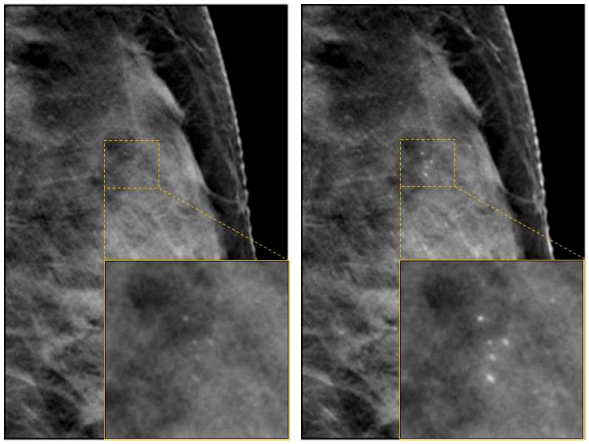

(d) $\alpha = 0, \beta = 600$ **(e)** $\alpha = 2500, \beta = 600$

Figure 3.15: *Selected slice of a DBT reconstruction with size* $2227 \times 594 \times 44$ *(voxels) : (a) Detection map* μ*. (b) NRLS. (c) dNRLS. (d) TV. (e) dTV.*

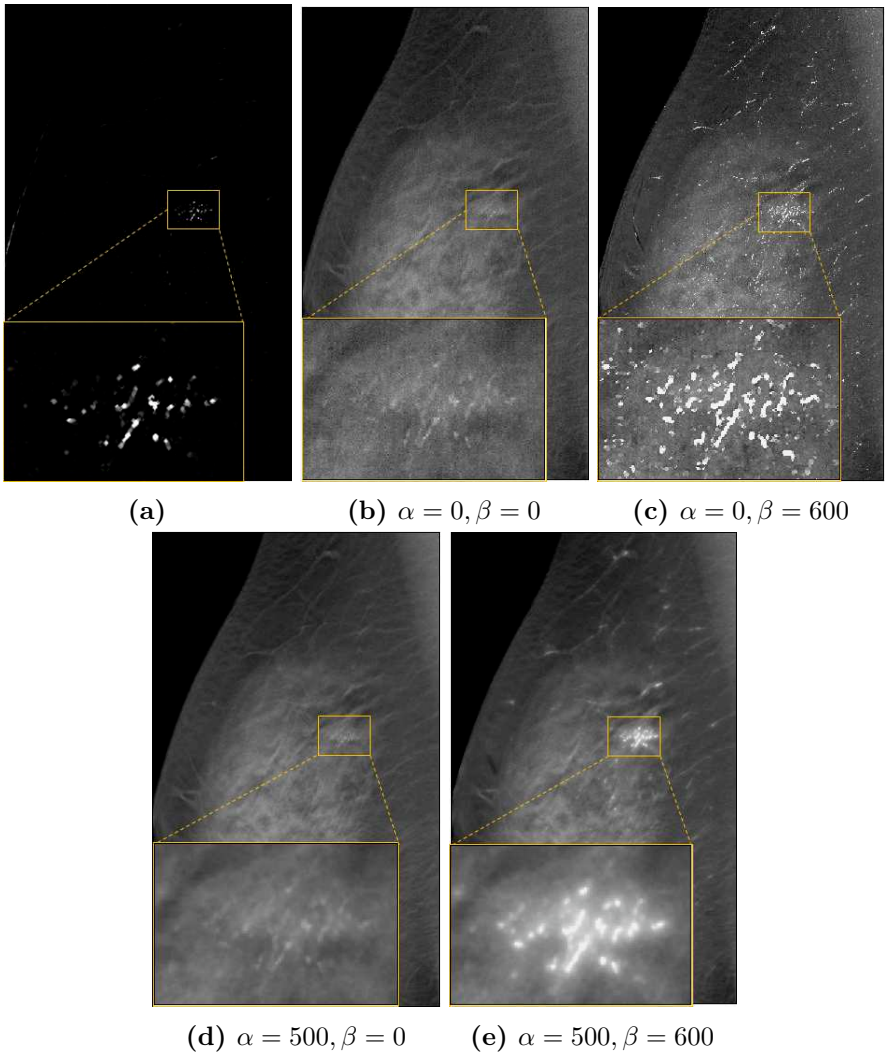

(a) **(b)** $\alpha = 0, \beta = 0$ **(c)** $\alpha = 0, \beta = 600$

(d) $\alpha = 500, \beta = 0$ **(e)** $\alpha = 500, \beta = 600$

Figure 3.16: *Selected slice of a DBT reconstruction with size* $3062 \times 994 \times 67$ *(voxels) : (a) Detection map* μ*. (b) NRLS. (c) dNRLS. (d) TV. (e) dTV.*

§ 3.5 Summary

In this chapter, we introduced a new a priori term in the DBT reconstruction process by adding to a classical regularized iterative DBT reconstruction a task-based assessment strategy implemented in the CHO observer. Henceforth, we have proposed a new approach aiming at enhancing the detectability of microcalcifications in DBT reconstruction as the targeted clinical task. We defined a detectability function, which is computed following an approach similar to the mathematical model observer CHO and we incorporated it as an a priori term in the proposed optimization approach.

We demonstrated on both synthetic and clinical datasets the potential interest of our method with respect to standard DBT reconstruction in terms of microcalcification visibility.

Although we are able to enhance the visibility of microcalcifications, they might appear less sharp and with a slight spreading effect. This particularly holds when combining the detectability function and the TV regularizer. In the next chapter, we propose to spatially adapt the regularization aiming at improving the robustness to the noise, the overall image quality and the preservation of microcalcification shape.

- Chapter 4 -

A new Spatially Adaptive TV (SATV) regularization function : Application in DBT

§ 4.1 Introduction

In literature, most DBT reconstructions have used total variation (TV) as a spatial regularization function [122, 124, 94]. The TV regularizer has demonstrated great performance in several applications of image processing [46, 28, 1, 47]. However, the staircasing effect inherent to TV [104] is not desirable as it rarely fits with the natural textures and shapes arising in real images. Several research studies have suggested alternative TV-based penalties, by proposing smooth approximation of it [8, 20, 29, 30], by introducing non-local similarity measures [32], by considering the posterior mean estimate instead of the standard maximum a posteriori one [86], or by investigating anisotropic gradient operators [88, 93, 85, 140, 19]. The aforementioned works gave rise to promising results but may however not be adapted to the restoration of very heterogeneous areas, such as the breast volume imaged in DBT. We thus propose to formulate a new Spatially Adaptive TV (SATV) regularization function which will take into consideration the different morphological contents of the breast. Different regularizers are applied, depending if microcalcifications are expected or not in the considered image zones. To this aim, we introduce a new definition of the gradient field allowing to involve heterogeneous prior knowledge on the structural content of each voxel of the sought volume.

The remainder of this chapter is organized as follows: we introduce in Section 4.2 state-of-the-art TV-based regularization strategies. In Section 4.3, we provide an original formulation for the weighted gradient field that efficiently incorporates prior knowledge on the location of microcalcifications. Then, we derive our spatially adaptive total variation (SATV) regularization and integrate it in the clinical task-based reconstruction approach for DBT.

Finally, we show experimental results carried out on both physical phantom and clinical data and discuss the qualitative results in Section 4.4.

§ 4.2 Problem statement and motivation

Total Variation (TV) is one of the most popular regularization method in image restoration. It has been initially introduced for 2D image denoising and reconstruction problem [116]. When applied to 3D images, it reads:

$$(\forall d \in \mathbb{R}^m) \quad \Phi(d) = \Psi(\Delta d) \tag{4.1}$$

where $\Delta \in \mathbb{R}^{3m \times m}$ is the 3D gradient operator defined as

$$(\Delta)^\top = [\Delta^x \quad \Delta^y \quad \Delta^y]^\top \tag{4.2}$$

with $\Delta^x \in \mathbb{R}^{m \times m}$ (respectively $\Delta^y \in \mathbb{R}^{m \times m}$, $\Delta^z \in \mathbb{R}^{m \times m}$) discrete horizontal (respectively vertical and depth) gradient operators assuming zero-boundaries. Moreover, Ψ is the sparsity promoting function, typically equals to the ℓ_1 norm (in case of anisotropic TV) or $\ell_{1,2}$ norm (in case of isotropic TV). The total variation promotes the sparsity of the image derivatives, which has the advantage of reducing the noise and preserving strong edges. However, it may lead to undesirable piecewise constant images and induce staircase artefacts [104]. With the aim to overcome these limitations, various variants of TV regularization have been proposed which are listed in the following.

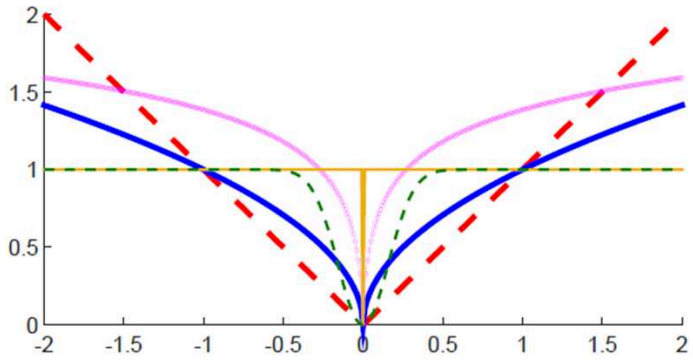

Figure 4.1: *Sparsity promoting norms: ℓ_0 norm (thin solid yellow), ℓ_1 norm (thick dashed red), ℓ_1/ℓ_2 norm (thick solid blue), log-ℓ_1 norm (thin magenta), Welsch penalty (thin dashed green)*

- *Smoothed One Over Two-Total Variation (SOOT-TV)* is a nonconvex sparsity promoting function combining the ℓ_1/ℓ_2 norm and the total

variation operator. ℓ_1/ℓ_2 can be viewed as a more accurate approximation to ℓ_0 compared to the convex ℓ_1 norm, as shown in Figure 4.1. One can mention the log-smoothed version of the ℓ_1/ℓ_2 norm called "SOOT" introduced in [114]. The prior then reads:

$$(\forall d \in \mathbb{R}^m) \quad \Phi(d) = \log\left(\frac{\ell_{1,\alpha}(\Delta d) + \beta}{\ell_{2,\lambda}(\Delta d)}\right), \tag{4.3}$$

where $\ell_{1,\alpha}$ and $\ell_{2,\lambda}$ denote the smooth approximations of ℓ_1 and ℓ_2 respectively, defined as

$$\ell_{1,\alpha}(\Delta d) = \sum_{i=1}^{m}\left(\sqrt{(\Delta d)_i^2 + \alpha^2} - \alpha\right), \quad \ell_{2,\lambda}(\Delta d) = \sqrt{\sum_{i=1}^{m}(\Delta d)_i^2 + \lambda^2}. \tag{4.4}$$

Herein $\Delta \in \mathbb{R}^{3m\times m}$ is the discrete 3D gradient operator defined in equation (4.2) and α, β and λ are positive parameters. It is worth mentioning that for $\alpha = \lambda = 0$ we recover ℓ_1 and ℓ_2.

- *Smoothed log-Total Variation (log-TV)* is a nonconvex smooth sparsity promoting regularization function from [110] defined as follows

$$\begin{aligned}(\forall d \in \mathbb{R}^m) \quad \Phi(d) \quad &= \sum_{i=1}^{m}\log\left(\sqrt{\|(\Delta d)_i\|^2 + \alpha^2}\right) \\ &= \frac{1}{2}\sum_{i=1}^{m}\log\left(\|(\Delta d)_i\|^2 + \alpha^2\right),\end{aligned} \tag{4.5}$$

where $\alpha > 0$ and $\Delta \in \mathbb{R}^{3m\times m}$ the 3D gradient operator as defined in 4.2. Similarly to the ℓ_1/ℓ_2 norm, the log-based penalty used in equation (4.5) can be viewed as a nonconvex approximation to ℓ_0.

- *Welsch-Total Variation (Welsch-TV)* is based on the so-called "Welsch function" [52] defined by

$$\mathbb{R} \to \mathbb{R}: \quad t \to 1 - \exp\left(-t^2/(2\sigma^2)\right). \tag{4.6}$$

The Welsch function is bounded and approaches 1 exponentially fast as $|t| \to +\infty$. It is convex near the origin, for $t^2 < \sigma^2$ and nonconvex elsewhere. When applied to the image gradient with the aim to improve its sparsity, it reads

$$(\forall d \in \mathbb{R}^m) \quad \Phi(d) = \sum_{i=1}^{m}\left(1 - \exp\left(-\|(\Delta d)_i\|^2/(2\sigma^2)\right)\right). \tag{4.7}$$

- *Sophisticated gradient operator :* Furthermore, other TV-based regularizations have been proposed based on more sophisticated definitions of the gradient field of the discrete image. With the aim to curb

the staircasing effect, *Non-local Total Variation (NLTV)* [32] investigates the non-locality through introducing non-local similarity measures, while *Total Generalized Variation (TGV)* [22] involves higher order derivatives of the desired object. Moreover, to better reconstruct oblique structures, *Total Variation on a Staggered Grid (TVSG)* [46] resorts to a more accurate adaptation of the continuous definition to the discrete domain, instead of the classical finite differences in (4.1)-(4.2).

Even though these regularization strategies may show great performance in various image processing applications, none of them have provided a formulation that takes into account the heterogeneity (in shape and texture) within the image to be regularized. In particular, breasts consist of different anatomical components such as tissues (background) (as detailed in Section 2.2.4) and lesions (as depicted in Section 2.2.3), which require a more sophisticated regularization when reconstructing the DBT volume. In such challenging context, our contribution is to propose a new Spatially Adaptive TV (SATV) regularization function which responds to the need for heterogeneous spatial regularization in DBT reconstruction, and accounts for the different morphological contents of the breast. Henceforth, we provide a new definition of the gradient field in the discrete image that takes into consideration an input detection map incorporating prior knowledge on the structural contents of the image. Thus, the SATV operator acts differently according to the sought local information around each voxel.

§ 4.3 SATV REGULARIZATION

4.3.1 Mathematical formulation

Let us consider the detection map $\mu \in \mathbb{R}^m$ obtained as an output of the construction of the previously introduced detectability function (3.11). This map is of a great interest, as it provides a good estimate for the location of the potential microcalcifications in the volume. This allows us to define the following weight parameters,

$$(\forall i \in \{1,\dots,m\}) \quad \lambda_i = \begin{cases} 1 & \text{if } \mu_i \leq \nu - \theta \\ \frac{\theta+\nu-\mu_i}{2\theta} & \text{if } \nu-\theta \leq \mu_i \leq \nu+\theta \\ 0 & \text{otherwise,} \end{cases} \tag{4.8}$$

with $\nu \in [0,+\infty[$ and $\theta \in]0, \min(\nu, 1-\nu)]$. The value of μ_i is high in zones where structures are present, while it is low in other areas. The threshold ν allows to set a binary transition between the breast texture and the detected microcalcifications, while the parameter θ is used to smooth this transition (Figure 4.2).

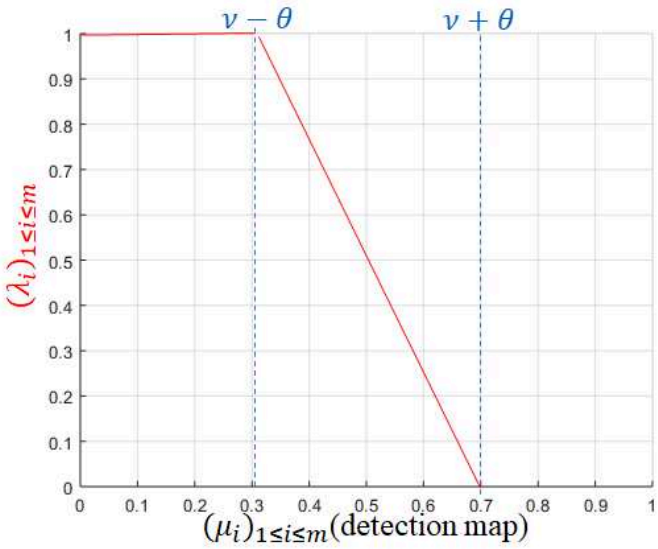

Figure 4.2: *Profile function of weight parameters* $(\lambda_i)_{1\leq i\leq m}$

In essence, they will be set up to preserve the geometric shape of the detected microcalcifications. By construction, $(\lambda_i)_{1\leq i\leq m} \in [0,1]^m$. The latter weight vector allow addressing differently the regularization of the plain healthy tissue and of the critical zones potentially containing microcalcifications.

For this purpose, we formulate our SATV regularization function as follows,

$$(\forall d \in \mathbb{R}^m) \quad \Phi(d) = \sum_{i=1}^{m} \psi\big((1-\eta)\lambda_i \Delta_i d + \eta(1-\lambda_i)\delta d_i\big), \tag{4.9}$$

where $\delta = [1\ 1\ 1]^\top$, $\psi\colon \mathbb{R}^3 \to \mathbb{R}$ represents a sparsity promoting function which applies either on the image intensity or on its gradients, $\eta \in [0,1]$ controls the overall contribution of each regularizing term, and Δ denotes the 3D gradient operator that is expressed as

$$(\Delta_i)^\top = [\Delta_i^x \quad \Delta_i^y \quad \Delta_i^z]^\top \tag{4.10}$$

with Δ_i^x (resp. (Δ_i^y) and (Δ_i^z)) discrete horizontal, (resp. vertical and depth) gradient operators at voxel $i \in \{1,\ldots,m\}$, assuming zero-boundaries. It is worthy to point out the special cases of Φ function, where for every $i \in \{1,\cdots,m\}$:

$$\begin{cases} \text{if} \quad \lambda_i = 0 \quad \text{then } \psi = \|.\|_1 \\ \text{if} \quad \lambda_i = 1 \quad \text{then } \psi = \|.\| \end{cases} \tag{4.11}$$

Henceforth, in the first case of (4.11), Φ corresponds to the ℓ_1 regularization, while the second case of (4.11), reduces Φ to the standard isotropic TV regularizer. For a suitable weight vector $(\lambda_i)_{1\leq i\leq m}$, the norm of the gradient

of the image will be penalized in regions where no microcalcifications are expected, while the intensity of microcalcifications will be penalized in the complementary regions.

4.3.2 Proposed reconstruction algorithm

In this part, we briefly explain how SATV regularization is numerically handled. From equation (4.9), function Φ can be re-expressed as

$$(\forall d \in \mathbb{R}^m)\,, \Phi(d) = \quad \Psi(Ld) \tag{4.12}$$

where

$$\forall u = (u_i)_{1\leq i\leq m} \in (\mathbb{R}^3)^m, \quad \Psi(u) = \sum_{i=1}^{m} \psi\big(u_i\big), \tag{4.13}$$

and

$$L = (1-\eta)(\Lambda \otimes I_3)\Delta + \eta(I_m - \Lambda) \otimes \delta \in \mathbb{R}^{3m\times m}, \tag{4.14}$$

where $\otimes$ denotes the Kronecker product and I_m and I_3 state for the identity matrix dimension $m \times m$ and 3×3 respectively.

$$\Lambda = \quad \mathrm{Diag}(\lambda_1, \ldots, \lambda_m) \tag{4.15}$$

We can easily define the adjoint operator of L in (4.14), L^* that is read

$$L^* = (1-\eta)\Delta^*(\Lambda \otimes I_3) + \eta(I_m - \Lambda) \otimes \delta \in \mathbb{R}^{3m\times m}, \tag{4.16}$$

where Δ^* denotes the adjoint operator of Δ. Based on (4.14), we infer that the norm of L is bounded by the following quantity,

$$\begin{aligned} \|L\| \quad &= \|(1-\eta)(\Lambda \otimes I_3)\Delta + \eta(I_m - \Lambda) \otimes \delta\| \\ &\leq (1-\eta)\|(\Lambda \otimes I_3)\Delta\| + \eta\|(I_m - \Lambda) \otimes \delta\| \\ &\leq (1-\eta)\|\Delta\| + \eta\|\delta\| \\ &\leq (1-\eta)\|\Delta\| + \sqrt{3}\eta \end{aligned} \tag{4.17}$$

Different strategies can be adopted for the choice of the sparsity promoting function ψ, which will have an impact on the reconstruction algorithm used to solve an optimization problem when using SATV regularization. For instance,

- If ψ is convex, and its proximity operator has a closed form expression (e.g., ψ is the ℓ_1 or ℓ_2 norm), proximal algorithms [45, 44] which include ADMM [21] and primal-dual methods [78] can be used.
- If ψ is Lipschitz-differentiable, but not necessarily convex (e.g. smooth approximations of ℓ_1 or ℓ_0), then the problem can be solved using Majoration-Minimization (MM) schemes [131, 73], which have shown their efficiency in the context of image tomography [40, 39].

In this work, we consider to minimize the problem as mentioned in Section 3.3.3,

$$\underset{d\in\mathbb{R}^m}{\text{minimize}} \quad \frac{1}{2}\|p - Ad\|^2 + g(d) \tag{4.18}$$

where g is defined as follows

$$(\forall d \in \mathbb{R}^m) \quad g(d) = \quad \Psi(Ld) - \alpha D(d) + \frac{\gamma}{2}\|d\|^2 + \kappa Q(d) \tag{4.19}$$

where $\Psi\colon \mathbb{R}^m \to \mathbb{R}$ is the SATV regularization as depicted in (4.12)-(5.5). Moreover, we consider a Lipschitz-differentiable ψ function defined as following,

$$(\forall u \in \mathbb{R}^3) \quad \psi(u) = \beta\sqrt{\|u\|_2^2 + \epsilon^2}, \tag{4.20}$$

where $\beta > 0$ is the regularization weight, and $\epsilon > 0$ controls the smoothness of the penalty function. Since all the involved terms of Problem (4.18)-(4.19)-(4.9) are now differentiable, we will resort to a Majorize-Minimize (MM) algorithm tailored for such smooth function, that will be detailed in Chapter 5.

§ 4.4 Shape restoration of microcalcifications in different datasets

4.4.1 Experimental settings

We now present experimental results assessing the performance of our method on both physical phantom and several clinical datasets, that will be further detailed in sections 4.4.2 and 4.4.3. In this regard, we consider the same experimental settings as detailed in Section 3.4.1. We construct the volume $(\lambda_i)_{1\leq i\leq m}$ as explained in Section 4.3.1. Therefore, we normalize the detection map $(\mu_i)_{1\leq i\leq m}$. Then, we set up experimentally the threshold ν in (4.8) so that the geometric shape of the detected microcalcifications is preserved, given the obtained detection map. Moreover, the parameter θ is manually finetuned to preserve an optimized transition between breast background and microcalcifications. Finally, we set η in order to achieve a certain image quality optimization of DBT.

4.4.2 Physical phantom data

We have first assessed our approach when using the physical phantom data as described in Section 3.4.2. The constructed map for the weight parameters $(\lambda_i)_{1\leq i\leq m}$ obtained following the approach described in Section 4.3.1 is shown in Figure 4.3. We set $\nu = 1.5 \times 10^{-3}$ and $\theta = \frac{\nu}{3}$.

Compared to the results obtained with a classical DBT reconstruction, in Figure 4.4(a), we observe a significant enhancement of the visibility as well

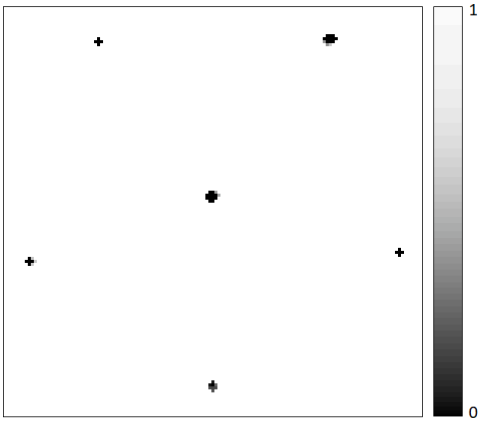

(a)

Figure 4.3: *Region of Model 015 phantom slice containing 6 ROIs : Weights* $(\lambda_i)_{1\leq i\leq m}$.

as the sharpness of the detected microcalcifications (Figure 4.4(c)). This gain in enhancement is spotlighted in Table 4.2 through the SDNR values. Moreover, we see a reduction of the spreading effect affecting the microcalcifications when the reconstruction uses the classical TV, in Figure 4.4(b). We emphasize that the comparison between the SATV-based reconstruction and the classical TV-based reconstruction is fair, since the regularization parameters, namely β and η are set such that the background is restored with the same quality. These regularization parameters, namely (β, ϵ, η), are presented in Table 4.1. This observation is highlighted through similar mean and standard deviation values observed on the different reconstructed images, as shown in Table 4.2.

Table 4.1: *The parameters value of the classical TV-based regularization and the SATV-based regularization for the physical phantom case.*

TV version	(β, ϵ, η)
Classical TV-based regularization	$(600, 10, 0)$
SATV-based regularization	$(630, 10, 0.048)$

Table 4.2: *Statistics on the region of Model 015 phantom slice containing 6 ROIs for different DBT reconstructions.*

(α, β, η)	**Mean**	**StD**	**Max**	**SDNR**
$(0, 600, 0)$	2340.93	22.90	2667	11
$(750, 600, 0)$	2336.85	22.99	2981	18
$(750, 630, 0.048)$	2334.97	23.38	4095	71

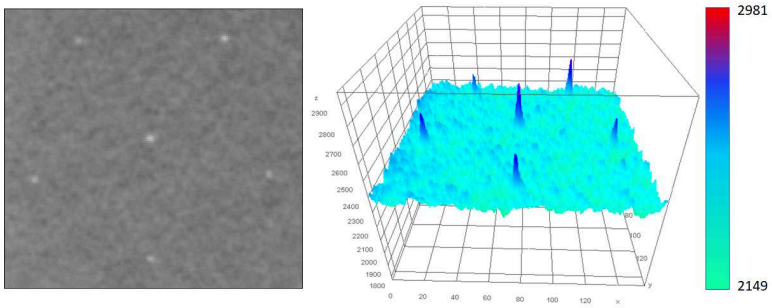

(a) $\alpha = 0, \beta = 600, \eta = 0$

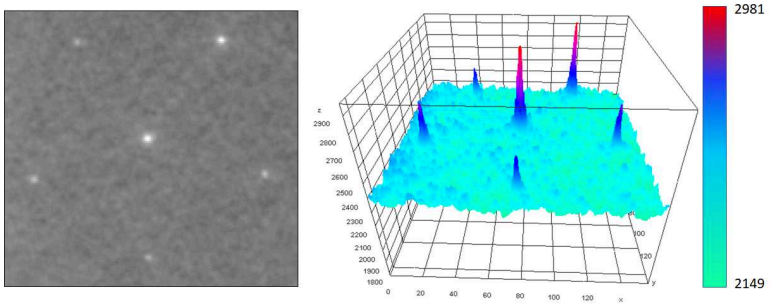

(b) $\alpha = 750, \beta = 600, \eta = 0$

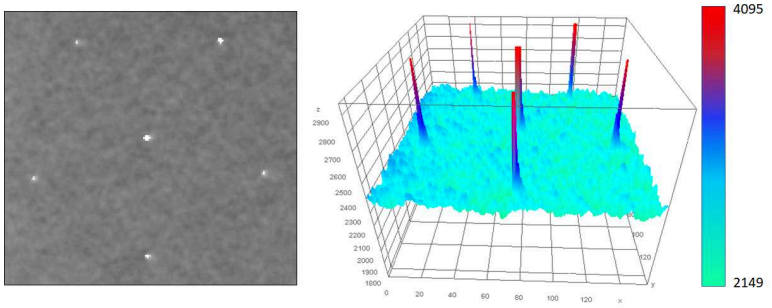

(c) $\alpha = 750, \beta = 630, \eta = 0.048$

Figure 4.4: *Region of Model 015 phantom slice containing 6 ROIs : (a) TV. (b) dTV. (c) DBT reconstruction with detectability function and SATV regularization (dSATV).*

To better grasp the aforementioned observations, we focus on the central microcalcification where the shape preservation is the most obvious. Therein, a DBT reconstruction with detectability function and SATV regularization, as shown in Figure 4.5(c), enables when compared to Figure 4.5(a)-(b), first, a high restoration of the background similarly to a TV-based reconstruction and second, a sharper microcalcification with a significant enhancement.

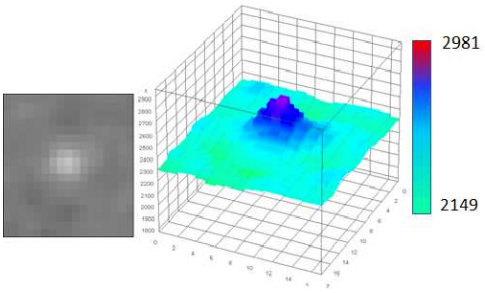

(a) $\alpha = 0, \beta = 600, \eta = 0$

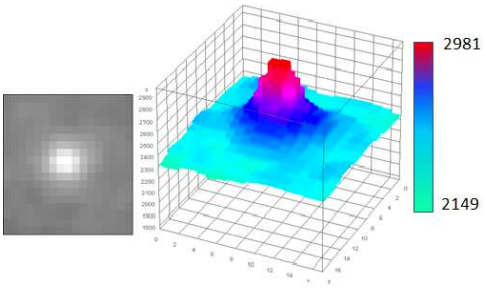

(b) $\alpha = 750, \beta = 600, \eta = 0$

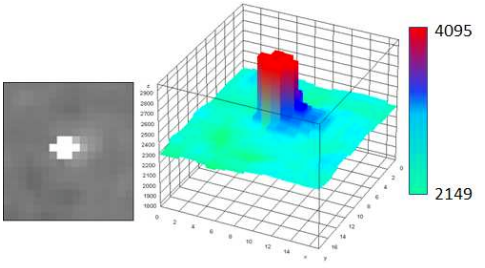

(c) $\alpha = 750, \beta = 630, \eta = 0.048$

Figure 4.5: *Zoom on the central microcalcification contained in the considered region of Model 015 phantom slice : (a) TV. (b) dTV. (c) dSATV.*

4.4.3 Clinical data

We have also evaluated our approach on the clinical images. We propose to show representative cases that include inconspicuous microcalcifications. First, we evaluate our approach on cases containing benign microcalcifica-

tions. Then, we extend our evaluation on a case comprising a potentially malignant group of microcalcifications.

Clinical cases with benign microcalcifications :
We illustrate in Figure 4.6 results for a clinical case with a BI-RADS d breast composition containing an isolated microcalcifications and in Figure 4.7 and 4.8, for a clinical case with a BI-RADS c breast composition comprising a group of microcalcifications. The corresponding detection maps are shown in Figure 4.6(a), Figure 4.7(a) and Figure 4.8(a) respectively. The constructed maps for $(\lambda_i)_{1\leq i\leq m}$ obtained following the approach described in Section 4.3.1 are shown in Figure 4.6(b), Figure 4.7(b) and Figure 4.8(b). Furthermore, we set $\theta = \nu/3$, with $(\nu, \alpha) = (0.09, 1500)$ for the first example and $(\nu, \alpha) = (0.03, 2500)$ for the second volume. The regularization parameters, namely (β, ϵ, η), are presented in Table 4.3. Here again, the reconstruction with our proposed approach and the one based on classical TV visually provide the same breast texture quality. This qualitative observation is verified by the standard deviation values reported in Table 4.4, Table 4.5 and Table 4.6 related to each volume respectively.

Furthermore, similar conclusions as for the physical phantom case, can be drawn from a visual inspection of those images. We highlight the advantage of our proposed approach (Figure 4.6(g), Figure 4.7(g) and Figure 4.8(g)) that simultaneously enables a robust preservation of the enhanced microcalcification shape and a high quality restoration of the background.

Table 4.3: *The parameters value of the classical TV-based regularization and the SATV-based regularization for the clinical scenario.*

TV version	(β, ϵ, η)
classical TV-based regularization	$(600, 10, 0)$
SATV-based regularization	$(660, 10, 0.09)$

Table 4.4: *Statistics on a selected slice of a DBT reconstruction with size* $2344 \times 868 \times 44$ *(voxels)*

(α, β, η)	**Mean**	**StD**	**Max**	**SDNR**
$(0, 600, 0)$	1686.06	693.53	2584	1
$(1500, 600, 0)$	1686.73	693.70	3649	3
$(1500, 660, 0.09)$	1686.70	693.73	3926	3

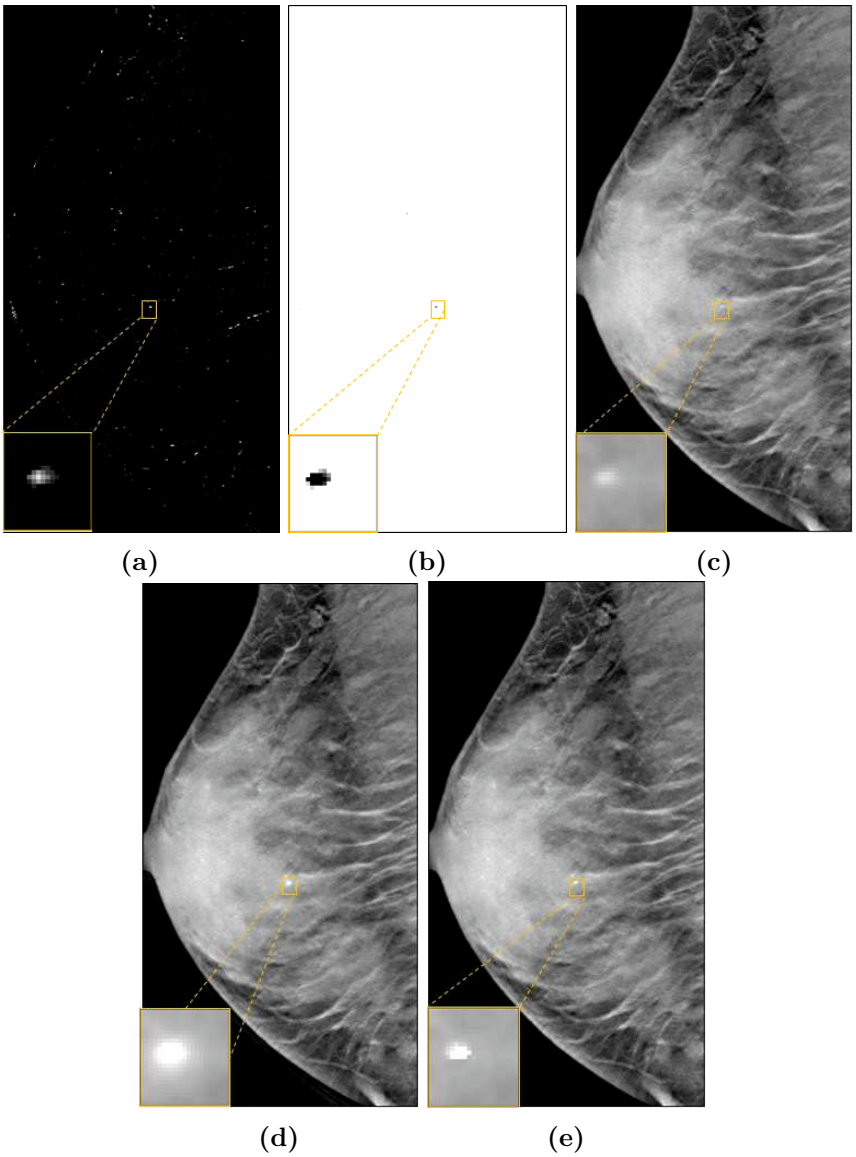

Figure 4.6: *Selected slice of a DBT reconstruction with size* $2344 \times 868 \times 44$ *(voxels) (a) Detection map* μ*. (b) Weights* $(\lambda_i)_{1 \leq i \leq m}$*. (c) TV. (d) dTV. (e) dSATV.*

Table 4.5: *Statistics on a selected slice of a DBT reconstruction with size* $594 \times 2346 \times 46$ *(voxels)*

(α, β, η)	**Mean**	**StD**	**Max**	**SDNR**
$(0, 600, 0)$	1484.84	772.92	2621	1
$(2500, 600, 0)$	1489.97	775.67	2775	2
$(2500, 660, 0.09)$	1492.01	779.59	3919	3

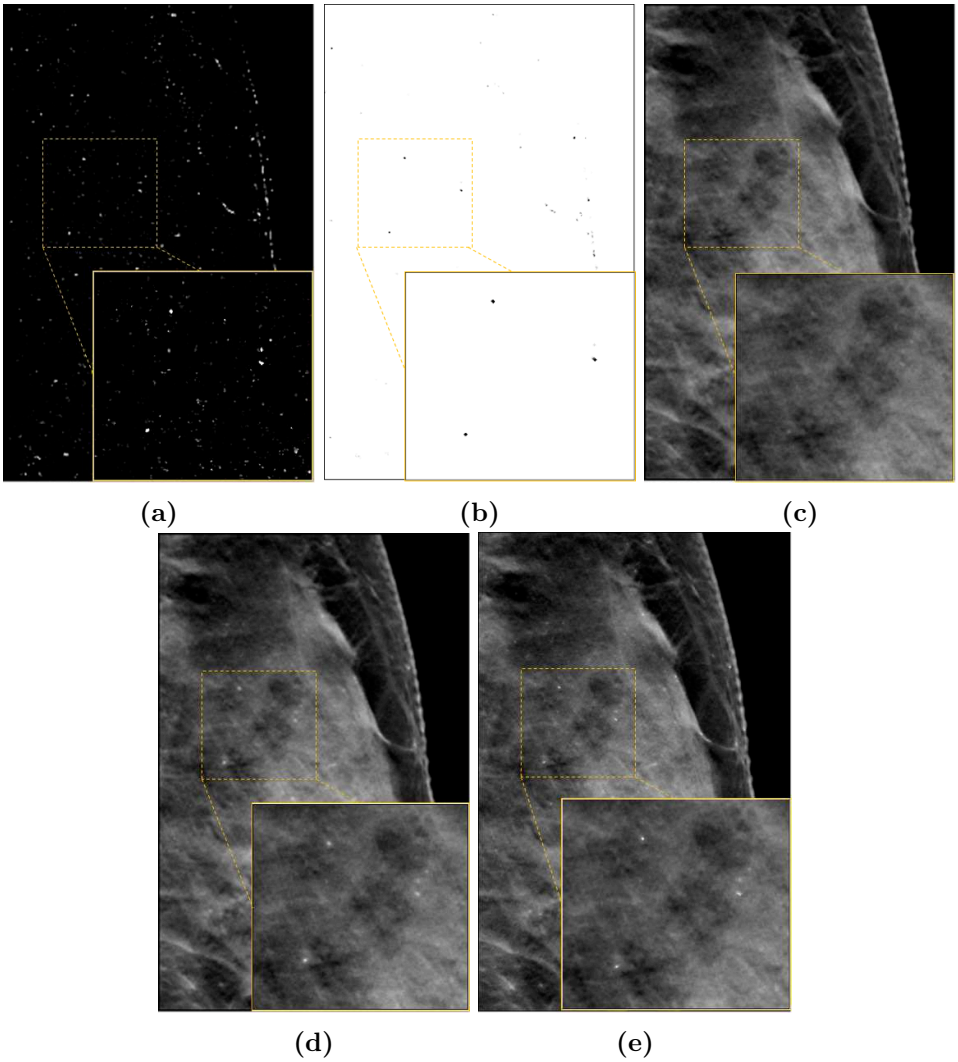

Figure 4.7: *Selected slice of a DBT reconstruction with size* $594 \times 2346 \times 46$ *(voxels) (a) Detection map* μ*. (b) Weights* $(\lambda_i)_{1 \leq i \leq m}$*. (c) TV. (d) dTV. (e) dSATV.*

Table 4.6: *Statistics on a selected slice of a DBT reconstruction with size* $594 \times 2346 \times 46$ *(voxels)*

(α, β, η)	**Mean**	**StD**	**Max**	**SDNR**
$(0, 600, 0)$	1485.20	776.17	2717	2
$(2500, 600, 0)$	1491.81	779.41	2732	2
$(2500, 660, 0.09)$	1490.25	775.91	3917	3

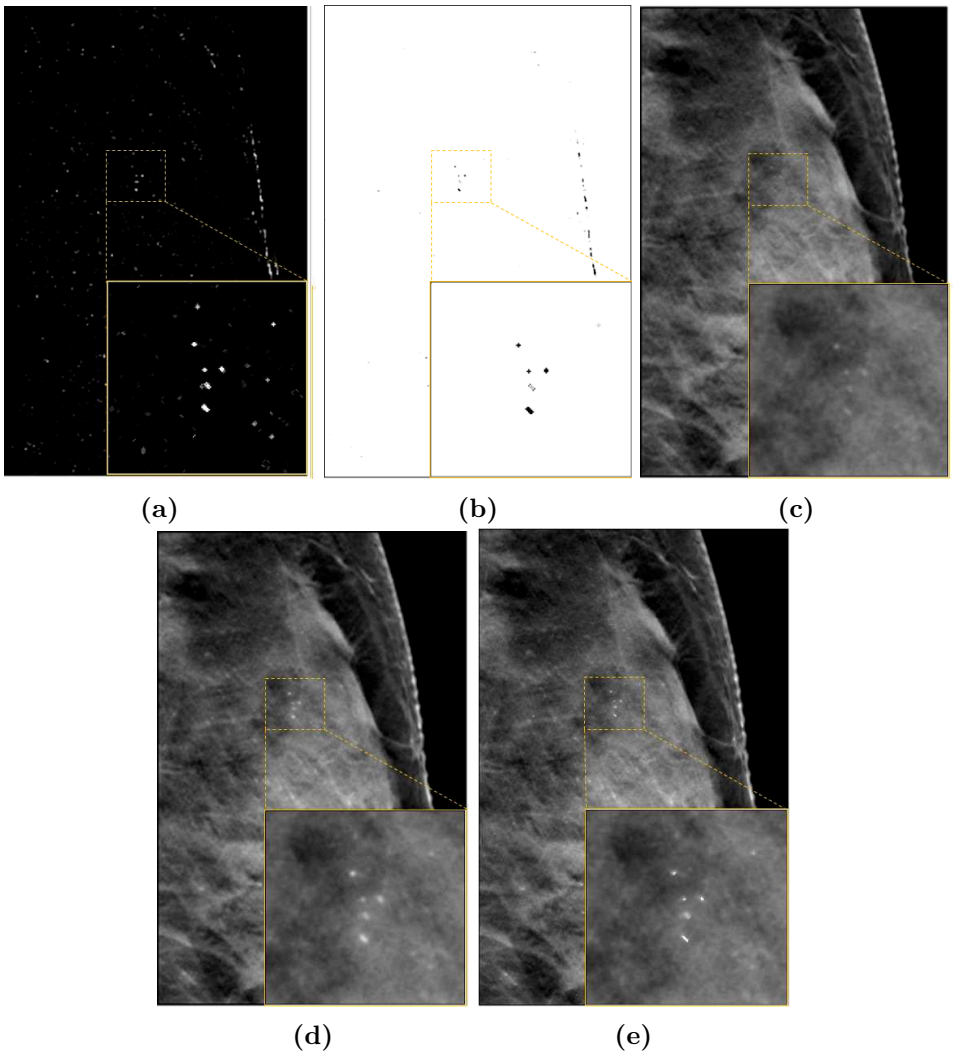

Figure 4.8: *Selected slice of a DBT reconstruction with size* $594 \times 2346 \times 46$ *(voxels) (a) Detection map* μ*. (b) Weights* $(\lambda_i)_{1 \leq i \leq m}$*. (c) TV. (d) dTV. (e) dSATV.*

Clinical cases with potentially malignant cluster of microcalcifications:
We show in Figure 4.9 results for a clinical case with a BI-RADS c breast composition exhibiting a potentially malignant group of microcalcifications. The corresponding detection map is illustrated in Figure 4.9(a). Furthermore, the constructed map for $(\lambda_i)_{1\leq i\leq m}$ obtained following the approach described in Section 4.3.1 is shown in Figure 4.9(b). Herein, we set $\theta = \nu/3$, with $(\nu, \alpha) = (0.009, 500)$. Regarding the hyperparameters, we used (β, ϵ, η) as depicted in Table 4.3. Here again, SATV and TV regularizations enable the reconstruction of the same texture quality which is depicted through the standard deviation values in Table 4.7.

Moreover, we observe the behaviour already unveiled in the physical phantom data as well as in the aforementioned clinical cases. By combining the SATV regularization and the detectability function (Figure 4.9(d)), we enable simultaneously a high restoration of the background while preserving the sharpness of the enhanced microcalcifications.

Nevertheless, we may observe some lesion-like structures enhanced in Figure 4.9(d). This is due to the choice of the threshold ν that is involved in the construction of the weight parameters $(\lambda_i)_{1\leq i\leq m}$. The latter threshold enables the preservation of the shape of the microcalcifications while it controls the False Positives (FP). Furthermore, it is directly deduced from the detection map $(\mu_i)_{1\leq i\leq m}$. Thus, we can infer that the construction quality of the weight parameters $(\lambda_i)_{1\leq i\leq m}$ depends highly on the detection power of the detection map.

Table 4.7: *Statistics on a selected slice of a DBT reconstruction with size* $3062 \times 994 \times 67$ *(voxels)*

(α, β, η)	**Mean**	**StD**	**Max**	**SDNR**
$(0, 600, 0)$	2042.64	738.78	3206	2
$(500, 600, 0)$	2035.34	740.90	4009	3
$(500, 660, 0.09)$	2038.30	739.58	4006	3

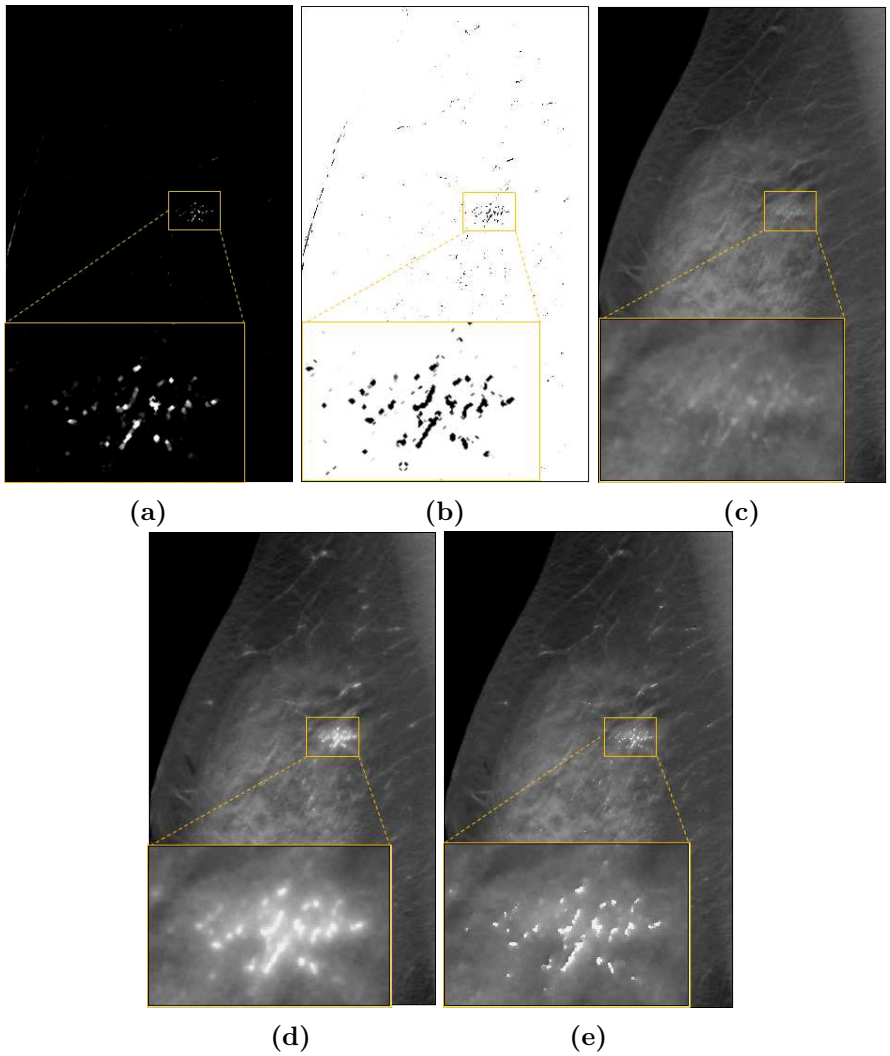

Figure 4.9: *Selected slice of a DBT reconstruction with size* $3062 \times 994 \times 67$ *(voxels) (a) Detection map* μ*. (b) Weights* $(\lambda_i)_{1\leq i\leq m}$*. (c) TV. (d) dTV. (e) dSATV.*

§ 4.5 Summary

Despite the tremendous amount of research works highlighting the success of TV in various image processing applications, this penalty does not model properly the heterogeneity within images. In this chapter, our main contribution lies in introducing a new Spatially adaptive Total Variation (SATV) regularization with the detectability function in DBT reconstruction. Henceforth, we have formulated a new definition for the weighted gradient field by integrating a priori knowledge on microcalcification spatial location. Second,

we have integrated the SATV as a regularization term in DBT reconstruction. Finally, we have demonstrated on different datasets the interest of our approach which constitutes a promising way of improving state-of-the-art methods.

It is worth mentioning that SATV regularization could be used in other image processing applications (e.g., astronomy) that involve both localized objects and homogeneous areas. A future direction for further improvements is to investigate a more automatic setting of the different parameters involved in SATV, depending on the targeted task and images to be processed.

- Chapter 5 -

Application of Majorize-Minimize Memory Gradient (3MG) algorithm to the proposed DBT reconstruction

§ 5.1 Introduction

As detailed in Chapter 4, the DBT reconstruction problem amounts to minimizing the objective function:

$$(\forall d \in \mathbb{R}^m) \quad f(d) = \frac{1}{2}\|p - Ad\|^2 + \Psi(Ld) - \alpha D(d) + \frac{\gamma}{2}\|d\|^2 + \kappa Q(d). \quad (5.1)$$

where D, Ψ and Q are defined by (3.11), (4.12) and (3.24), respectively. Majorize-Minimize (MM) algorithms rely on successive majorizing approximations of function f in order to produce a sequence of iterates that will converge to a solution to the problem, under suitable assumptions. The MM framework gives rise to a class of efficient and flexible optimization algorithms that is grounded on solid theoretical foundations. MM algorithms are very popular in the field of medical image reconstruction [50, 56, 61]. The Majorize-Minimize Memory Gradient (3MG) algorithm falls within this class. Integrating a subspace acceleration strategy in the standard quadratic MM algorithm constitutes one of the most efficient strategies for smooth optimization at large scales [36] and one of the few benefiting from convergence guarantees in the non-convex case [37, 39].

The remainder of this chapter is organized as follows: in Section 5.2 we first formulate 3MG algorithm when applied to Problem (5.1). Then, we propose two numerical improvements of the algorithm, which aim to further improve the speed of the reconstruction process in Section 5.3. Finally, we assess the numerical performance of 3MG algorithm in Section 5.4 by

comparing the convergence speed of the proposed method with those of standard convex optimization algorithms.

§ 5.2 Majorize-Minimize Memory Gradient method

5.2.1 Subspace algorithm

A classic strategy to minimize the criterion f involves building a sequence $(d^{(j)})_{j\in\mathbb{N}}$ of vectors in $\mathbb{R}^m$ such that

$$(\forall j \in \mathbb{N}) \quad f(d^{(j+1)}) \leq f(d^{(j)}). \tag{5.2}$$

This can be carried out by translating the current solution $d^{(j)}$ at each iteration $j \in \mathbb{N}$ along an appropriate direction $c^{(j)} \in \mathbb{R}^m$:

$$(\forall j \in \mathbb{N}) \quad d^{(j+1)} = d^{(j)} + \alpha^{(j)} c^{(j)}. \tag{5.3}$$

where $\alpha^{(j)} > 0$ is the step size, and $c^{(j)}$ is a descent direction. When the criterion to be minimized is differentiable, which is the case for f, this direction is chosen such that $(\nabla f(d^{(j)}))^\top c^{(j)} \leq 0$ where $\nabla f(d^{(j)})$ denotes the gradient of f at $d^{(j)}$ [18]. At the aim of improving the convergence rate, a set of M search directions $\{c_1^{(j)}, \ldots, c_M^{(j)}\} \subset \mathbb{R}^m$ can be considered. Then iteration (5.3) can be defined as following

$$(\forall j \in \mathbb{N}) \quad d^{(j+1)} = d^{(j)} + B^{(j)} u^{(j)}. \tag{5.4}$$

where $B^{(j)} = [c_1^{(j)}, \ldots, c_M^{(j)}] \in \mathbb{R}^{m\times M}$ is the search direction matrix and $u^{(j)} \in \mathbb{R}^M$ is a multivariate step size, which is determined so as to minimize on $\mathbb{R}^M$

$$u \mapsto f(d^{(j)} + B^{(j)} u). \tag{5.5}$$

By choosing $M > 1$, this may enable a faster convergence in terms of the required number of iterations to reach the solution [38]. Yet, when M is large, the cost per iteration may be more complex than a usual line search. Henceforth, the dimension of the subspace is crucial to achieve a tradeoff between the required number of iterations to reach convergence and the cost per iteration.

In particular, the memory gradient subspace algorithm, initially proposed in [98], is defined as:

$$(\forall j \in \mathbb{N}) \quad B^{(j)} = \begin{cases} [-\nabla f(d^{(j)}) & 0] & \text{if } j = 0 \\ [-\nabla f(d^{(j)}) & d^{(j)} - d^{(j-1)}] & \text{if } j > 0, \end{cases} \tag{5.6}$$

where $d^{(0)} \in \mathbb{R}^m$ is an initial volume and $B^{(j)} \in \mathbb{R}^{m\times 2}$ reduces to a stack of a gradient descent direction and the difference between $d^{(j)}$ and $d^{(j-1)}$,

the current and the previous iterates respectively. The subspace framework (5.4)-(5.6) was shown to lead to a fast convergence on several examples in the field of signal and image restoration [62, 40, 146]. Yet, to guarantee the convergence of (5.4)-(5.6), a proper strategy should be adopted to compute the step sizes $(u^{(j)})_{j\in\mathbb{N}}$ where, for every $j \in \mathbb{N}$, $u^{(j)} \in \mathbb{R}^2$, which is detailed hereafter.

5.2.2 Majorize-Minimize framework

To compute the step size $u^{(j)} \in \mathbb{R}^2$ at iteration $j \in \mathbb{N}$, function (5.5) is minimized using the Majorization-Minimization (MM) principle [106]. The idea behind the MM approach is to perform successive minimizations of some surrogate functions defined as tangent majorant functions for f.

Let $d' \in \mathbb{R}^m$. A function $q(.,d')$ is said to be a *tangent majorant* for f at d', if for every $d \in \mathbb{R}^m$,

$$q(d,d') \geq f(d) \quad \text{and} \quad q(d',d') = f(d'). \tag{5.7}$$

Following [39] and since f is differentiable, we construct a quadratic tangent majorant function for f at d', taking the form:

$$(\forall d \in \mathbb{R}^m) \quad q(d,d') = f(d') + \nabla f(d')^\top (d-d') + \frac{1}{2}(d-d')^\top \mathcal{M}(d')(d-d') \tag{5.8}$$

where $\nabla f(d')$ denotes the gradient of f at d' and $\mathcal{M}(d') \in \mathbb{R}^{m\times m}$ is a symmetric positive definite matrix that ensures the majorization properties (5.7). Then, the minimization of f is substituted by a less complicated subproblem, corresponding to the following MM Algorithm 3 :

Algorithm 3: Majorize-Minimize algorithm

```
Initialization with d^(0) ∈ R^m,
for j = 1, ..., J_max do
    d^(j+1) = minimize_{d∈R^m}  q(d, d^(j)) ;
end
```

An illustration of the MM principle is shown in Figure 5.1. The MM framework combined with the subspace strategy (5.4) and (5.6) yields the Majorize-Minimize Memory Gradient (3MG) algorithm [40, 35].

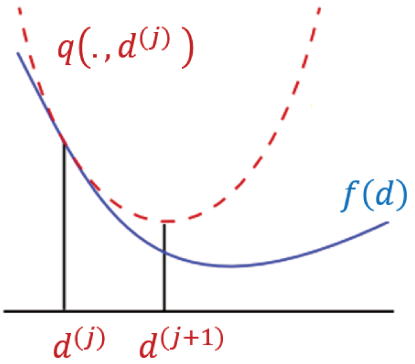

Figure 5.1: *An illustrative example of the Majorize-Minimize strategy : at each iteration $j \in \mathbb{N}$, a tangent majorant $q(.,d^{(j)})$ of f at $d^{(j)}$ is built and the next iterate $d^{(j+1)}$ is defined as the minimizer of $q(.,d^{(j)})$.*

5.2.3 Construction of the majorizing approximation

We focus on the criterion f defined in Problem (5.1), where we consider SATV regularization function Ψ which is detailed in Section 4.3.2.

Thus, to construct the majorizing approximation, we make the following assumptions:

(i) f is differentiable with a β-Lipschitzian gradient, i.e.

$$(\forall d \in \mathbb{R}^m)(\forall d' \in \mathbb{R}^m) \quad \|\nabla f(d) - \nabla f(d')\| \leq \beta \|d - d'\|. \tag{5.9}$$

(ii) ψ defined in (4.20) is a differentiable function.

(iii) $\psi(\sqrt{.})$ is concave on $[0, +\infty)$.

(iv) There exists $\bar{\omega} \in [0, +\infty)$ such that $(\forall t \in (0, +\infty))\ 0 \leq \dot{\psi}(t) \leq \bar{\omega} t$ where $\dot{\psi}$ is the derivative of ψ. In addition, ω is defined as follows

$$(\forall t \in \mathbb{R}) \quad \omega(t) = \begin{cases} \frac{\dot{\psi}(t)}{t} & \text{if } t \neq 0 \\ \lim_{\substack{a \to 0 \\ a \neq 0}} \frac{\dot{\psi}(a)}{a} & \text{otherwise.} \end{cases} \tag{5.10}$$

Note that Assumptions (iii)-(iv) are relevant to a large class of penalty functions, e.g.

- ℓ_2-ℓ_1 functions, i.e. convex, continuously differentiable, asymptotically linear functions with a quadratic behavior near 0 [4, 146, 39].
- ℓ_2-ℓ_0 functions, i.e. asymptotically constant functions with a quadratic behavior near 0 used to approximate the ℓ_0 pseudo-norm [51].

Under the assumptions (i)-(iv) and by using the same procedure than in [39], we can show that the matrix $\mathcal{M}$ can be defined as

$$(\forall d \in \mathbb{R}^m) \quad \mathcal{M}(d) = A^\top A + L^\top \mathrm{Diag}\{b(d) \otimes \delta\} L + (\gamma + 2\kappa) I_m. \tag{5.11}$$

Hereabove, $b(d) = (b_i(d))_{1 \leq i \leq m} \in \mathbb{R}^m$ is such that, for every $i \in \{1, \dots, m\}$,

$$b_i(d) = \omega(\|(Ld)_i\|) \tag{5.12}$$

By applying (5.10) on (5.12), we deduce for every $i \in \{1, \dots, m\}$,

$$b_i(d) = \beta(\|(Ld)_i\|^2 + \epsilon^2)^{-1/2} \tag{5.13}$$

where $(Ld)_i$ is the i-th block of 3 components of Ld, with L defined in (4.14).

5.2.4 Formulation of the algorithm

At each iteration $j \in \mathbb{N}$, the step size $u^{(j)}$ is obtained by minimizing the quadratic function $u \mapsto q(d^{(j)} + B^{(j)}u, d^{(j)})$, which yields the following closed form expression:

$$u^{(j)} = -((B^{(j)})^\top \mathcal{M}(d^{(j)}) B^{(j)})^\dagger (B^{(j)})^\top \nabla f(d^{(j)}), \tag{5.14}$$

where † denotes the pseudo-inverse operation. The 3MG algorithm iterates over Steps (5.6), (5.14), and (5.4). The convergence of the sequence $(d^{(j)})_{j \in \mathbb{N}}$ produced by 3MG to the minimizer of the strongly convex function f is secured [39]. In practice, we initialize the 3MG algorithm by using $d^{(0)}$ as the Filtered Backprojection (FBP) reconstruction and we implement a maximum iteration number $J_{\max}$, leading to Algorithm 4.

Algorithm 4: 3MG Algorithm for DBT reconstruction

```
Initialization with d^(0) obtained by FBP,
for j = 1, ..., J_max do
    For all i ∈ {1, ..., m}, set b_i(d^(j)) using (5.13);
    Construct M(d^(j)) using (5.11);
    Build B^(j) using (5.6);
    Calculate u^(j) using (5.14);
    Update d^(j+1) = d^(j) + B^(j) u^(j);
end
```

§ 5.3 Numerical improvements of 3MG algorithm

Function Q defined in (3.24) penalizes the distance of each component of d to the hypercube $[0, d_{\max}]^m$. The strength of this penalization is controlled

through the weight κ. The greater κ, the closer κQ to the indicator function of the hypercube, hence the more faithfully the constraints are fulfilled. However, increasing κ also induces an increase of the curvature of the majorizing function q, leading in practice to a slowdown of the convergence of the 3MG algorithm, in practice. To address this issue, we propose two modifications in the Algorithm 4 explained hereafter.

5.3.1 Construction of a local majoration

We first substitute (5.11) by

$$(\forall d \in \mathbb{R}^m) \quad \widetilde{\mathcal{M}}(d) = A^\top A + L^\top \mathrm{Diag}\{b(d) \otimes \delta\} L + \gamma I_m + \mathrm{Diag}\{s(d)\}, \quad (5.15)$$

where, for every $i \in \{1, \ldots, m\}$, the i-th component of vector $s(d)$ is

$$s_i(d) = \begin{cases} 0 & \text{if } d_i \in [0, d_{\max}] \\ 2\kappa & \text{otherwise.} \end{cases} \quad (5.16)$$

This amounts to relaxing the majorizing assumption (5.7) by considering only a local majoration for f in the neighborhood of the current iterate.

5.3.2 Iteration-varying κ

Second, in order to further mitigate the negative impact of a large value of κ, which allows to adjust the range value constraint term, on the convergence speed, we propose to progressively increase this weight along the number of iterations by implementing the following rule

$$(\forall j \in \mathbb{N}) \quad \kappa^{(j)} = \kappa_{\max} \frac{j}{j + \xi} \quad (5.17)$$

where $\kappa_{\max}$ is a maximum value for $(\kappa^{(j)})_{j \in \mathbb{N}}$ and $\xi \geq 0$ is a parameter controlling the evolution of this sequence along the number of iterations. When j goes to infinity, $\kappa^{(j)} \to \kappa_{\max}$. Herein, we highlight three scenarios for ξ value :

- When $\xi = 0$, a constant parameter $\kappa^{(j)} \equiv \kappa_{\max}$ is retrieved.
- With small values of ξ, a large penalization weight is obtained from the very beginning of the algorithm.
- With large values of ξ, a more gradual penalization over the pixel intensity is performed.

§ 5.4 Numerical performance of 3MG algorithm

In this section, we aim at evaluating the practical convergence profile of the proposed reconstruction approach. For this purpose, we conduct a comparison of the convergence speed with two state-of-the-art optimization methods, namely the Projected Gradient Descent (PGD) [25] which is detailed in Section 5.4.1 and Fast Iterative Shrinkage-Thresholding Algorithm (FISTA) [27] presented in Section 5.4.2. Our experimental results are shown in Section 5.4.3.

5.4.1 Projected Gradient Descent

Projected Gradient Descent (PGD) is one of the simplest first order optimization methods. Recall that the values of the reconstructed volume lie in a specific range of values $[0, d_{\max}]$, a property which can be formulated as a constraint in our optimization problem. In this context, we consider the projected gradient descent, a variant of the gradient descent which is used to minimize a smooth function subject to a certain constraint. Henceforth, our function g to be minimized reads

$$(\forall d \in \mathbb{R}^m) \quad g(d) = \frac{1}{2}\|p - Ad\|^2 + \Psi(Ld) - \alpha D(d) + \frac{\gamma}{2}\|d\|^2 + \iota_{[0,d_{\max}]^m}(d), \quad (5.18)$$

where $\iota_{[0,d_{\max}]^m}$ is the indicator function of the closed and convex constraint set corresponding to the plausible dynamic range. Below we detail the steps of the projected gradient descent algorithm.

Algorithm 5: Projected Gradient Descent

```
Initialization with d^(0) obtained by FBP,
for j = 1, ..., J_max do
    d^(j+1) = P_[0,d_max]^m (d^(j) − λ^(j) ∇g(d^(j))) ;
end
```

Hereabove, $J_{\max}$ denotes the maximum iteration number and $\mathrm{P}_{[0,d_{\max}]^m}$ the projection onto the hypercube $[0, d_{\max}]^m$. We emphasize that, at each iteration j, we set the step size $\lambda^{(j)} = \lambda$ so that

$$0 < \lambda < \frac{2}{\widetilde{\beta}}, \quad (5.19)$$

where $\widetilde{\beta}$ is a Lipschitz constant of the gradient of g hence satisfying:

$$\forall (x, y) \in (\mathbb{R}^m)^2, \quad \|\nabla g(x) - \nabla g(y)\| \leq \widetilde{\beta}\|x - y\|. \quad (5.20)$$

Condition (5.19) ensures the convergence of the algorithm. In our case, a Lipschitz constant of ∇g is given by

$$\widetilde{\beta} = \frac{1}{\|A\|_{\mathrm{S}}^2 + \beta \frac{\|L\|_{\mathrm{S}}^2}{\epsilon} + \gamma}. \tag{5.21}$$

5.4.2 Fast Iterative Shrinkage-Thresholding Algorithm

Under the same smoothness assumptions on function g in (5.18), another popular first-order algorithm called Fast Iterative Shrinkage-Thresholding Algorithm (FISTA) can be applied. The latter one is an accelerated variant of the Forward-Backward algorithm [13]. Compared to PGD, FISTA is a proximal gradient descent incorporating a step of interpolation between the iterates $d^{(j)}$ and $d^{(j-1)}$ to find $d^{(j+1)}$. This interpolation is over-relaxed thanks to a convergent sequence of relaxation parameters which controls the convergence acceleration of the algorithm. Over the years, various choices for this sequence have been suggested to improve the convergence properties of the algorithm. In our study, we have assessed the variant proposed in [27]. Hereafter, we detail the application of the algorithm to our Problem (5.18).

Algorithm 6: FISTA

Initialization with $d^{(0)}$ obtained by FBP, $d^{(-1)} = d^{(0)}$, $t^{(-1)} = 1$
for $j = 0, 1, \ldots, J_{\max}$ **do**
  $\rho^{(j)} = \frac{j}{j+1+a}$;
  $\tilde{d^{(j)}} = d^{(j)} + \rho^{(j)}(d^{(j)} - d^{(j-1)})$;
  $d_{l+1} = \mathrm{P}_{[0,d_{\max}]^m}(\tilde{d^{(j)}} - \lambda \nabla g(\tilde{d^{(j)}}))$;
end

We have to choose the step size λ such that

$$0 < \lambda \leq \frac{1}{\widetilde{\beta}}, \tag{5.22}$$

where $\widetilde{\beta}$ is the Lipschitz constant of ∇g given by (5.21). The latter condition is paramount to ensure the algorithm convergence.

5.4.3 Experimental results

In this part, we illustrate the practical convergence profile of the proposed reconstruction algorithm on a DBT clinical dataset corresponding to a BI-RADS d breast composition. We solve the optimization Problem (5.1) with 3MG method, either using its initial form described in Algorithm 4, or its variants proposed in Section 5.3. We also perform comparisons with

FISTA and PGD explained in Sections 5.4.2 and 5.4.1 respectively. All the algorithms have been initialized with FBP solution and ran until 10^4 iterations. We choose the latter maximum iteration number in order to better evaluate the convergence properties of the assessed algorithms and to ensure that all the algorithms converge approximately to the same solution. We set the elastic net weight $\gamma = 1$ for all the experiments, which allows to ensure the uniqueness of the solution d^* while not degrading the overall image quality of DBT.
For conciseness we refer to :

- Algorithm 4 with modified majorant (5.15) as 3MG$^+$.
- The cases when $\kappa^{(j)} \equiv \kappa_{\max}$ either as 3MG-$\kappa_{\max}$ or 3MG$^+$-$\kappa_{\max}$.
- The cases when the varying rule (5.17) is adopted, either as 3MG-κ^+ and 3MG$^+$-κ^+.

We set $\kappa_{\max} = 10^3$, since it was observed to lead to the same image quality at convergence as when using FISTA and PGD algorithms. Furthermore, we set $\xi = 75$ in (5.17) since it was observed to achieve the best trade-off between convergence speed and image quality.

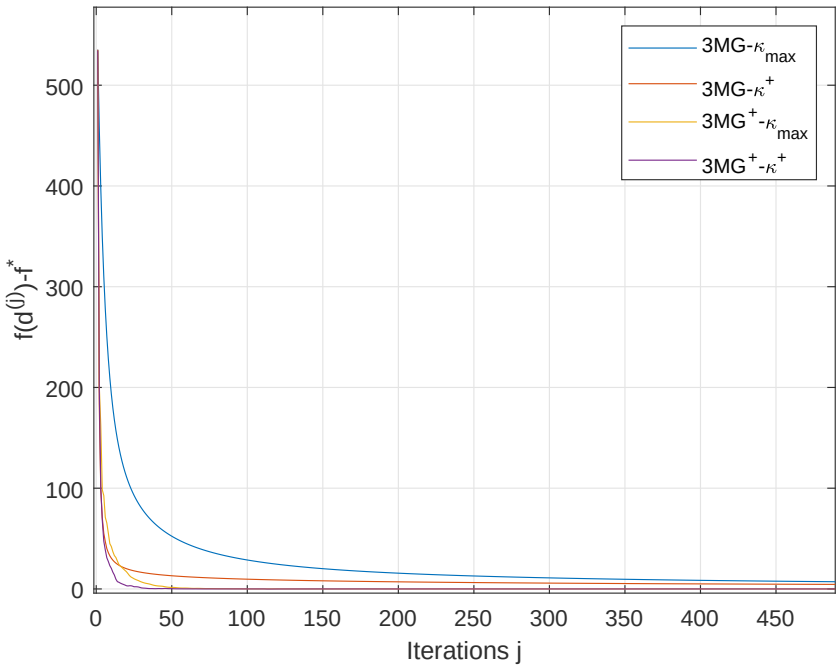

Figure 5.2: *Comparison of 3MG and its variants, on clinical data in terms of $f(d^{(j)}) - f^*$ where f^* corresponds to the cost function value of 3MG$^+$-$\kappa_{\max}$ at iteration 10^4.*

First, we assessed the convergence of 3MG variants by considering the evolution of the criterion f to the value f^*, computed after a large number of iterations equal to 10^4. This is illustrated in Figure 5.2. We note that 3MG$^+$-κ^+ is faster than its counterparts.

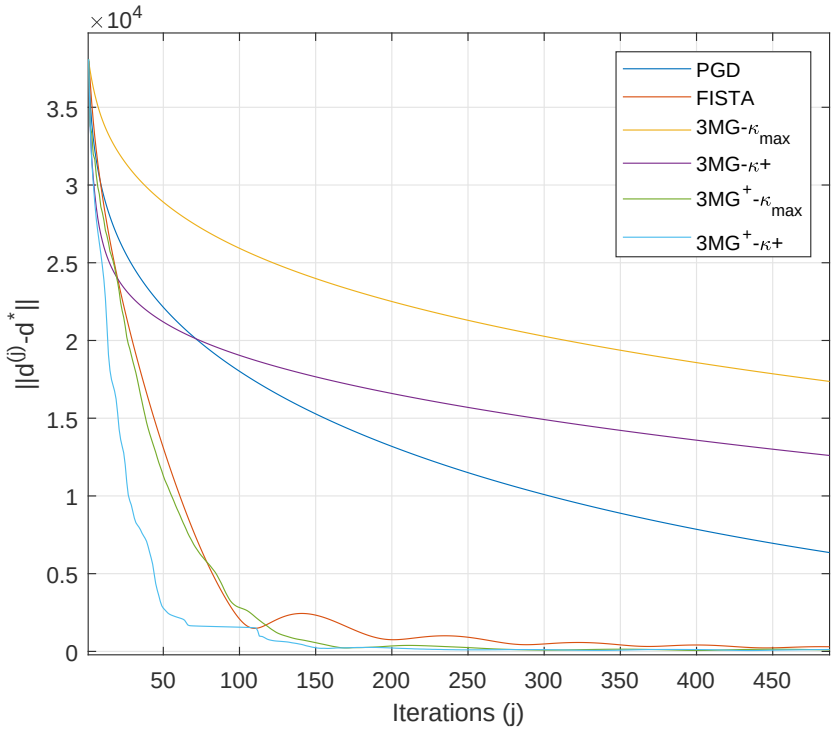

Figure 5.3: *Comparison between 3MG variants and two state-of-the-art methods, on clinical data in terms of* $\|d^{(j)} - d^*\|$ *where* d^* *is the reconstructed volume for each algorithm at iteration* 10^4.

To further highlight this result, we computed the evolution of the distance to the solution d^*, evaluated after a large number of iterations equal to 10^4. PGD and FISTA algorithms are also included in this comparison, as displayed in Figure 5.3. We notice that 3MG-$\kappa_{\max}$, that corresponds to the standard 3MG implementation, leads to the slowest convergence. Furthermore, 3MG$^+$-$\kappa_{\max}$ reaches similar performance to FISTA and 3MG$^+$-κ^+ outperforms the other competitors in terms of convergence speed. Finally, we observe that even though 3MG-κ^+ is faster than 3MG-$\kappa_{\max}$, it remains clearly slower than 3MG$^+$-κ^+. Then, we may infer that the local majorant strategy represents a great boost to the convergence speed of 3MG algorithm. Furthermore, ξ value in the iteration-varying strategy κ may be finetuned for the standard 3MG implementation. More precisely, it might be interesting to investigate larger values of ξ parameter to achieve the best

trade-off between convergence speed of 3MG-κ^+ algorithm and image quality.

§ 5.5 Summary

We have proposed an efficient algorithm based on the Majorize-Minimize Memory Gradient (3MG) scheme, to minimize our proposed objective function. We have conducted a numerical comparison of the convergence speed of the proposed method with those of standard convex optimization algorithms. The practical convergence profile shows the interest of our contribution regarding the numerical improvements of 3MG algorithm applied to our reconstruction approach. Thereby, by combining a local majorant with the iteration-varying κ scheme, 3MG has the best convergence performance. Furthermore, convex optimization algorithms such as PGD and FISTA require the computation of the Lipschitz constant, which may be cumbersome in large-scale simulation scenarios. In contrast, 3MG algorithm has the advantage to enable an automatic computation of the stepsize.

Furthermore, we have observed that the global image quality of the reconstructed DBT volume does not change after a certain number of iterations. From a practical point of view, one could set the stopping criteria based on defining the number of iterations required to obtain a satisfactory approximation to the solution.

- Chapter 6 -

Quantitative assessment of the proposed DBT reconstruction approach

§ 6.1 Introduction

The main goal of our proposed dSATV approach is to yield more conspicuous and enhanced microcalcifications while increasing robustness to noise and improving the overall quality in the imaged volume. So far, we have demonstrated qualitatively these qualities on phantom and several clinical data. To bring insight to the visual contribution of the regularization functions proposed in our dSATV reconstruction approach, we propose in this chapter to perform a quantitative evaluation of its performance. To this aim, we conduct a visual experiment trial where experts compare dSATV and NRLS reconstructions, regarding several aspects including microcalcification conspicuity, rendering of breast structures, presence of potential artifacts and overall visual preference.

The remainder of this chapter is structured as follows: we explain the methodology of the visual experiment study in Section 6.2 by detailing the construction of the image data set and the image review protocol. In Section 6.3, we present and discuss the results of our experiment.

§ 6.2 Visual Experiment settings

6.2.1 Image data set

We have extracted 19 regions of interest from 16 clinical cases corresponding to BI-RADS c and d breast compositions. For each clinical case, 9 projections were acquired using the same DBT system (Senographe Essential, GE Healthcare). In this regard, we consider the same experimental settings as detailed in Section 3.4.1. We constructed the detectability function and the

SATV regularization as explained in Sections 3.4.1 and 4.4.1 respectively. We then reconstructed each case with both the standard non-regularized least squares solution NRLS and our proposed dSATV solution. For the latter, the parameters were set following the same approach as detailed in Sections 3.4 and 4.4, and finally we used the improved 3MG optimization algorithm detailed in Section 5.3 which was initialized with FBP solution and run until a maximum number of iterations (here equal to 200). Each of the 19 regions of interest was $220 \times 220 \times 7$ voxels in size, four of them contain isolated microcalcifications while the remaining ones display various types of microcalcification groups, as illustrated in Figure 6.1 and 6.2 respectively.

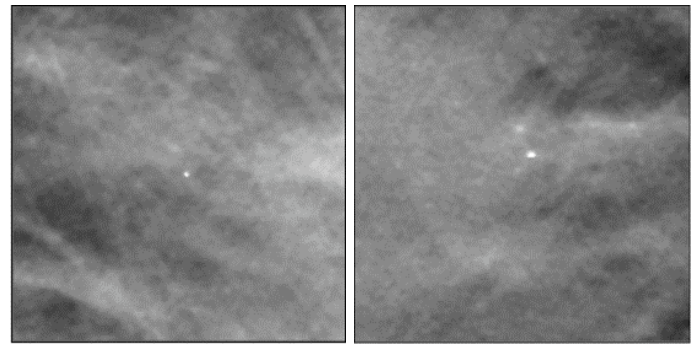

(a) *ROI n°2* **(b)** *ROI n°12*

(c) *ROI n°13* **(d)** *ROI n°17*

Figure 6.1: *Central slice of four extracted regions of interest in clinical cases with isolated microcalcifications, reconstructed with dSATV solution.*

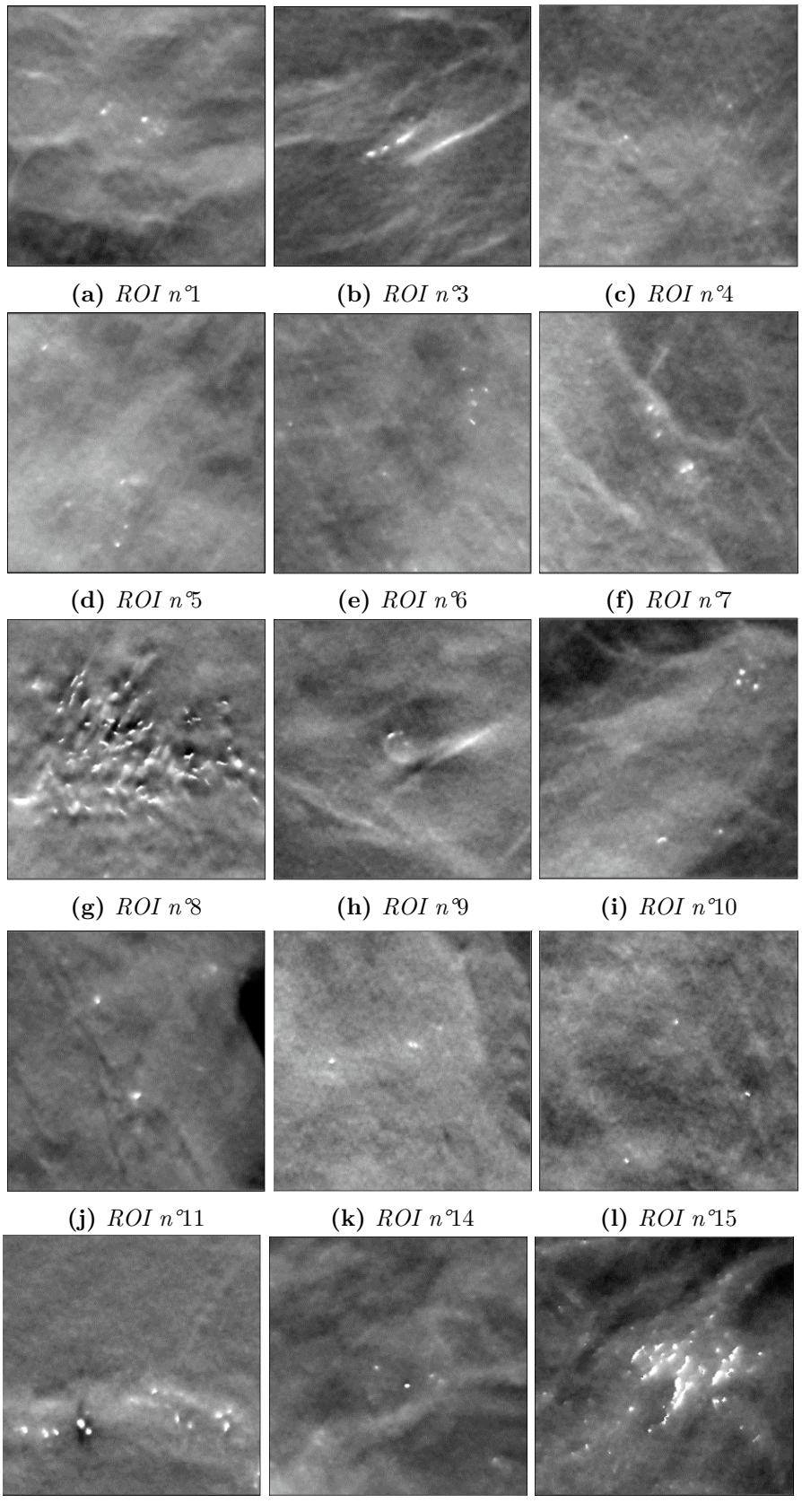

(a) *ROI n°*1 **(b)** *ROI n°*3 **(c)** *ROI n°*4

(d) *ROI n°*5 **(e)** *ROI n°*6 **(f)** *ROI n°*7

(g) *ROI n°*8 **(h)** *ROI n°*9 **(i)** *ROI n°*10

(j) *ROI n°*11 **(k)** *ROI n°*14 **(l)** *ROI n°*15

(m) *ROI n°*16 **(n)** *ROI n°*18 **(o)** *ROI n°*19

Figure 6.2: *Central slice of* 15 *extracted regions of interest in clinical cases presenting various types of microcalcification groups, reconstructed with dSATV solution.*

6.2.2 Image readers

Fourteen qualified participants, namely five GE Healthcare image quality experts in mammography and nine radiologists from **Institut de Radiologie de Paris** and **CSE imagerie médicale numérique, Paris** in France, participated in our visual experiment. We distinguish three different categories of radiologists according to their level of expertise where:

- category "Expert" denotes that the radiologist reads more than 5000 cases per year;
- category "Advanced" denotes that the radiologist reads between 2500 and 5000 cases per year;
- category "Junior" denotes that the radiologist reads less than 2500 cases per year.

We note that three of the radiologists belong to "Expert" category, four of them are in the "Advanced" category and two are in the "Junior" category.

6.2.3 Image review protocol

For each test case, we built visual trials displaying side by side (with random left/right side assignation) both reconstruction results as illustrated in Figure 6.3. No training session was conducted before the actual experiment for all the readers. Each reader reviewed sequentially, in the same order, the 19 trial image pairs. The 7 slices of each image pair were displayed using a cine-loop review mode scrolling back and forth through the stack of slices. This mode enables the reader to appraise the 3D information within each trial. An example of the series of the 7 slices in a trial is displayed in Figure 6.4. Furthermore, between two consecutive trials, a uniform neutral grey level image was displayed to introduce a memory reset stimulus between two successive trials.

For each trial, the reader was asked to choose between right or left image by answering the following questions:

- Q1: In which image the microcalcifications are more conspicuous? (Right/Left)
- Q2: In which image do you see a better representation of the breast structures? (Right/Left)
- Q3: In which image do you see more artifacts? Describe them. (Right/Left, then description)
- Q4: Which image do you prefer overall? (Right/Left)

The readers had no time limitation to answer the questions. Note that a zoom of 100% was used to answer the questions Q1, Q2 and Q4, respectively. To enable a better description of the potential artifacts, a zoom of 150% was used for Q3. Finally, the contrast and the brightness were fixed for all the 19 trial image pairs.

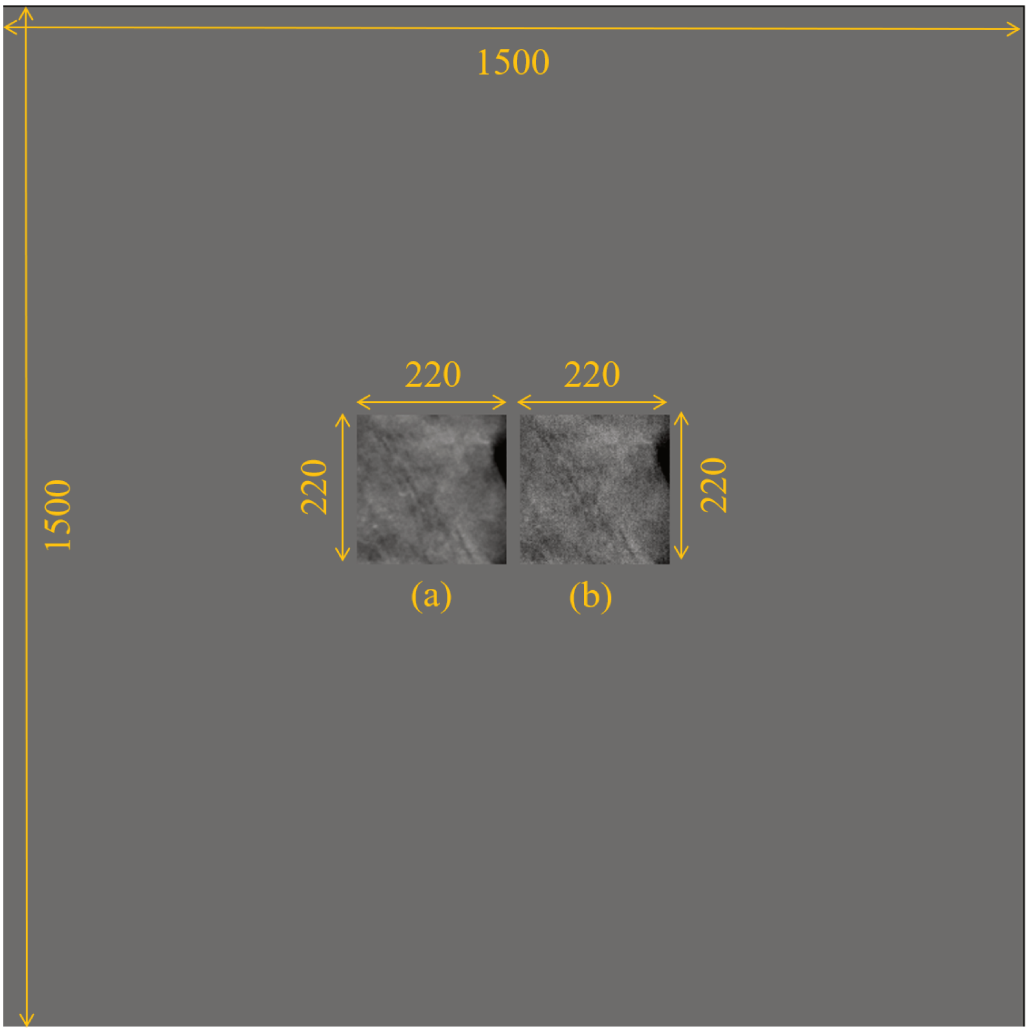

Figure 6.3: *An example of a trial with size* 1500×1500 *in pixels, of a clinical case. In the center, a slice of both reconstruction results, with size* 220×220 *each, put side by side: (a) dSATV and (b) NRLS.*

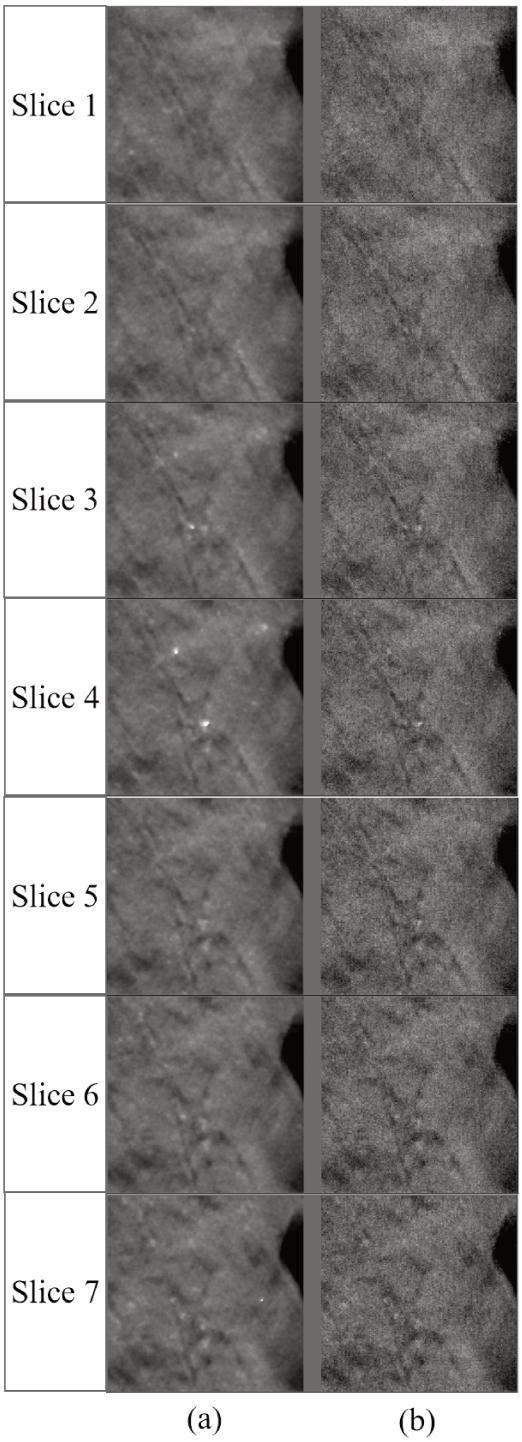

Figure 6.4: *An example of* 7 *slices in a trial, with* 220×220 *pixel images: (a) dSATV and (b) NRLS.*

§ 6.3 Results

In this section, we show and analyze the results of the visual experiment study. Since it was performed in different populations, namely GE Healthcare image quality experts in mammography and radiologists with different levels of expertise, we performed an analysis considering different population sets: all readers, GE Healthcare image quality experts in mammography, all radiologists, expert radiologists, advanced radiologists and junior radiologists.

6.3.1 Descriptive analysis

Due to the limited number of images used in this experiment, we opted for a descriptive analysis of the results. For each question, we show in Figure 6.5 the scoring percentage in favor of dSATV and NRLS approaches pooled over all the readers. The positive end of each box corresponds to the mean-reader preference for dSATV, while the negative end corresponds to the mean-reader preference for NRLS. The top of the positive bar indicates the maximum preference score obtained over the considered group of readers for dSATV, while the top of the negative bar indicates the maximum preference score obtained over the considered group of readers for NRLS.

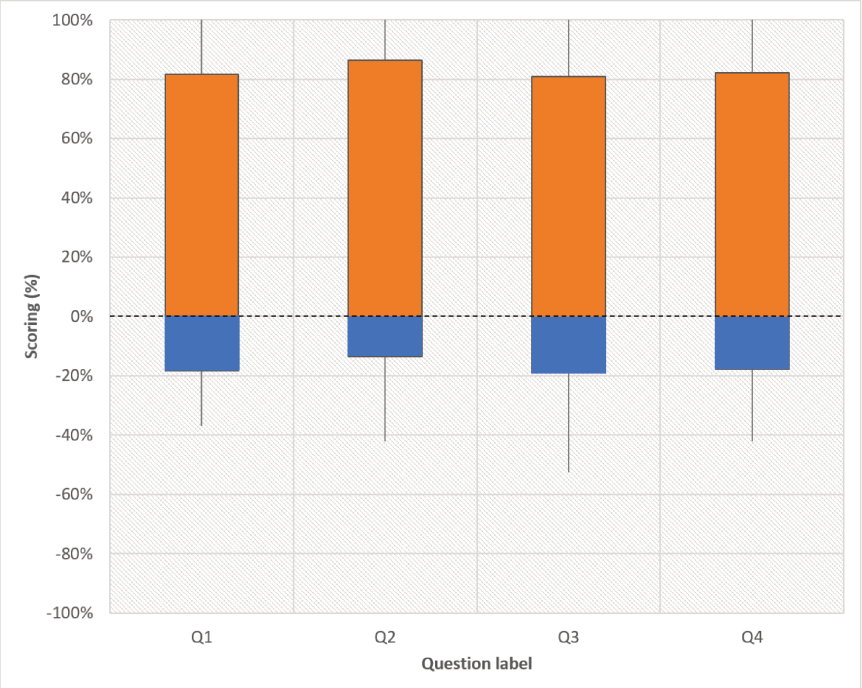

Figure 6.5: *Results of the visual experiment pooled over all the readers: positive scoring is in favor of dSATV, negative scoring is in favor of NRLS.*

By averaging over all the readers, our proposed method provides more conspicuous microcalcifications with $82\%[63\% - 100\%]$ [1] of scores, a better representation of the breast structures with $87\%[58\% - 100\%]$ of scores, less artifacts with $81\%[47\% - 100\%]$ of scores and an overall preference of $83\%[58\% - 100\%]$ of scores.

Pooling over all the fourteen readers, the most frequent artifacts observed in our proposed dSATV approach were the following:

(i) Some undershooting around the microcalcifications (Figure 6.6(a))

(ii) The presence of enhanced structures not identified as microcalcifications (potentially false positives) (Figure 6.6(b))

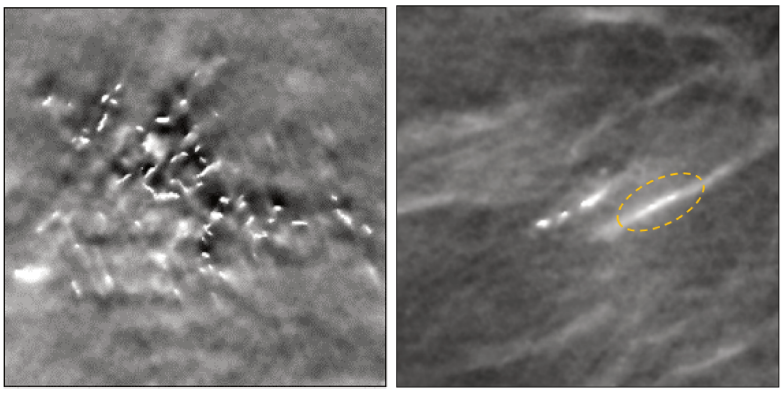

(a) **(b)**

Figure 6.6: *The most observed artifacts in dSATV approach in the visual experiment study pooling over all the readers : (a) Undershooting around the microcalcifications. (b) Enhanced false positive.*

Regarding the non-regularized algorithm NRLS, the most frequently noted artifacts were:

(i) Replication artifacts (Figure 6.7(a))

(ii) Presence of off-focal artifact (Figure 6.7(b))

(iii) Presence of noise (Figure 6.7(c))

(iv) Some undershooting around the microcalcifications for some cases (Figure 6.7(d))

[1] mean value in % [minimum value in %- maximum value in %]

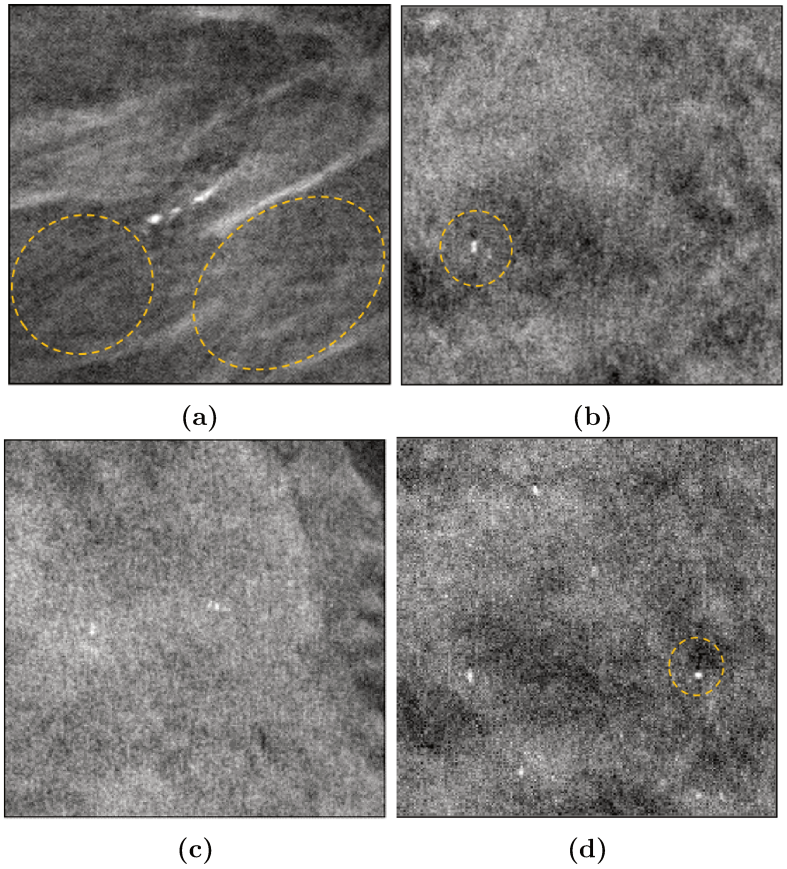

Figure 6.7: *The most observed artifacts in NRLS approach in the visual experiment study pooling over all the readers : (a) Replication artifacts. (b) Off-focal artifact. (c) Presence of noise. (d) Undershooting around microcalcifications.*

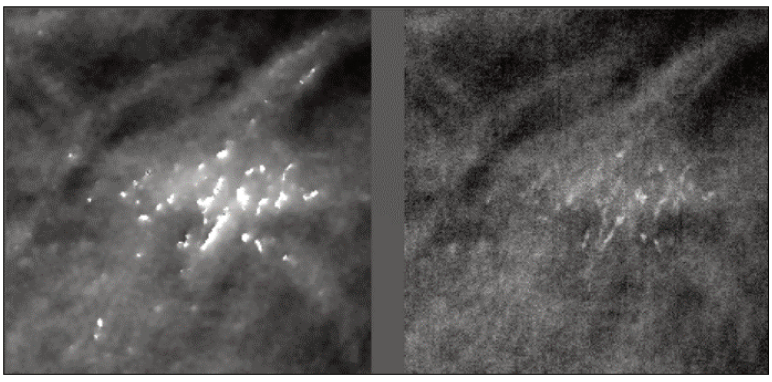

Figure 6.8: *Example of over-enhancement or non-realistic rendering of microcalcifications in dSATV. Left image: dSATV. Right image: NRLS*

By averaging over all the GE Healthcare image quality experts in mammography, we show the results in Figure 6.9. Pooling over all these experts,

the most frequent artifacts observed in NRLS and dSATV approaches are highlighted in Table 6.1. Furthermore, they have noted that the performance in specificity might decrease in dSTAV approach for some cases, due to the over-enhancement or the non-realistic rendering of microcalcifications, as illustrated in Figure 6.8. As a result, this may be considered as an artifact to be improved in dSATV approach, at least from a pure image quality point of view.

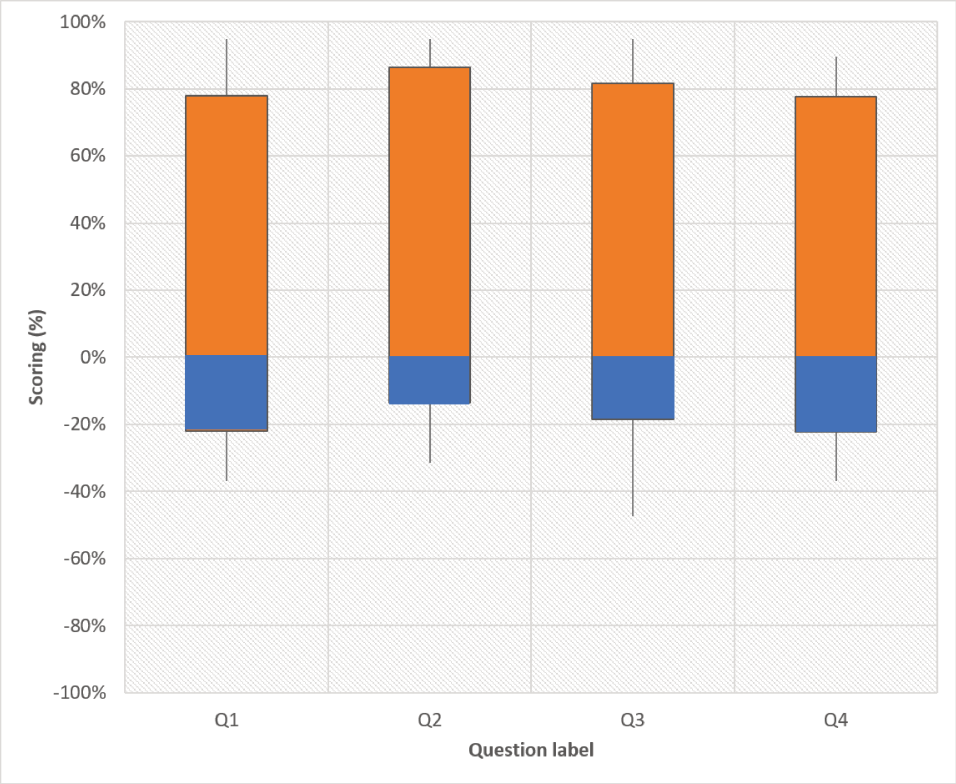

Figure 6.9: *Results of the visual experiment pooled over the GE Healthcare image quality experts in mammography: positive scoring is in favor of dSATV, negative scoring is in favor of NRLS.*

By averaging over all the radiologists, we present the results in Figure 6.10. We note that the most frequent artifacts detected by these experts in NRLS and dSATV approaches are highlighted in Table 6.1. It is worth mentioning that even though the specificity might be decreased for some cases in our proposed dSATV approach (e.g. Figure 6.8), the radiologists still prefer our proposed reconstruction since it enables a better conspicuity of microcalcifications in the context of breast cancer screening.

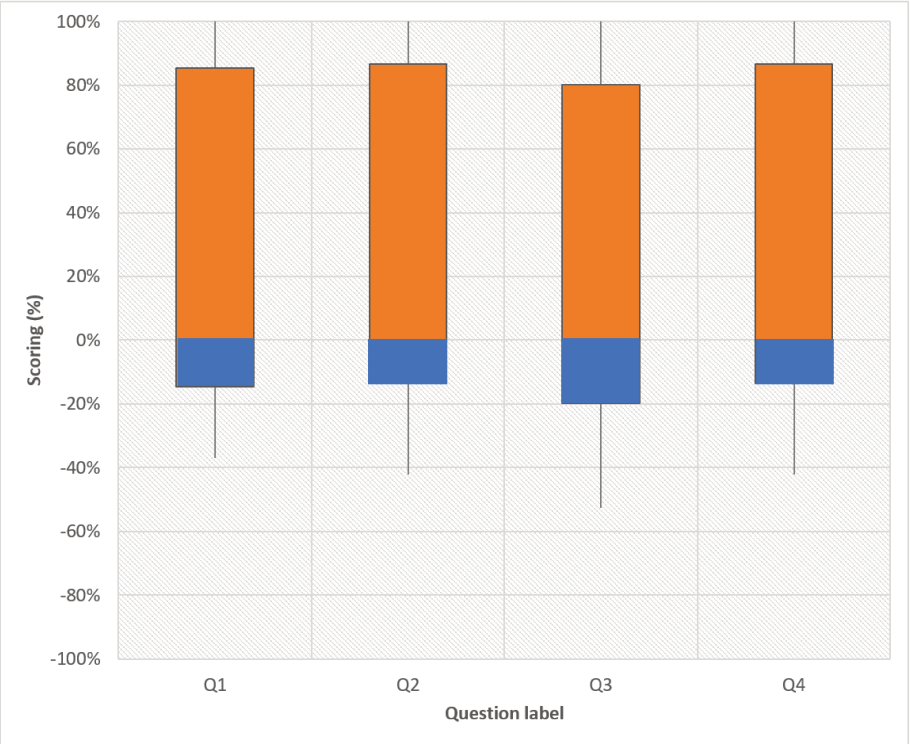

Figure 6.10: *Results of the visual experiment pooled over all the radiologists: positive scoring is in favor of dSATV, negative scoring is in favor of NRLS.*

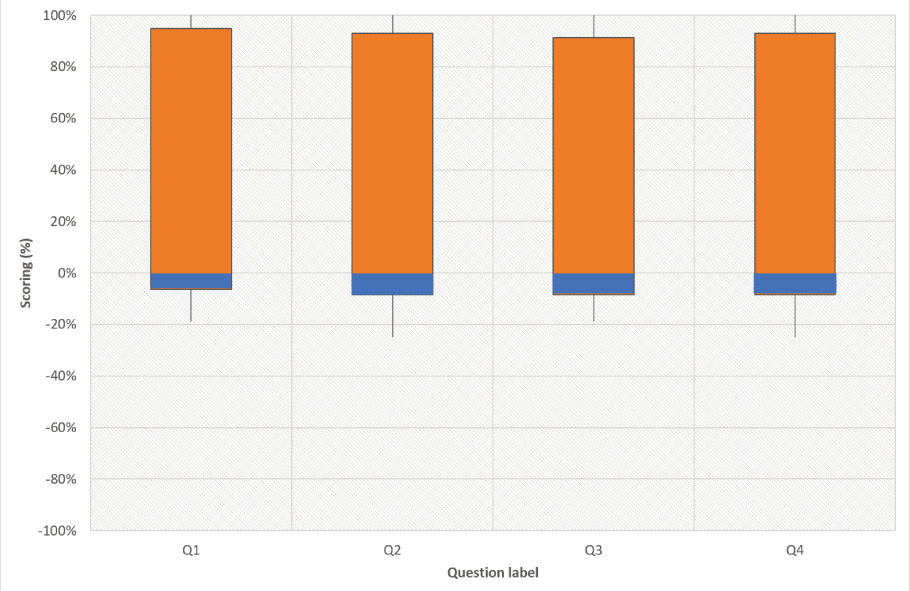

Figure 6.11: *Results of the visual experiment pooled over category "Expert": positive scoring is in favor of dSATV, negative scoring is in favor of NRLS.*

Herein, we further detail the results according to each category of radiologists. By averaging over category "Expert", we depict the results in Figure 6.11. The most frequent observed artifcats in NRLS and dSATV approaches are displayed in Table 6.1. We note that for this sub-group of readers, the radiologists have a high preference (and the highest of all sub-groups) for our proposed approach according to the four assessed criteria.

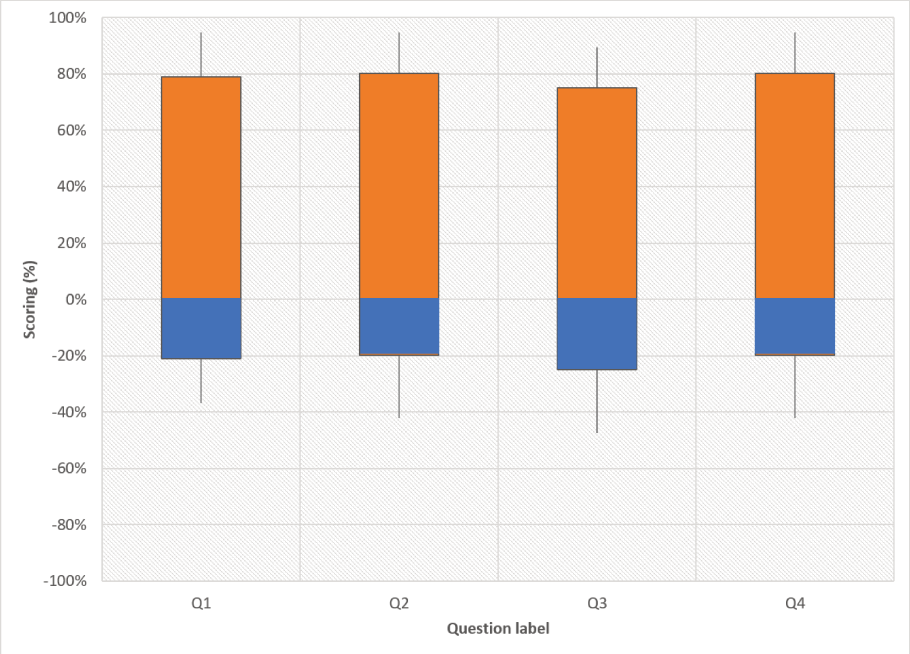

Figure 6.12: *Results of the visual experiment pooled over category "Advanced": positive scoring is in favor of dSATV, negative scoring is in favor of NRLS.*

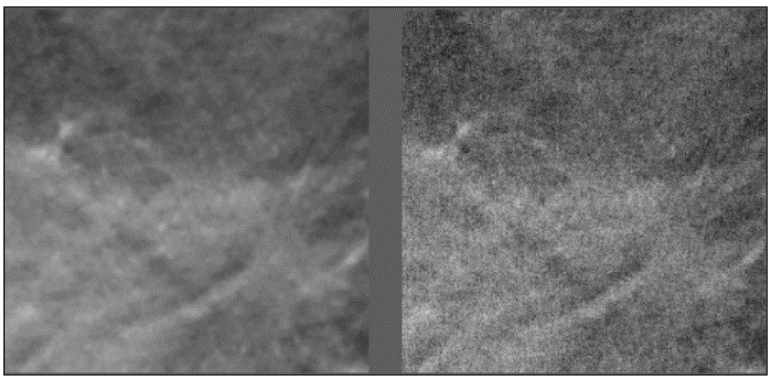

Figure 6.13: *Example of a slice with a perceived blurry background on dSATV. Left image: dSATV. Right image: NRLS*

By averaging over category "Advanced", the results are unveiled in Figure 6.12. In Table 6.1, we detail the most frequent artifacts detected in

NRLS and dSATV approaches, by this category of radiologists. We note that some radiologists of this sub-group of readers have found that the breast background reconstructed by our proposed approach may seem blurry for some cases when compared to NRLS approach, as illustrated in Figure 6.13. This is explained by the fact that some of these radiologists are accustomed to reading different breast background quality. Yet, they highlighted that this artifact does not disturb their clinical performance for the microcalcification detectability task. We note also that even though this category of radiologists has scored less high in favor of our dSATV approach when compared to "Expert" category, they still find our reconstruction helpful for the microcalcifications visibility.

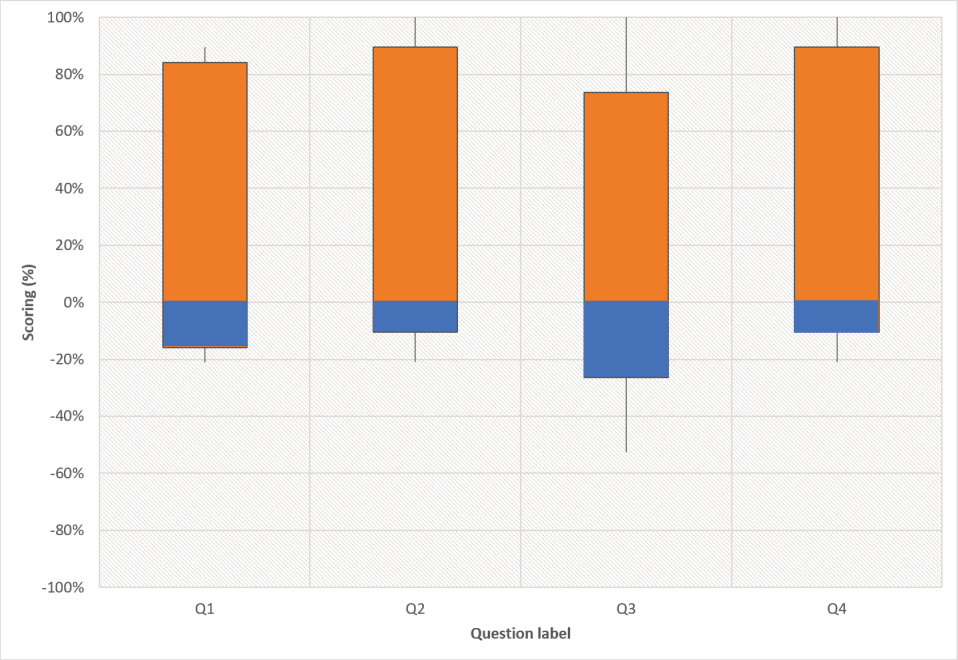

Figure 6.14: *Results of the visual experiment pooled over category "Junior": positive scoring is in favor of dSATV, negative scoring is in favor of NRLS.*

By averaging over category "Junior", we show the results in Figure 6.14. We highlight that for this category, the description of potential artifacts has scored the least when compared to the other categories. Note that one rater did find the NRLS solution noisy (Figure 6.7(c)) while the other one observed some undershooting around microcalcifications in our dSATV approach (Figure 6.6(a)) and presence of noise in NRLS approach (Figure 6.7(c)). This is presented in Table 6.1.

Table 6.1: *The most frequent observed artifacts in NRLS and dSATV approaches per group of readers*

Artifacts/ Group of readers		GE Healthcare	All radiologists	Expert radiologists	Advanced radiologists	Junior radiologists
dSATV approach	Some undershooting around the microcalcifications	×	×	×	×	×
	The presence of enhanced structures not identified as microcalcifications (false positives)	×				
NRLS approach	Replication artifacts	×				
	Presence of off-focal artifact	×	×	×		
	Presence of noise	×	×	×	×	×
	Some undershooting around the microcalcifications	×				

Finally, we observe that the different populations prefer our proposed dSATV approach over the NRLS solution. In average, the nine radiologists scored higher in microcalcification conspicuity, rendering of breast structures and overall visual preference criteria than the five GE Healthcare image quality experts in mammography. Yet, these five experts have scored slightly higher in presence of artifacts criterion. This analysis conveys two points:

- The radiologists may scrutinize the DBT reconstruction in favor of the clinical task in the context of breast cancer screening, which is the microcalcification visibility.

- GE Healthcare experts may be more sensitive towards the overall image quality in the DBT reconstruction.

6.3.2 Inter-reader agreements

It is important to verify the level of agreement between the readers in order to ensure the reliability of our study. Therefore, to assess the inter-reader agreement between the readers, we propose to compute the Gwet's AC1 agreement coefficient [66] for each asked question. This coefficient is defined as

$$\frac{p_a - p_e}{1 - p_e} \tag{6.1}$$

where the percent agreement p_a and the chance agreement probability p_e are defined as follows :

$$\begin{cases} p_a &= \dfrac{1}{n'} \displaystyle\sum_{i=1}^{n'} \sum_{k=1}^{q} \frac{r_{ik}\,(r_{ik}-1)}{r_i\,(r_i-1)}, \\ p_e &= \dfrac{1}{1-q} \displaystyle\sum_{k=1}^{q} \pi_k\,(1-\pi_k), \\ & \text{and} \quad \pi_k = \dfrac{1}{n} \displaystyle\sum_{i=1}^{n} \frac{r_{ik}}{r_i}. \end{cases} \tag{6.2}$$

In equation (6.2), q is the number of categories (in our case $q = 2$ since the readers should answer to the questions whether by "Right" or "Left"), r_{ik} is the count of readers who classified trial i into category k, r_i is the count of readers who rated trial i, n is the total count of trials, and n' the count of trials which were rated by two readers or more.
We highlight that we chose the Gwet's AC1 agreement coefficient to assess the inter-reader agreement in our study, since it has been shown to be resistant to Kappa paradox [66, 137, 58]. The latter studies show that the agreement measure based on the Kappa coefficient [43] can be low despite a high level of agreement between two readers, which is not the case for the Gwet's AC1 agreement [66].

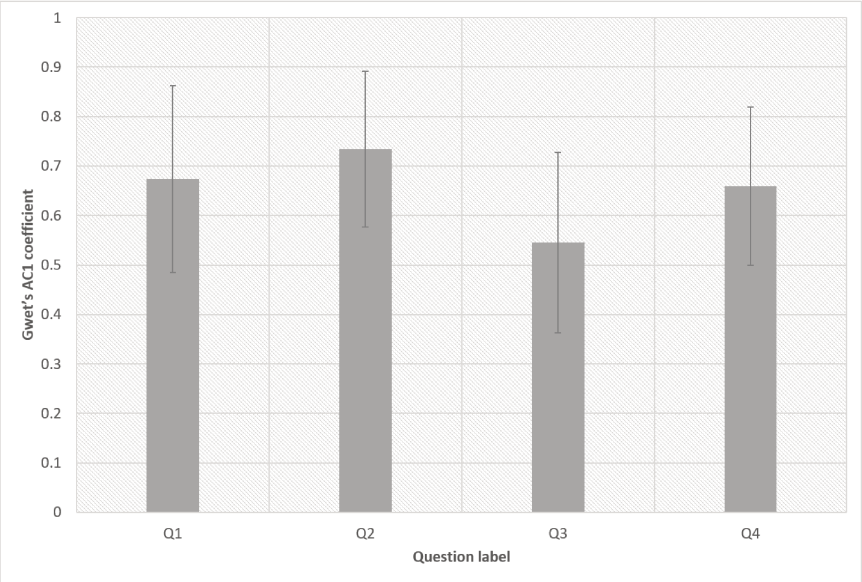

Figure 6.15: *Inter-reader agreement (Gwet's AC1 coefficients) between all the readers.*

We computed first the Gwet's AC1 agreement coefficient between all the readers for each question as displayed in Figure 6.15. The highest response

consensus is found for breast background restoration (with a substantial inter-reader agreement) [137] and the lowest one for the presence of potential artifacts (with a moderate inter-reader agreement). We notice also that the Gwet's AC1 coefficient indicates a substantial inter-reader agreement for microcalcification conspicuity and for the overall preference of the DBT reconstruction in favor of dSATV.

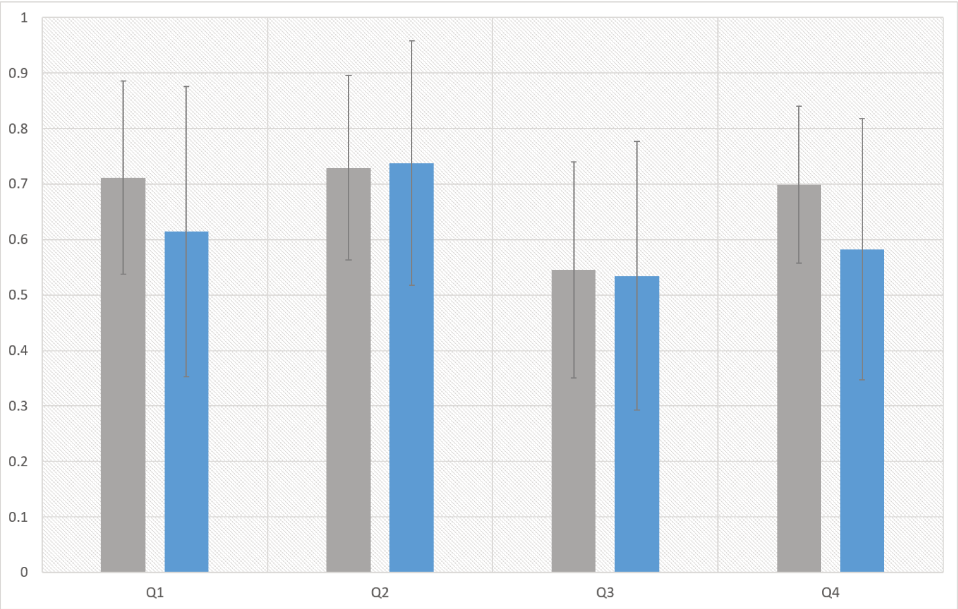

Figure 6.16: *Inter-reader agreement (Gwet's AC1 coefficients) between all the radiologists (in grey) and bewteen GE Healthcare image quality experts (in blue).*

To further understand the inter-reader agreement of each group of readers for each question, we compared the Gwet's AC1 agreement coefficient computed between the group of GE Healthcare image quality experts and between the group of all the radiologists, as illustrated in Figure 6.16. We highlight that the inter-reader agreement for microcalcification conspicuity and the overall preference for the DBT reconstruction in favor of dSATV scored higher between the radiologists than between GE Healthcare experts. Here again, this unveils that the group of radiologists consistently better appreciates a DBT reconstruction spotlighting the clinical task in the context of breast cancer screening, which is the microcalcification visibility. Moreover, the inter-reader agreement for breast background restoration is slightly higher between GE Healthcare image quality experts in mammography. This means that the GE Healthcare image quality experts are more sensitive to noise in images. Finally, the inter-reader agreement for the observed artifacts was comparable between the two reader populations.

We also compared the inter-reader agreement of each sub-group of radiol-

ogists for each question. Therefore, we computed the Gwet's AC1 agreement coefficient between the radiologists of category "Expert", between the radiologists of category "Advanced" and between the radiologists of category "Junior", as presented in Figure 6.17. First, we note that the inter-reader agreement over all the four criteria are the highest for the radiologists of category "Expert" when compared to the other group of readers. Furthermore, we highlight that the inter-reader agreement for breast background restoration and the overall preference of the DBT reconstruction in favor of dSATV scored lower in the radiologists of category "Advanced" when compared to the other sub-groups of radiologists. This may be explained by the fact that the radiologists of the "Advanced" category are accustomed to reading different breast background quality. Finally, the lowest response consensus is scored for the presence of potential artifacts by the radiologists' category "Junior". Herein, it is worth mentioning that in the latter category we have only two readers. This conveys that the inter-reader agreement would be more insightful and consistent, if we had more readers.

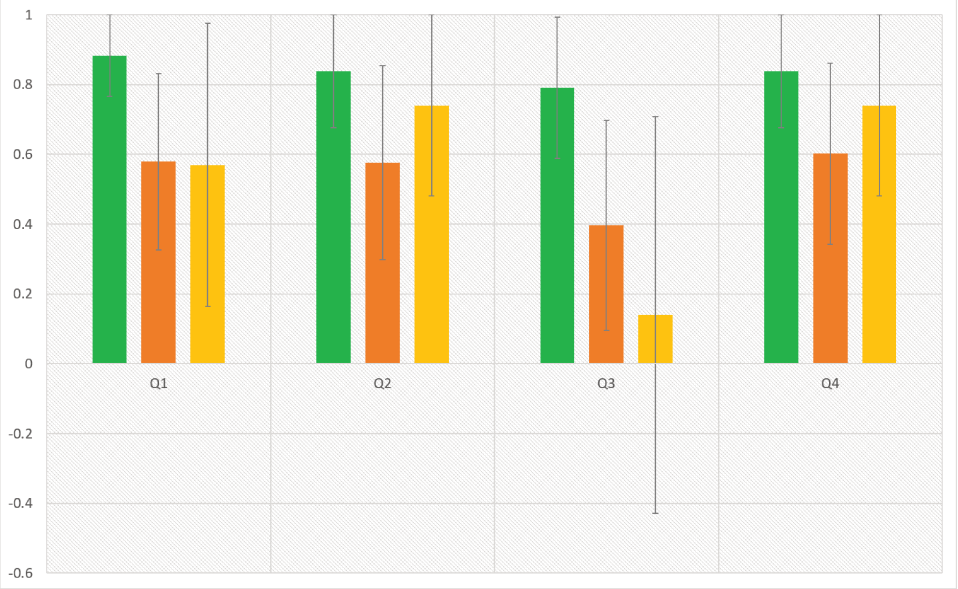

Figure 6.17: *Inter-reader agreement (Gwet's AC1 coefficients) between the radiologists of category "Expert" (in green), bewteen the radiologists of category "Advanced" (in orange) and between the radiologists of category "Junior" (in yellow).*

§ 6.4 Summary

We have conducted a visual experiment trial with fourteen readers including nine radiologists with different levels of expertise and five GE Healthcare

experts in mammography to quantitatively assess the contribution of our proposed approach dSATV. The results show the superiority of dSATV over the non-regularized least squares solution NRLS according to four criteria: microcalcification conspicuity, rendering of breast structures, presence of potential artifacts and overall visual preference. Furthermore, the results of the inter-reader agreement analysis tend to show that the radiologists may scrutinize the DBT reconstruction in favor of the clinical task, which is directly related to the conspicuity of microcalcifications, whereas, GE Healthcare experts may be more sensitive towards the overall image quality in the DBT reconstruction. Note that it might be worthwhile to perform this visual experiment in larger populations of readers, especially for the category "Junior" to better seize the potential prospects for dSATV improvements.

A future direction for further improvements should consider the different artifacts observed in our dSATV reconstruction approach, namely the undershooting around the microcalcifications, the presence of false positives and the non-realistic rendering of microcalcifications observed in some cases.

- Chapter 7 -

Conclusion

§ 7.1 Summary

The detectability of microcalcifications is a difficult problem in the context of DBT due to the characteristics of these lesions and the inherent geometric limitations of DBT. During this thesis, our main axes of research aimed at improving the microcalcification detectability in DBT volumes by focusing on the reconstruction algorithm. Accordingly, we have established a novel variational reconstruction framework in DBT tailored for enhancing the microcalcification detection performance and enabling a high-quality restoration of the background breast tissues.

In Chapter 2, we have focused on the clinical context of our research work. Therefore, we have introduced the breast cancer epidemiology and we have presented the imaging modalities currently used to detect suspicious lesions. Then, a special attention was dedicated to DBT which was introduced to reduce the limitations of FFDM, the current standard for breast cancer screening and diagnosis. An in-depth presentation of DBT was provided to explain its main features and benefits over FFDM and to discuss its performance in microcalcification detectability. As the latter performance has not yet reached consensus in the medical community, we investigated the reconstruction algorithm, which is a DBT key ingredient, to shed light on the core contributions of our research work.

In Chapter 3, we have explained the downsides of a typical workflow involving lesion detection task in DBT. Then, we have introduced our clinical-task based reconstruction approach. It integrates the radiological performance associated with a given clinical task to the reconstruction procedure. We proposed a novel a priori term in the DBT reconstruction combining regularized iterative DBT reconstruction and the task-based assessment strategy adopted in anthropomorphic model observers, namely CHO observer.

This approach aims at enhancing the detectability of microcalcifications in DBT reconstruction as the targeted clinical task.

Thus, we have proposed a new penalty function in our reconstruction method whose formulation takes its roots into the framework of CHO observer. Afterwards, we have presented the methodology to construct this novel function that acts as an enhancer for the microcalcification detectability. Finally, we have incorporated this detectability function in the proposed optimization approach. Experimental results have demonstrated the great interest of our method in terms of microcalcification enhancement compared with standard DBT reconstruction on both physical phantom and clinical data.

In Chapter 4, we have emphasized the need of investigating more sophisticated spatial regularization when reconstructing the DBT volume. In fact, breasts consist of several anatomical components with very different attenuation properties compared with the ones of the microcalcifications. Resorting to classical regularization approaches, such as total-variation (TV), is not enough to cope with such heterogeneity within the DBT images. In such challenging context, our contribution is to propose a new Spatially Adaptive TV (SATV) regularization function which responds to the need for heterogeneous spatial regularization in DBT reconstruction. In addition, it accounts for the different morphological contents of the breast. Henceforth, we provided an original discretization of the gradient field of the image that incorporates prior knowledge on the structural contents of the image. Thus, the SATV operator acts differently according to the sought local information around each voxel. Finally, we have derived our SATV regularization and incorporated it in the clinical-task based reconstruction approach for DBT, leading to the dSATV approach.

We have shown on both physical phantom and clinical data the great potential of our approach for preserving the shape of the enhanced microcalcifications while reducing the noisy appearance in background breast tissues and finally for improving the overall image quality. Thus, SATV regularizer constitutes a promising improvement with respect to state-of-the-art regularization methods.

In Chapter 5, we have investigated the application of Majorize-Minimize Memory Gradient (3MG) algorithm to our proposed dSATV approach. We have proposed two numerical improvements. First, we have considered a local majoration of the objective function in the neighbourhood of the current iterate. Indeed, this amounts to relaxing the majorizing assumption defined in MM approach. Second, we have suggested a new scheme to increase progressively the weight of the distance penalization function of each voxel of the volume to the plausible hypercube. Then, we have carried out a numerical comparison of the convergence speed of the proposed method with those of standard convex optimization algorithms.

The practical convergence profile demonstrates the potential interest of

the proposed numerical improvements of 3MG algorithm applied to our reconstruction framework. By combining the local majorant with the iteration-varying κ scheme, 3MG has the best convergence performance, when compared to several state-of-the-art minimization schemes.

In Chapter 6, we have carried out a visual experiment trial on fourteen raters involving nine radiologists with different levels of expertise and five GE Healthcare experts in mammography at the aim of quantitatively evaluate the contribution of our proposed dSATV approach. As a result, dSATV was shown to outperform the non-regularized least squares solution NRLS based on four criteria: microcalcification conspicuity, rendering of breast structures, presence of potential artifacts and overall visual preference. In addition, we have assessed the inter-reader agreement between the readers by computing the Gwet's AC1 coefficient. The results demonstrated that the radiologists may examinate the DBT reconstruction in favor of the clinical task in the context of breast cancer screening, which is directly linked to microcalcification conspicuity, while, GE Healthcare experts may be more sensitive towards the overall image quality in the DBT reconstruction.

In the next section, we suggest several extensions of the aforementioned contributions that could be investigated for future works.

§ 7.2 Perspectives

The detectability function introduced in Chapter 3 could be further improved as proposed hereafter.

Deploy accelerated versions of Parallel Forward-Backward based Primal-Dual Algorithm

The formulation of the parallel Forward-Backward Primal-Dual Algorithm in Section 3.3.2 requires the computation of the Lipschitz constant of the differentiable part of the loss function. From a practical point of view, this turns out to be cumbersome in large-scale simulation scenarios. It would be therefore interesting to integrate accelerated versions of primal-dual algorithm proposed in [79, 45].

Investigate the False positives in the developed detection map

In our strategy proposed to construct the detection map in Section 3.3.2, we apply on the TV-based solution obtained by Algorithm 2 successive opening operators. The aim was to detect the voxels comprising structures suspected to be microcalcifications whose size lies in a specific range. Since the selection criterion is solely based on the size, this method keeps structures not identified as microcalcifications

(false positives) that share the same size as microcalcifications. As a consequence, it might be worthwhile to investigate more sophisticated morphological operators that encompass the different characteristics of microcalcification in terms of size, shape, contrast and distribution [42, 141, 31, 95] for a better distinction between true postives (microcalcifications) and false positives.

Study the application of an improved 3D model observer to better match human observer performance

The channelization mechanism in the CHO model adopted in Section 3.4.1 does not take into consideration the correlation between the slices of the input volume. It might be a good choice to investigate the extensions of CHO model in [112] which were proposed to realistically model the stack review mode of volume slices in DBT. In addition, different spatial and frequency channel models were proposed in literature to model characteristics of the human visual system in certain conditions. It might be of interest to compare Laguerre-Gauss application with the frequently applied channels such as the Gabor channels [145] and the square channels [117, 100]. Furthermore, our used model observer does not encounter the viewing distance and the scrolling speed of the human observer when reading a stack of images. These aspects could be integrated by using a spatio-temporel contrast-sensitivity function enabling better matches with human observer performance [10]. Finally, an extension of the white Gaussian noise model in equation (3.2) to more complex models might be worthwhile to better handle the non-Gaussian noise in the clinical images.

We propose the following potential improvements and future leads related to our SATV regularization studied in Chapter 4.

Consider an automatic setting of SATV parameters

One limitation of the proposed SATV regularization is that we need to fix its parameters for each volume. Moreover, to construct the adequate weight parameters in new reconstructed equation (4.8) for each volume, we need to search for an optimal value of ν parameter, that preserves the geometric shape of the detected microcalcifications, whereby conducting dSATV reconstructions for the assessed values of ν. From a practical point of view, this methodology should be improved by adopting an automatic setting of ν parameter given the location of microcalcifications.

Extend the application of SATV regularization

Apart from microcalcifications, the breast may contain other lesions as detailed in Section 2.2.3. Thus, SATV function could be extended to

spatially adapt the regularization providing sharper and more robust shape preservation of the different components of the breast. We also highlight that SATV regularization could be applied to other image processing applications (e.g., astronomy) that involve both localized objects and homogeneous areas.

Building on 3MG algorithm applied to our proposed DBT reconstruction in Chapter 5, we suggest the following research directions.

Study the convergence proof of the proposed numerical improvements of 3MG algorithm

The proposed numerical improvements in Section 5.3 have numerically demonstrated their efficiency in boosting the convergence speed of 3MG algorithm. From a theoretical perspective, a rigorous theoretical proof should be conducted to study the convergence of the proposed improved variant of 3MG algorithm and further extend its application.

Explore stopping criteria strategy for DBT reconstruction algorithm

We have observed that the global image quality of the reconstructed DBT volume does not change after a certain number of iterations. From a practical point of view, we can explore more adapted stopping criteria schemes, such as early stopping rules studied in [91, 115], based on defining the number of iterations required to obtain a satisfactory approximation to the solution. One possible starting point is to conduct a psychovisual experiment to determine the required number of iterations.

Deep unfold 3MG algorithm

Several recent works have investigated the combination between deep learning (DL) and iterative reconstruction approaches [17, 2, 130]. The advantage of these methods is that they provide a better convergence speed when compared to standard optimization algorithms and interpretable models in contrast to "Black-box" end-to-end learning. Therefore, we may explore this approach by deep unfolding the fastest variant of 3MG algorithm to benefit from a potential gain in terms of convergence speed as well as a better distinction between enhancing true positives versus false postives in volumes through a dedicated training dataset. In addition, a suitable GPU implementation could be beneficial to improve the efficiency of the implemented algorithm.

Finally, we suggest a possible following future direction related to artefacts reduction in DBT reconstruction.

Deep learning projection interpolation

With the aim of reducing replication artefacts in DBT reconstruction, we have investigated projection interpolation using deep learning (DL) approach. Preliminary results conducted on both synthetic and clinical data showed the potential interest of the proposed approach when compared to linear interpolation. Indeed, generating more projections under the standard DBT angular aperture using the proposed DL-based approach reduced the intensity of replication artefacts in the reconstructed volume. Then, it would be worthwhile to further investigate this approach considering the following leads: training the network on a larger dataset which comprises higher variability in terms of texture and lesions, designing a DL architecture which better reflects the DBT geometry and finally assess a larger angular range through a dedicated training data set, as studied in the CT scenario [33].

List of Figures

List of Tables

List of Algorithms

Bibliography

[1] R. Abergel and L. Moisan. The shannon total variation. *Journal of Mathematical Imaging and Vision*, 59(2):341–370, 2017. 59

[2] J. Adler and O. Öktem. Learned primal-dual reconstruction. *IEEE transactions on medical imaging*, 37(6):1322–1332, 2018. 111

[3] J. Adler, S. Lunz, O. Verdier, C. B. Schönlieb, and O. Öktem. Task adapted reconstruction for inverse problems. *arXiv preprint arXiv:1809.00948*, 2018. 33

[4] M. Allain, J. Idier, and Y. Goussard. On global and local convergence of half-quadratic algorithms. *IEEE Transactions on Image Processing*, 15(5):1130–1142, 2006. 80

[5] A. Andersen and A. Kak. Simultaneous algebraic reconstruction technique (sart): a superior implementation of the art algorithm. *Ultrasonic imaging*, 6(1):81–94, 1984. 25

[6] S. Astley, E. Harkness, J. Sergeant, J. Warwick, P. Stavrinos, R. Warren, M. Wilson, U. Beetles, S. Gadde, Y. Lim, et al. A comparison of five methods of measuring mammographic density: a case-control study. *Breast Cancer Research*, 20(1):10, 2018. 15

[7] A. Athanasiou, A. Tardivon, L. Ollivier, F. Thibault, C. El Khoury, and S. Neuenschwander. How to optimize breast ultrasound. *European journal of radiology*, 69(1):6–13, 2009. 10

[8] J. Aujol. Some first-order algorithms for total variation based image restoration. *Journal of Mathematical Imaging and Vision*, 34(3):307–327, 2009. 59

[9] A. Avanaki, K. Espig, C. Marchessoux, E. Krupinski, P. Bakic, T. Kimpe, and A. Maidment. Integration of spatio-temporal contrast sensitivity with a multi-slice channelized hotelling observer. In *Medical*

Imaging 2013: Image Perception, Observer Performance, and Technology Assessment, volume 8673, page 86730H. International Society for Optics and Photonics, 2013. 18

[10] A. Avanaki, K. Espig, A. Maidment, C. Marchessoux, P. Bakic, and T. Kimpe. Development and evaluation of a 3d model observer with nonlinear spatiotemporal contrast sensitivity. In *Medical Imaging 2014: Image Perception, Observer Performance, and Technology Assessment*, volume 9037, page 90370X. International Society for Optics and Photonics, 2014. 110

[11] M. Bae, W. Moon, J. Chang, H. Koo, W. Kim, N. Cho, A. Yi, B. La Yun, S. Lee, M. Kim, et al. Breast cancer detected with screening us: reasons for nondetection at mammography. *Radiology*, 270(2): 369–377, 2014. 10

[12] H. Barrett, J. Yao, J. Rollandt, and K. Myerst. Model observers for assessment of image quality. *Proceedings of the National Academy of Sciences*, 90(November):9758–9765, 1993. 31, 35

[13] A. Beck and M. Teboulle. A fast iterative shrinkage-thresholding algorithm for linear inverse problems. *SIAM journal on imaging sciences*, 2(1):183–202, 2009. 84

[14] W. Berg, L. Gutierrez, M. NessAiver, W. Carter, M. Bhargavan, R. Lewis, and O. Ioffe. Diagnostic accuracy of mammography, clinical examination, us, and mr imaging in preoperative assessment of breast cancer. *radiology*, 233(3):830–849, 2004. 10

[15] W. Berg, J. Blume, J. Cormack, E. Mendelson, D. Lehrer, M. Böhm-Vélez, E. Pisano, R. Jong, W. Evans, M. Morton, et al. Combined screening with ultrasound and mammography vs mammography alone in women at elevated risk of breast cancer. *Jama*, 299(18):2151–2163, 2008. 10

[16] C. Berger, T. Geraud, R. Levillain, N. Widynski, A. Baillard, and E. Bertin. Effective Component Tree Computation with Application to Pattern Recognition in Astronomical Imaging. In *Proceeding of IEEE International Conference on Image Processing (ICIP 2007)*, volume 4, pages 41–44, San Antonio, TX, 16-19 September 2007. doi: 10.1109/ICIP.2007.4379949. 41

[17] C. Bertocchi, E. Chouzenoux, M. C. Corbineau, J. C. Pesquet, and M. Prato. Deep unfolding of a proximal interior point method for image restoration. *Inverse Problems*, 36(3):034005, 2020. 111

[18] D. P. Bertsekas. *Nonlinear Programming*. Qing hua da xue chu ban she, 2018. 78

[19] S. Biton and G. Gilboa. Adaptive anisotropic total variation-a nonlinear spectral analysis. *arXiv preprint arXiv:1811.11281*, 2018. 59

[20] P. Blomgren, T. F. Chan, P. Mulet, and C. Wong. Total variation image restoration: numerical methods and extensions. In *Proceedings of IEEE International Conference on Image Processing (ICIP 1997)*, volume 3, pages 384–387. IEEE, 26-29 October 1997. 59

[21] S. Boyd, N. Parikh, E. Chu, B. Peleato, and J. Eckstein. Distributed optimization and statistical learning via the alternating direction method of multipliers. *Foundations and Trends® in Machine learning*, 3(1):1–122, 2011. 64

[22] K. Bredies, K. Kunisch, and T. Pock. Total generalized variation. *SIAM Journal on Imaging Sciences*, 3(3):492–526, 2010. 62

[23] W. Buchberger, A. Niehoff, P. Obrist, P. DeKoekkoek-Doll, and M. Dünser. Clinically and mammographically occult breast lesions: detection and classification with high-resolution sonography. In *Seminars in Ultrasound, CT and MRI*, volume 21, pages 325–336. Elsevier, 2000. 16

[24] S.-Q. Cai, J.-X. Yan, Q.-S. Chen, M.-L. Huang, and D.-L. Cai. Significance and application of digital breast tomosynthesis for the bi-rads classification of breast cancer. *Asian Pac J Cancer Prev*, 16:4109–4114, 2015. 18

[25] P. H. Calamai and J. J. Moré. Projected gradient methods for linearly constrained problems. 39(1):93–116, 1987. 83

[26] X. Castells, I. Torá-Rocamora, M. Posso, M. Román, M. Vernet-Tomas, A. Rodríguez-Arana, L. Domingo, C. Vidal, M. Baré, J. Ferrer, et al. Risk of breast cancer in women with false-positive results according to mammographic features. *Radiology*, 280(2):379–386, 2016. 17

[27] A. Chambolle and C. Dossal. On the convergence of the iterates of " fista". *Journal of Optimization Theory and Applications*, 166(3):25, 2015. 83, 84

[28] A. Chambolle, S. Levine, and B. Lucier. An upwind finite-difference method for total variation–based image smoothing. *SIAM Journal on Imaging Sciences*, 4(1):277–299, 2011. 59

[29] T. Chan, A. Marquina, and P. Mulet. High-order total variation-based image restoration. *SIAM Journal on Scientific Computing*, 22(2):503–516, 2000. 59

[30] T. Chan, S. Esedoglu, and F. Park. Image decomposition combining staircase reduction and texture extraction. *Journal of Visual Communication and Image Representation*, 18(6):464–486, 2007. 59

[31] Z. Chen, H. Strange, A. Oliver, E. Denton, C. Boggis, and R. Zwiggelaar. Topological modeling and classification of mammographic microcalcification clusters. *IEEE transactions on biomedical engineering*, 62 (4):1203–1214, 2014. 110

[32] G. Chierchia, N. Pustelnik, B. Pesquet-Popescu, and J. Pesquet. A nonlocal structure tensor-based approach for multicomponent image recovery problems. *IEEE transactions on Image Processing*, 23(12): 5531–5544, 2014. 59, 62

[33] J. Choi, B. Dong, and X. Zhang. Limited tomography reconstruction via tight frame and sinogram extrapolation. *arXiv preprint arXiv:1602.07049*, 2016. 112

[34] J. Choi, B.-K. Han, E. Ko, E. Ko, S. Hahn, J. Shin, and M. Kim. Comparison between two-dimensional synthetic mammography reconstructed from digital breast tomosynthesis and full-field digital mammography for the detection of t1 breast cancer. *European radiology*, 26(8):2538–2546, 2016. 22

[35] E. Chouzenoux and J.-C. Pesquet. Convergence rate analysis of the majorize-minimize subspace algorithm. 23(9):1284–1288, Sep. 2016. 42, 79

[36] E. Chouzenoux and J. C. Pesquet. Convergence rate analysis of the majorize–minimize subspace algorithm. *IEEE Signal Processing Letters*, 23(9):1284–1288, 2016. 77

[37] E. Chouzenoux and J. C. Pesquet. A stochastic majorize-minimize subspace algorithm for online penalized least squares estimation. 65 (18):4770–4783, 2017. 77

[38] E. Chouzenoux, J. Idier, and S. Moussaoui. A majorize–minimize strategy for subspace optimization applied to image restoration. *IEEE Transactions on Image Processing*, 20(6):1517–1528, 2010. 78

[39] E. Chouzenoux, A. Jezierska, J. C. Pesquet, and H. Talbot. A majorize-minimize subspace approach for $\ell_2 - \ell_0$ image regularization. *SIAM Journal on Imaging Sciences*, 6(1):563–591, 2013. 64, 77, 79, 80, 81

[40] E. Chouzenoux, F. Zolyniak, E. Gouillart, and H. Talbot. A majorize-minimize memory gradient algorithm applied to x-ray tomography.

In *2013 IEEE International Conference on Image Processing*, pages 1011–1015. IEEE, 2013. 64, 79

[41] I. Christoyianni, A. Koutras, E. Dermatas, and G. Kokkinakis. Computer aided diagnosis of breast cancer in digitized mammograms. *Computerized Medical Imaging and Graphics*, 26(5):309 – 319, 2002. ISSN 0895-6111. doi: https://doi.org/10.1016/S0895-6111(02)00031-9. URL http://www.sciencedirect.com/science/article/pii/S0895611102000319. 38

[42] M. Ciecholewski. Microcalcification segmentation from mammograms: A morphological approach. *Journal of digital imaging*, 30(2):172–184, 2017. 110

[43] J. Cohen. A coefficient of agreement for nominal scales. *Educational and psychological measurement*, 20(1):37–46, 1960. 103

[44] P. Combettes and J. Pesquet. Proximal splitting methods in signal processing. In *Fixed-point algorithms for inverse problems in science and engineering*, pages 185–212. Springer, 2011. 64

[45] P. L. Combettes and J.-C. Pesquet. Fixed point strategies in data science. *arXiv preprint arXiv:2008.02260*, 2020. 64, 109

[46] L. Condat. Discrete total variation: New definition and minimization. *SIAM Journal on Imaging Sciences*, 10(3):1258–1290, 2017. 59, 62

[47] M. C. Corbineau, E. Chouzenoux, and J. C. Pesquet. Geometry-texture decomposition/reconstruction using a proximal interior point algorithm. In *2018 IEEE 10th Sensor Array and Multichannel Signal Processing Workshop (SAM)*, pages 435–439. IEEE, 2018. 59

[48] P. Crystal, S. Strano, S. Shcharynski, and M. Koretz. Using sonography to screen women with mammographically dense breasts. *American Journal of Roentgenology*, 181(1):177–182, 2003. 10

[49] H. Dang, J. Stayman, J. Xu, W. Zbijewski, A. Sisniega, M. Mow, X. Wang, D. Foos, N. Aygun, V. Koliatsos, and J. Siewerdsen. Task-based statistical image reconstruction for high-quality cone-beam ct. *Physics in Medicine & Biology*, 62(22):8693–8719, 2017. URL http://stacks.iop.org/0031-9155/62/i=22/a=8693. 28

[50] A. R. De Pierro. A modified expectation maximization algorithm for penalized likelihood estimation in emission tomography. *IEEE transactions on medical imaging*, 14(1):132–137, 1995. 77

[51] A. H. Delaney and Y. Bresler. Globally convergent edge-preserving regularized reconstruction: an application to limited-angle tomography. *IEEE Transactions on Image Processing*, 7(2):204–221, 1998. 80

[52] J. E. Dennis Jr. and R. E. Welsch. Techniques for nonlinear least squares and robust regression. *Communications in Statistics-simulation and Computation*, 7(4):345–359, 1978. 61

[53] S. Destounis, A. Arieno, and R. Morgan. Preliminary clinical experience with digital breast tomosynthesis in the visualization of breast microcalcifications. *Journal of clinical imaging science*, 3, 2013. 21

[54] J. T. Dobbins III. and D. Godfrey. Digital x-ray tomosynthesis: current state of the art and clinical potential. *Physics in medicine & biology*, 48(19):R65, 2003. 24

[55] M. Dustler, P. Timberg, A. Tingberg, and S. Zackrisson. Image quality of thick average intensity pixel slabs using statistical artifact reduction in breast tomosynthesis. In *International Workshop on Digital Mammography*, pages 544–549. Springer, 2014. 21

[56] H. Erdogan and J. A. Fessler. Ordered subsets algorithms for transmission tomography. *Physics in Medicine & Biology*, 44(11):2835, 1999. 77

[57] A. Evans, R. Trimboli, A. Athanasiou, C. Balleyguier, P. Baltzer, U. Bick, J. Herrero, P. Clauser, C. Colin, E. Cornford, et al. Breast ultrasound: recommendations for information to women and referring physicians by the european society of breast imaging. *Insights into imaging*, 9(4):449–461, 2018. 10

[58] A. R. Feinstein and D. V. Cicchetti. High agreement but low kappa: I. the problems of two paradoxes. *Journal of clinical epidemiology*, 43 (6):543–549, 1990. 103

[59] J. Ferlay, I. Soerjomataram, M. Ervik, R. Dikshit, S. Eser, C. Mathers, M. Rebelo, D. Parkin, D. Forman, and F. Bray. Globocan 2012 v1. 0, cancer incidence and mortality worldwide: Iarc cancerbase no. 11. *Lyon, France: International agency for research on cancer*, 2016, 2013. 8

[60] R. Fisher. *Statistical Methods for Research Workers*. Number V. Genesis Publishing Pvt Ltd, 1925. 36

[61] A. Florescu, E. Chouzenoux, J.-C. Pesquet, P. Ciuciu, and S. Ciochina. A majorize-minimize memory gradient method for complex-valued inverse problem. *Signal Processing*, 103:285–295, Oct. 2014. Special

issue on Image Restoration and Enhancement: Recent Advances and Applications. 77

[62] A. Florescu, E. Chouzenoux, J. C. Pesquet, P. Ciuciu, and S. Ciochina. A majorize-minimize memory gradient method for complex-valued inverse problems. *Signal Processing*, 103:285–295, 2014. 79

[63] P. Freer. Mammographic breast density: impact on breast cancer risk and implications for screening. *Radiographics*, 35(2):302–315, 2015. 16

[64] M. Ghoncheh, A. Mohammadian-Hafshejani, and H. Salehiniya. Incidence and mortality of breast cancer and their relationship to development in asia. *Asian Pacific Journal of Cancer Prevention*, 16(14): 6081–6087, 2015. 8

[65] H. Greenwood, K. Dodelzon, and J. Katzen. Impact of advancing technology on diagnosis and treatment of breast cancer. *Surgical Clinics*, 98(4):703–724, 2018. 8

[66] K. L. Gwet. *Handbook of inter-rater reliability: The definitive guide to measuring the extent of agreement among raters*. Advanced Analytics, LLC, 2014. 102, 103

[67] P. Hansen. *Discrete inverse problems: insight and algorithms*, volume 7. Siam, 2010. ISBN 0898716969, 9780898716962. 27, 28

[68] P. Henrot, A. Leroux, C. Barlier, and P. Génin. Breast microcalcifications: the lesions in anatomical pathology. *Diagnostic and interventional imaging*, 95(2):141–152, 2014. 35

[69] R. Hooley, M. Durand, and L. Philpotts. Advances in digital breast tomosynthesis. *American Journal of Roentgenology*, 208(2):256–266, 2017. 22

[70] G. Hortobagyi, J. De La Garza Salazar, K. Pritchard, D. Amadori, R. Haidinger, C. Hudis, H. Khaled, M.-C. Liu, M. Martin, M. Namer, et al. The global breast cancer burden: variations in epidemiology and survival. *Clinical breast cancer*, 6(5):391–401, 2005. 8

[71] Y.-H. Hu, B. Zhao, and W. Zhao. Image artifacts in digital breast tomosynthesis: Investigation of the effects of system geometry and reconstruction parameters using a linear system approach. *Medical physics*, 35(12):5242–5252, 2008. 20

[72] D. Ikeda and K. Miyake. *Breast Imaging: The Requisites E-Book*. Elsevier Health Sciences, 2016. 12

[73] M. W. Jacobson and J. A. Fessler. An expanded theoretical treatment of iteration-dependent majorize-minimize algorithms. 16(10): 2411–2422, Oct. 2007. 64

[74] M. Jochelson, K. Pinker, D. Dershaw, M. Hughes, G. Gibbons, K. Rahbar, M. Robson, D. Mangino, D. Goldman, C. Moskowitz, et al. Comparison of screening cedm and mri for women at increased risk for breast cancer: a pilot study. *European journal of radiology*, 97:37–43, 2017. 11

[75] A. Kak, M. Slaney, and G. Wang. Principles of computerized tomographic imaging. *Medical Physics*, 29(1):107–107, 2002. 24

[76] Y. Kim, K.-Y. Yoo, and M. Goodm. Differences in incidence, mortality and survival of breast cancer by regions and countries in asia and contributing factors. *Asian Pac J Cancer Prev*, 16(7):2857–70, 2015. 8

[77] T. Kolb, J. Lichy, and J. Newhouse. Comparison of the performance of screening mammography, physical examination, and breast us and evaluation of factors that influence them: an analysis of 27,825 patient evaluations. *Radiology*, 225(1):165–175, 2002. 10, 16

[78] N. Komodakis and J. Pesquet. Playing with Duality : An Overview of Recent Primal-Dual Approaches for Solving Large-Scale Optimization Problems. *IEEE Signal Processing Magazine*, 32(6):31 – 54, 2014. 38, 39, 64

[79] N. Komodakis and J. Pesquet. Playing with duality: An overview of recent primal? dual approaches for solving large-scale optimization problems. *IEEE Signal Processing Magazine*, 32(6):31–54, 2015. 109

[80] D. Kopans. Interpreting the mammogram. *Breast imaging. 3rd ed. Philadelphia, Pa: Lippincott Williams & Wilkins*, pages 365–479, 2007. 9

[81] D. Kopans, S. Gavenonis, E. Halpern, and R. Moore. Calcifications in the breast and digital breast tomosynthesis. *The breast journal*, 17 (6):638–644, 2011. 21

[82] C. Kuhl, P. Mielcareck, S. Klaschik, C. Leutner, E. Wardelmann, J. Gieseke, and H. Schild. Dynamic breast mr imaging: are signal intensity time course data useful for differential diagnosis of enhancing lesions? *Radiology*, 211(1):101–110, 1999. 11

[83] J. Lewin, P. Isaacs, V. Vance, and F. Larke. Dual-energy contrast-enhanced digital subtraction mammography: feasibility. *Radiology*, 229(1):261–268, 2003. 11

[84] Z. Li, A. Desolneux, S. Muller, P. Milioni de Carvalho, and A. Carton. Comparison of microcalcification detectability in FFDM and DBT using a virtual clinical trial. In *Proceeding SPIE Medical Imaging*, volume 10577, Houston, Texas, February 2018. doi: 10.1117/12.2293619. URL https://doi.org/10.1117/12.2293619. 43

[85] F. Liao and S. Shao. An image denoising fast algorithm for weighted total variation. In *Proceedings of the 2nd International Conference on Intelligent Information Processing*, page 16. ACM, July 2017. 59

[86] C. Louchet and L. Moisan. Total variation denoising using posterior expectation. In *Proceedings of the 16th IEEE European Signal Processing Conference (EUSIPCO2008)*, pages 1–5. IEEE, 25-29 August 2008. 59

[87] Y. Lu, H.-P. Chan, J. A. Fessler, L. Hadjiiski, J. Wei, and M. M. Goodsitt. Adaptive diffusion regularization for enhancement of microcalcifications in digital breast tomosynthesis (dbt) reconstruction. In *Medical Imaging 2011: Physics of Medical Imaging*, volume 7961, page 796117. International Society for Optics and Photonics, 2011. 28

[88] F. Luo, W. Li, W. Tu, and W. Wu. Adaptive weighted total variation minimization based alternating direction method of multipliers for limited angle ct reconstruction. *IEEE Access*, 6:64225–64236, 2018. 59

[89] R. Mann, N. Cho, and L. Moy. Breast mri: State of the art. *Radiology*, 292(3):520–536, 2019. 11

[90] S. Mansour, L. Adel, O. Mokhtar, and O. Omar. Comparative study between breast tomosynthesis and classic digital mammography in the evaluation of different breast lesions. *The Egyptian Journal of Radiology and Nuclear Medicine*, 45(3):1053–1061, 2014. 18

[91] S. Matet, L. Rosasco, S. Villa, and B. Vu. Don't relax: early stopping for convex regularization. *arXiv preprint arXiv:1707.05422*, 2017. 111

[92] K. McPherson, C. Steel, and J. Dixon. Abc of breast diseases: breast cancer—epidemiology, risk factors, and genetics. *BMJ: British Medical Journal*, 321(7261):624, 2000. 8

[93] O. Merveille, O. Miraucourt, S. Salmon, N. Passat, and H. Talbot. A variational model for thin structure segmentation based on a directional regularization. In *Proceedings of IEEE International Conference on Image Processing (ICIP 2016)*, pages 4324–4328. IEEE, 25-28 September 2016. 59

[94] E. Metin, Y. Isa, K. Mustafa, and A. Aydin. An iterative tomosynthesis reconstruction using total variation combined with nonlocal means filtering. *BioMedical Engineering OnLine*, 13(1):65, May 2014. ISSN 1475-925X. doi: 10.1186/1475-925X-13-65. URL https://doi.org/10.1186/1475-925X-13-65. 59

[95] F. Meyer, C. Vachier, A. Oliveras, and P. Salembier. Morphological tools for segmentation: connected filters and watersheds. In *Annales des télécommunications*, volume 52, pages 367–379. Springer, 1997. 110

[96] M. Michell. Breast screening review—a radiologist's perspective. *The British journal of radiology*, 85(1015):845–847, 2012. 17

[97] M. Michell, A. Iqbal, R. Wasan, D. Evans, C. Peacock, C. Lawinski, A. Douiri, R. Wilson, and P. Whelehan. A comparison of the accuracy of film-screen mammography, full-field digital mammography, and digital breast tomosynthesis. *Clinical radiology*, 67(10):976–981, 2012. 21

[98] A. Miele and J. W. Cantrell. Study on a memory gradient method for the minimization of functions. *Journal of Optimization Theory and Applications*, 3(6):459–470, 1969. 78

[99] Z. Momenimovahed and H. Salehiniya. Epidemiological characteristics of and risk factors for breast cancer in the world. *Breast Cancer: Targets and Therapy*, 11:151, 2019. 8

[100] K. Myers and H. Barrett. Addition of a channel mechanism to the ideal-observer model. *JOSA A*, 4(12):2447–2457, 1987. 35, 37, 110

[101] L. Najman and H. Talbot. *Mathematical morphology: from theory to applications*. John Wiley & Sons, 2013. 40

[102] F. Natterer and F. Wübbeling. *Mathematical methods in image reconstruction*, volume 5. Siam, 2001. 24

[103] L. Niklason, B. Christian, L. Niklason, D. Kopans, D. Castleberry, B. Opsahl-Ong, C. Landberg, P. Slanetz, A. Giardino, and R. o. Moore. Digital tomosynthesis in breast imaging. *Radiology*, 205(2): 399–406, 1997. 23

[104] M. Nikolova. Local strong homogeneity of a regularized estimator. *SIAM Journal on Applied Mathematics*, 61(2):633–658, 2000. 38, 59, 60

[105] A. C. of Radiology et al. Acr bi-rads atlas: breast imaging reporting and data system. *Reston, VA: American College of Radiology*, 2014: 37–78, 2013. 13, 15, 113

[106] J. M. Ortega and W. C. Rheinboldt. *Iterative solution of nonlinear equations in several variables*. SIAM, 2000. 79

[107] J. Park, E. Franken Jr, M. Garg, L. Fajardo, and L. Niklason. Breast tomosynthesis: present considerations and future applications. *Radiographics*, 27(suppl_1):S231–S240, 2007. 18

[108] S. Park, H. Barrett, E. Clarkson, M. Kupinski, and K. Myers. Channelized-ideal observer using Laguerre-Gauss channels in detection tasks involving non-Gaussian distributed lumpy backgrounds and a Gaussian signal. *Journal of the Optical Society of America A*, 24(12): B136–B150, December 2007. doi: 10.1364/JOSAA.24.00B136. URL http://josaa.osa.org/abstract.cfm?URI=josaa-24-12-B136. 35, 43

[109] S. Park, J. M. Witten, and K. Myers. Singular vectors of a linear imaging system as efficient channels for the bayesian ideal observer. *IEEE Transactions on Medical Imaging*, 28.5:657–668, 2009. doi: 10.1109/TMI.2008.2008967. 31

[110] D. Perrone and P. Favaro. A logarithmic image prior for blind deconvolution. *International journal of computer vision*, 117(2):159–172, 2016. 61

[111] E. L. Piccolomini and E. L. Morotti. A fast Total Variation-based iterative algorithm for digital breast tomosynthesis image reconstruction. *Journal of Algorithms & Computational Technology*, 10(4):277–289, 2016. doi: doi:10.1177/1748301816668022. 28

[112] L. Platiša, B. Goossens, E. Vansteenkiste, S. Park, B. Gallas, A. Badano, and W. Philips. Channelized Hotelling observers for the assessment of volumetric imaging data sets. *Journal of the Optical Society of America A*, 28:1145–1163, 2011. doi: 10.1364/JOSAA.28.001145. URL http://josaa.osa.org/abstract.cfm?URI=josaa-28-6-1145. 31, 35, 43, 110

[113] S. Poplack, T. Tosteson, C. Kogel, and H. Nagy. Digital breast tomosynthesis: initial experience in 98 women with abnormal digital screening mammography. *American Journal of Roentgenology*, 189 (3):616–623, 2007. 21

[114] A. Repetti, M. Q. Pham, L. Duval, E. Chouzenoux, and J.-C. Pesquet. Euclid in a taxicab: Sparse blind deconvolution with smoothed $\ell_1 - \ell_2$ regularization. *IEEE Signal Processing Letters*, 22(5):539–543, 2014. 61

[115] L. Rosasco and S. Villa. Learning with incremental iterative regularization. In *Advances in Neural Information Processing Systems*, pages 1630–1638, 2015. 111

[116] L. I. Rudin, S. Osher, and E. Fatemi. Nonlinear total variation based noise removal algorithms. *Physica D: nonlinear phenomena*, 60(1-4): 259–268, 1992. 60

[117] M. Sachs, J. Nachmias, and J. Robson. Spatial-frequency channels in human vision. *JOSA*, 61(9):1176–1186, 1971. 110

[118] I. Sechopoulos. A review of breast tomosynthesis. Part I . The image acquisition process. *Medical Physics*, 40:1–12, 2013. 20

[119] I. Sechopoulos. A review of breast tomosynthesis. Part II. Image reconstruction, processing and analysis, and advanced applications. *Medical Physics*, 40:014302, 2013. 20, 23, 24

[120] I. Sechopoulos. A review of breast tomosynthesis. Part I. The image acquisition process. *Medical Physics*, 40(1):014301, 2013. 17

[121] M. Shetty. Screening and diagnosis of breast cancer in low-resource countries: what is state of the art? In *Seminars in Ultrasound, CT and MRI*, volume 32, pages 300–305. Elsevier, 2011. 10

[122] E. Sidky, I. Reiser, R. Nishikawa, and X. Pan. Image reconstruction in digital breast tomosynthesis by total variation minimization. In *Proceedings SPIE Medical Imaging*, volume 6510, San Diego, CA, March 2007. 28, 59

[123] E. Sidky, I. Reiser, R. Nishikawa, X. Pan, R. Chartrand, D. Kopans, and R. Moore. Practical iterative image reconstruction in digital breast tomosynthesis by non-convex tpv optimization. In *Medical Imaging 2008: Physics of Medical Imaging*, volume 6913, page 691328. International Society for Optics and Photonics, 2008. 28

[124] E. Sidky, X. Pan, I. Reiser, R. Nishikawa, R. Moore, and D. Kopans. Enhanced imaging of microcalcifications in digital breast tomosynthesis through improved image-reconstruction algorithms. *Medical Physics*, 36(11):4920–4932, 2009. ISSN 0094-2405. doi: 10.1118/1.3232211. URL http://www.pubmedcentral.nih.gov/articlerender.fcgi?artid=2773453{&}tool=pmcentrez{&}rendertype=abstract. 28, 59

[125] R. Siegel, K. Miller, and A. Jemal. Cancer statistics, 2016. *CA: a cancer journal for clinicians*, 66(1):7–30, 2016. 8

[126] P. Skaane, A. Bandos, E. Eben, I. Jebsen, M. Krager, U. Haakenaasen, U. Ekseth, M. Izadi, S. Hofvind, and R. Gullien. Two-view digital breast tomosynthesis screening with synthetically reconstructed projection images: comparison with digital breast tomosynthesis with full-field digital mammographic images. *Radiology*, 271(3):655–663, 2014. 22

[127] S. Smith et al. The scientist and engineer's guide to digital signal processing. 1997. 24, 113

[128] R. Sood, A. Rositch, D. Shakoor, E. Ambinder, K. Pool, E. Pollack, D. Mollura, L. Mullen, and S. Harvey. Ultrasound for breast cancer detection globally: A systematic review and meta-analysis. *Journal of global oncology*, 5:1–17, 2019. 10

[129] M. Spangler, M. Zuley, J. Sumkin, G. Abrams, M. Ganott, C. Hakim, R. Perrin, D. Chough, R. Shah, and D. Gur. Detection and classification of calcifications on digital breast tomosynthesis and 2d digital mammography: a comparison. *American Journal of Roentgenology*, 196(2):320–324, 2011. 21

[130] J. Sun, H. Li, Z. Xu, et al. Deep admm-net for compressive sensing mri. In *Advances in neural information processing systems*, pages 10–18, 2016. 111

[131] Y. Sun, P. Babu, and D. P. Palomar. Majorization-minimization algorithms in signal processing, communications, and machine learning. 65(3):794–816, Feb. 2017. 64

[132] T. Szasz, A. Basarab, and D. Kouamé. Beamforming through regularized inverse problems in ultrasound medical imaging. *IEEE transactions on ultrasonics, ferroelectrics, and frequency control*, 63(12): 2031–2044, 2016. 28

[133] A. Tagliafico, B. Bignotti, F. Rossi, A. Signori, M. Sormani, F. Valdora, M. Calabrese, and N. Houssami. Diagnostic performance of contrast-enhanced spectral mammography: systematic review and meta-analysis. *The Breast*, 28:13–19, 2016. 11

[134] D. Van de Sompel and M. Brady. Regularising limited view tomography using anatomical reference images and information theoretic similarity metrics. *Medical image analysis*, 16(1):278–300, 2012. 28

[135] R. Van Metter, J. Beutel, and H. L. Kundel. *Handbook of Medical Imaging*, volume 1. Laurel, MD, 2000. 31, 35

[136] F. Wheeler, A. Perera, B. Claus, S. Muller, G. Peters, and J. Kaufhold. Micro-calcification detection in digital tomosynthesis mammography. In *Proc. SPIE Medical Imaging*, volume 6144, San Diego, CA, March 2006. doi: doi:10.1117/12.653478. URL https://doi.org/10.1117/12.653478. 38, 40

[137] N. Wongpakaran, T. Wongpakaran, D. Wedding, and K. L. Gwet. A comparison of cohen's kappa and gwet's ac1 when calculating inter-rater reliability coefficients: a study conducted with personality disorder samples. *BMC medical research methodology*, 13(1):61, 2013. 103, 104

[138] T. Wu, R. Moore, and D. Kopans. Voting strategy for artifact reduction in digital breast tomosynthesis. *Medical physics*, 33(7Part1): 2461–2471, 2006. 20

[139] H. Xin and S. Park. Model observers in medical imaging research. *Theranostics*, 3(10):774, 2013. 37

[140] G. Xu, Y. Xia, and H. Ji. Weighted total variation based convex clustering. *arXiv preprint arXiv:1808.09144*, 2018. 59

[141] Y. Xu, T. Géraud, and L. Najman. Connected filtering on tree-based shape-spaces. *IEEE transactions on pattern analysis and machine intelligence*, 38(6):1126–1140, 2015. 110

[142] M. Yalaza, A. İnan, and M. Bozer. Male breast cancer. *The journal of breast health*, 12(1):1–8, January 2016. 8

[143] C. Yip, R. Smith, B. Anderson, A. Miller, D. Thomas, E. Ang, R. Caffarella, M. Corbex, G. Kreps, A. McTiernan, et al. Guideline implementation for breast healthcare in low-and middle-income countries: Early detection resource allocation. *Cancer*, 113(S8):2244–2256, 2008. 10

[144] J. Youk, E.-K. Kim, K. Ko, and M. Kim. Asymmetric mammographic findings based on the fourth edition of bi-rads: types, evaluation, and management. *Radiographics*, 29(1):e33–e33, 2009. 12

[145] Y. Zhang, B. Pham, and M. Eckstein. The effect of nonlinear human visual system components on performance of a channelized hotelling observer in structured backgrounds. *IEEE Transactions on Medical Imaging*, 25(10):1348–1362, 2006. 110

[146] M. Zibulevsky and M. Elad. $\ell_1 - \ell_2$ optimization in signal and image processing. *IEEE Signal Processing Magazine*, 27(3):76–88, 2010. 79, 80